The University Of Sheffield.

Improving Workholding Layouts In Double Sided Machining

Camilo Soto

A thesis submitted in partial fulfilment of the requirements for the degree of

Doctor of Engineering

The University of Sheffield

Faculty of Engineering

Department of Mechanical Engineering

Submission Date

August 27, 2024

Acknowledgements

I would firstly like to express my sincere gratitude to my dedicated supervisor team, whose guidance and immense patience have been invaluable throughout this journey. A big thank you to Neil Sims, Erdem Ozturk, and Ben Weekes.

Secondly, I am truly grateful to all the people at GKN that gave me the opportunity to work alongside you and welcomed me with open arms. A special thanks to Ben for his useful insights, knowledgeable advice and constant disposition to help. Thanks to Dan Graham for organising the project and ensuring I had everything I needed.

I would like to express my gratitude to the Engineering and Physical Sciences Research Council (EPSRC) for their financial support, provided through grant number EP/L016257/1.

I would also like to thank the support and generosity the IDC has given me, particularly during my paternity leave for my second child. I truly appreciate the effort and feel blessed for your help. A big thank you to Pete, Clare and Chez.

Ty and Chris have also been essential for the completion of this work. I'm truly grateful for their trust and support.

Finalmente, el más profundo agradecimiento para mi familia, a mis viejos Camila y Raimundo, a mis hermanos Lucas y Vicente, y también a Sandra, Rodrigo y Bia. Gracias a todos por la motivación y el apoyo. Gracias León y gracias Julián por generarme ese amor infinito que me desborda el corazón y me llena de alegría. Más que a nadie, quiero agradecerle profundamente a Natalia. Gracias Nata por tu entrega inquebrantable y sobrehumana que nos das a todo momento. No sabes cuánto agradezco tu paciencia, comprensión y amor. Aprecio profundamente tus sacrificios y tu compromiso con nuestros proyectos de vida. Sin lugar a duda este logro es compartido, al igual que el resto de nuestras vidas. Juntitos, punta cerro.

Abstract

This thesis focuses on advancing the understanding of the dynamic behaviour for double-sided components by addressing the effects of workholding configurations. The research targets key questions regarding workpiece dynamics in order to enable this type of machining approach.

The study begins by reviewing the relevant state-of-the-art literature on machining induced vibrations, concentrating on chatter prediction models, as well as chatter avoidance in flexible parts. Complemented by the evaluation of research targeting machining fixture layout optimisation, a potential gap in knowledge is highlighted and aimed as a research avenue for this project.

The theoretical background is then summarised, describing the mathematical basis of modal analysis, finite element modelling, experimental modal analysis, and model updating methods. This foundation serves to underpin the framework and procedures for the subsequent chapters.

Optimisation programming and software integration follows, explaining the steps involved in creating an automated link between numerical software platforms for Finite Element Analysis (FEA) and a Particle Swarm Optimisation approaches. This integration creates a robust platform for evaluating and enhancing double-sided access and minimally held fixturing layouts.

The thesis then explores how validation and updating procedures enhance the predictive behaviour of FEA models, and the preferred experimental approaches required for model validation. This is achieved by several modal testing activities of components and structures, which provide the physical data to validate the models.

With a connection established between machining stability and computer-aided fixture design optimisation routines, an FEA-based methodology is employed to derive optimal solutions for external workholding layouts. The optimisation method is then

expanded onto the finishing stages of a component, specifically targeting parting-off tab layouts. This extension aims to improve the definition of breakaway tab arrangements through the investigation of suitable modelling approaches and optimisation routines.

The significance of this study lies in its potential industrial impact, enabling novel machining approaches for double-sided components in minimally held environments. The developed optimisation routines have the capability to target design areas traditionally managed manually based on experience. Additionally, enhanced FEA modelling techniques contribute to the refinement and precision of workholding evaluations.

In conclusion, this thesis offers a comprehensive framework for the definition and optimisation of workholding layouts in double-sided machining. By addressing critical questions in machining dynamics, it advances the industrial application of these techniques, contributing to the ongoing evolution of machining methodologies.

Contents

List of Figures

Nomenclature

Acronyms and Abbreviations

BC	Boundary Condition
CAD	Computer Assisted Design
DDE,ODE	Delay Differential Equation, Ordinary Differential Equation
DFT	Discrete Fourier Transform
DOF, mDOF	Degree of Freedom, multiple Degree of Freedom
DSA	Double Sided Access
EMA	Experimental Modal Analysis
FEA	Finite Element Analysis
FRF	Frequency Response Function
MAC	Modal Assurance Criterion
MBA	Multi-Body Assembly
MKE	Modal Kinetic Energy
MPA	Modal Participation Analysis
MRR	Material Removal Rate
OSM	Opposite Spindle Milling
PSO	Particle swarm optimisation
RPM	Revolutions per Minute
SDM	Semi-Discretisation Method
SLD	Stability Lobe Diagram

ZOA	Zeroeth Order Approximation

Coding

**.cmd*	Command file extension
**.inp*	Input file extension
**.stp*	STEP file extension
**.uff, *.unv*	Universal file format extensions
**.vtu*	VTU file extension

Greek alphabet

α, β	Proportional viscous damping coefficients
$\dot{\Gamma}_i$	Layout speed vector for particle i
γ^2	Coherence
Γ_i	Layout vector for particle i
Γ_T	Total number of possible workholding layouts
ν	Material Poisson ratio
Ω	Spindle speed
ω	Frequency
ω_c	Chatter Frequency
ω_i	Natural frequency of ith mode
Φ_i	Mass-normalised mode shape vector
ϕ_j	Tooth engagement angle
ρ	Material density
τ	Delay
ε	Relative wave phase angle
ζ_i	Dimensionless viscous damping coefficient

Latin alphabet

$\bar{L_j}$	Indexable length of component

$\mathbf{u_i}$	Eigenvector ith mode
$\mathbf{U}$	Global joint displacement
a_e	Radial depth of cut, Stepover
a_p	Axial depth of cut, Stepdown
a_{lim}	Limiting stable axial depth of cut
$a_{p,crit}$	Critical depth of cut
a_{xx}	Time varying dynamic force coefficient
d	Structural damping coefficient
E	Elastic modulus
f_t	Feed per tooth
G	Displacement-Force Receptance
g_{best}	Best global fitness function value for entire swarm
H	Frequency response function (FRF)
h_j	Chip thickness for tooth j
K_t	Cutting force coefficients
k_{ii}	Generalised stiffness ith mode
m_{ii}	Generalised mass ith mode
N_t	Number of Teeth
P_g	Best global position vector for entire swarm
P_i	Best position vector for particle i
P_{best}	Fitness value for P_i
$R_{rs,i}$	Modal residue
S_{xF}	Cross power spectrum
T	Kinetic energy
t	Time
V	Potential energy

$y(t)$	Modal state vector
$F(t), f$	Harmonic forcing
$x(t)$	State Vector

Mathematical operations

$\dot{(\cdot)}, \ddot{(\cdot)}$	Time differentiation
$\lfloor \cdot \rfloor$	Floor function
$\|\cdot\|$	Euclidean Norm
$\mathbf{G}(j\omega)$	Fourier Transform
$\mathcal{L}(s)$	Laplace Transform
j	$\sqrt{-1}$
$\mathrm{tr}(\cdot)$, $\mathrm{trace}(\cdot)$	Trace of a square matrix

Matrices

$[C]$	Damping matrix
$[I]$	Identity matrix
$[K], [\mathbf{K}]$	Stiffness matrix
$[M], [\mathbf{M}]$	Mass matrix
$[R]$	Updating response matrix
$[S]$	Updating sensitivity matrix
$[W]$	Updating weighting matrix
A	Directional force factor matrix
P	Mode shape matrix

Chapter 1

Introduction

Designing machining fixtures is a critical task for aerospace manufacturing companies, particularly when dealing with large scale double-sided components. These fixtures need to ensure reliable and repeatable alignment whilst providing sufficient clamping force which commonly results in stage specific bases and bespoke solutions. The downsides of using these methods include significant development times and costs, as well as limited versatility to handle varied geometries within a family of parts. Modern tendencies in large thin-walled components are looking at single setup environments which can allow unrestricted access to the workpiece on both sides [1], referred to as double sided access (DSA), as shown in Figure 1.1.

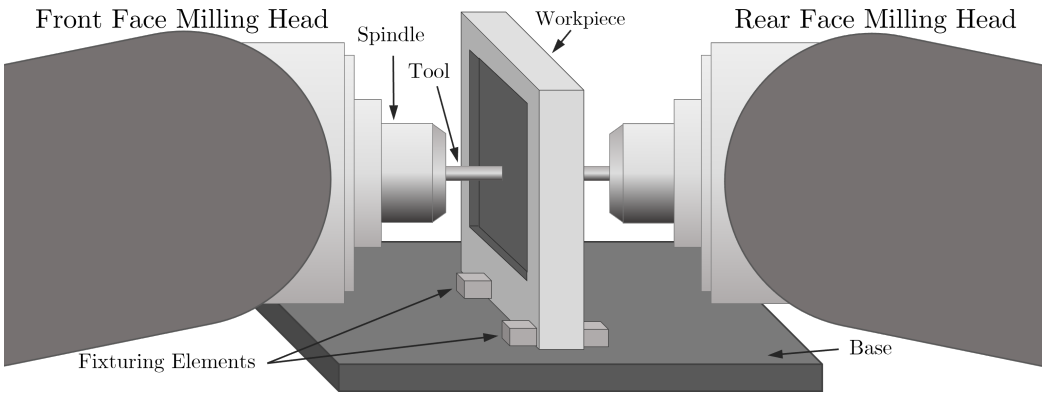

Figure 1.1: Schematic drawing of a DSA setup.

The main challenge arising from this ambitious type of setup is an increase in machining induced vibrations issues due to the inherent reduction in workpiece stiffness. In particular self-excited vibrations, due to the dynamic response characteristics of the cutting tool and workpiece, and referred to as regenerative chatter, can occur.

It is well established within the manufacturing field that excessive machining chatter hinders both the productivity and quality of machined components. To improve the process, often the focus is set on the cutting tool side of the machining operation, with comparatively less consideration given to the dynamic response of the workpiece. In such cases, unexpected stability issues can still arise from flexible structures with thin walls, floors or unsupported features. This issue is even more significant in modern manufacturing approaches that wish to remove traditional workholding solutions and provide modularity and re-configurable characteristics to the machining cycle of a component. Making use of the fact that workpiece dynamic response is highly dependent on the workholding configuration and associated boundary conditions, a series of benefits (quality, speed, etc.) can be obtained from expanding the knowledge and understanding of fixture layouts.

Targeting improvements to the academic and industrial developments on the dynamics of flexible workpieces, with an emphasis in the definition of workholding and fixturing layouts, presents an area for novelty in the field alongside an enhancement of the modelling capabilities of the sponsoring company (GKN Aerospace). In this project, the objectives revolve around the development of numerical methods to estimate, measure and improve the effects that workholding configurations can have on the dynamic properties of a component during machining. Understanding the applicability, accuracy and reliability of finite element models enables the construction of optimisation programs to target dynamic response based metrics and aid the definition of improved machining practices. A commonly manual process, such as the design of fixture and workholding layouts, can be automated and improved upon by using past research and the novel developments this projects aims to deliver.

The project serves as a bridge between the fields of machining dynamics and fixture layout optimisation, which have seen few studies linking them together [2]. The ultimate aim is to develop an integrated system of computer-aided fixture design using Finite Element Analysis (FEA) dynamic analysis to derive optimal workholding configurations which maximise cutting stability.

Closely linked to the external workholding designs, the application of optimisation programs can also target internal support features within a billet. In particular, the use of parting-off tabs and ties are a common practice within manufacturing (Fig. 1.2a). These critical operations are implemented at the very end of a component's manufacturing cycle and allow the finished component to be extracted from the remaining unmachined billet. Any non-conformance rising from machining induced

vibrations at this stage has limited remedial options for rectification. By understanding the dynamic response of the workpiece in its finishing stages, careful evaluation of the optimal locations for these tabs can provide the required balance between workholding strength, dynamic stability and manual removal benefits.

1.1 Industrial Drivers

Non-conformance due to unexpected chatter vibrations is a common limitation in high production rate industrial settings. GKN Aerospace has highlighted monolithic aluminium rib type components and other prismatic parts, such as A-frames or wings spars (Fig. 1.2) as particularly problematic. Machining of chatter poses serious consequences if left unaddressed, including premature tool failures, manual rework of affected areas, non-conformance and scrappage.

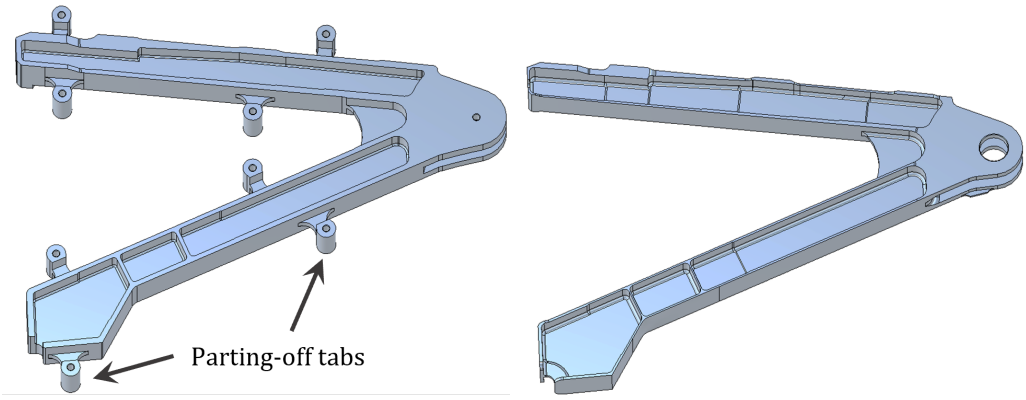

(a) Tab-held prismatic component (b) Finished prismatic component

Figure 1.2: Generic double sided prismatic component

Furthermore, the presence of chatter also prompts manufacturing organisations to redefine the global machining parameters of a part based on these problem areas, which lowers the overall productivity and Material Removal Rate (MRR). Alongside this loss of productivity, the process by which these cutting parameters are selected are commonly based on the NC programmer's experience of past similar components and trial and error approaches. Under further investigation of this issue, it is revealed that GKN Aerospace currently have no means to model the dynamic response of their workpieces, and therefore, limited predictive capabilities for machining stability of flexible components. Although some dynamic testing is performed to determine the frequency response function (FRF) of the tool, this information is mainly used as

a threshold value to check whether the machining centre is fit for purpose and limited stability analysis is currently being generated.

It is of interest to target and characterise the workpiece dynamics as a central industrial driver, particularly to enhance the understanding of fixturing and workholding solutions. At the moment GKN primarily use vacuum fixtures in most machining stages of their rib components. These types of fixtures are expensive to build and store, unique to a specific part, and despite regular inspections, still present some levels of variability in workholding performance. This variability occurs, among other reasons, because of material distortion (residual stress relaxation), geometrical constraints of the component, and deterioration of the fixture leading to seal failure for example. There is a need to increase the reliability of the workholding solution and, if possible, reduce the expenses associated by developing smaller scaled fixtures with easier to replace and maintain components.

On a longer term scale, there is also a drive to implement double-sided access to the workpiece and change the way ribs have traditionally been manufactured. By exposing both sides of a workpiece whilst machining, it enables a valuable range of applications such as, back face metrology and enhanced monitoring of the cutting process, and also opportunities for parallel, mirror and robotic assisted machining with multiple spindles and active chatter mitigation strategies. The modular aspect of DSA machining environments is also an attractive area of research for future manufacturing technologies. Using simpler workholding solutions can significantly reduce part production lead times and, consequently, increase the scalability, adaptability, and overall productivity.

In summary, the industrial drive is set upon investigating the effects different workholding solutions have on the dynamic response of the machining environment and improve modelling techniques to evaluate workpiece dynamic response in reduced fixturing scenarios. This can be applied at different stages of a machining cycle: At early roughing stages targeting external clamping layouts in DSA environments, and in finishing stages looking at optimal breakaway tab configurations.

1.2 Aim and Objectives

With a clear set of academic and industrial motivations to enhance workpiece modelling capabilities, the aim of this project is to develop a methodology to improve workholding configurations for DSA and minimally held machining environments. In

order to target this aim, more fundamental research questions are defined to establish focused research areas for the project. The main objectives and their associated research questions can be stated as:

O1. Develop a computational framework in which different DSA workholding layouts can be evaluated, and answer the following research questions:

- Q1: How can different numerical software platforms be integrated in order to develop a novel optimisation architecture?
- Q2: What optimisation approach is suitable for this type of analysis? What physical parameters in the system can be targeted as evaluation metrics?
- Q3: Given a set of part design and manufacturing parameters, what is the optimal workholding configuration under these restrictions?

O2. Introduce FEA dynamic analysis with model updating and multi-body assembly methods (MBA) to the optimisation protocol and compare layouts.

- Q4: How can model updating enhance FEA predictive behaviour and is it required for workholding optimisation?
- Q5: What EMA methods are preferred and how can they complement the FEA modelling activities?

O3. Develop a connection between chatter analysis and computer-aided fixture design and use the FEA methodologies to derive assembled solutions.

O4. Expand the optimisation methods onto finishing stages, targeting picture frame parting off tabs and answer:

- Q6: How can the optimisation programs improve parting tab definition?
- Q7: What type of modelling approach is best suited to evaluate this type of feature?

1.3 Outline of chapters

The chapters of this thesis are presented following the chronological development of the project and therefore begin with simpler tasks and applications, continuously increasing the complexity of the modelling and programming activities in different applications.

Chapter 2: Literature Review

This chapter provides a comprehensive examination of existing academic literature that relate to this project, focusing on the fields of machining induced vibrations and optimisation of machining fixture layouts. It serves to establish the theoretical and mathematical approaches employed across various models to predict chatter in milling processes. It also covers research that targets machining fixture optimisation, particularly for workholding layouts, aiming to uncover potential gaps in knowledge and avenues for academic novelty.

Chapter 3: Background

The background chapter defines the theoretical basis for the main analytical, numerical and experimental and procedures applied thereafter. Having a clear understanding in the mathematical derivation and provenance of the characteristic equations that describe the behaviour of vibrating systems is critical for adequate implementation of evaluation metrics in optimisation protocols. The topics covered are modal analysis, FEA modelling, EMA techniques and model updating for dynamic systems.

Chapter 4: Optimisation Programming

A novel and unique optimisation architecture is presented in this Chapter. It defines the implementation procedures of numerical, experimental and programming solutions utilised within. By means of a central software integration routine, different numerical computation environments are utilised in parallel to create feedback loops within the optimisation protocol.

Chapter 5: Model Updating of a Single Pocket Component

The single pocket coupon chapter is the first application of the tools described in the methodology. It serves as a scoping and learning exercise to evaluate the applicability of different FEA modelling techniques for a small scale aluminium component, with particular interest in boundary condition characterisation. It is complemented by detailed experimental modal analysis techniques (EMA) defining the required procedures for model updating and validation. It demonstrates the importance of pretest analysis, EMA procedures, FEA modal correlation metrics for improving the accuracy of different model updating alternatives.

Chapter 6: External Workholding Optimisation for Double-Sided Billets

This chapter tackles the optimisation of external workholding configurations on DSA machining environments of aluminium billets. Initially targeting an isolated billet, the optimisation program is run on numerous tests, expanding the versatility of user defined variables it can process. A series of evaluations on the behaviour of the optimisation routines allows fine tuning the parameters for better convergence of optimal results. The second section of this chapter expands the prior application by implementing the physical nature of the system and introducing a fixture frame onto the analysis. This aspect presents a series of additional modelling challenges, and allows the comparison of multi-body assembly techniques increasing the capabilities of the program.

Chapter 7: Optimisation of Parting-off Tab Layouts

Using the optimisation architecture developed thus far, Chapter 6 targets the definition of breakaway tabs and parting-off routines. In this case, a test coupon is designed to represent the typical features of a flexible double-sided component, with thin walls, floors and unsupported pockets. Careful evaluation of modelling techniques for this stage are studied and model updating routines are employed to enhance the FEA predictions. Machining trials provide EMA data for a non-optimised version of the component, as well as being able to quantify the benefits presented by an optimised component.

Chapter 8: Conclusions

The main points of discussion arising from each stage of this project are summarized in this conclusions chapter. It allows for detailed analysis of possible areas of improvement and future work proposals that can be derived from this work.

Chapter 2

Literature review

This chapter provides an in-depth review of the relevant literature in the field of machining induced vibrations, chatter prediction methods and mitigation strategies, as well as an overview of machining fixture layout optimisation and double sided access machining environments.

The first section details the defining the mathematical and physical theory commonly used to evaluate machining induced vibrations. By reviewing different approaches employed to describe and predict the chatter phenomena from a technical perspective, it provides the key parameters that shape and influence the behaviour of the system.

The following section presents a brief analysis of chatter mitigation strategies. Understanding the constant development and wide range of applications within the field, the focus is mainly set on chatter avoidance topics. Nevertheless some associated and relevant suppression, mitigation and control approaches are also explored.

Machining fixture layout optimisation is a field that commonly sits slightly apart from the previous two, in the sense that computer assisted fixture design typically priorities alternative aspects specific to machining and assembly rather than solely focusing on dynamic features (such as clamping workpiece deflections, or part location strategies). Nevertheless, the field has still seen some bridging research, and the aim of this review is to highlight potential gaps in knowledge and gauge the appropriate methods to link both fields.

The final section explores the area of double sided machining and reduced fixturing approaches.

2.1 Machining induced vibrations and chatter

The first step to describe chatter in machining is to define the types of vibrations present in metal cutting procedures depending on the characteristics of the external source of energy imparted into the system, i.e. forcing input [3]. In this sense, three main classifications of vibration are identified; free, forced and self-excited vibrations. The principles behind these types of vibration can be easily accessed in textbooks on the subject [4], but a machining perspective of these is detailed below.

1. **Free Vibrations:** Correspond to the case in which an external energy source is imparted onto the dynamic system to initiate vibrations and then removed. The resulting vibration of the system as it tries to recover its equilibrium position is considered to be *free*, aside from the initial perturbation (either position or velocity). In a machining environment, this type of vibration can be observed in highly intermittent milling operations while the tooth is out of cut, or when an incorrect tool path results in a collision [5, 3, 6].

   Mathematically, this type of vibration is usually represented by a linear, viscously damped, second order differential equation of the form:

   $$[M]\{\ddot{x}(t)\} + [C]\{\dot{x}(t)\} + [K]\{x(t)\} = 0 \tag{2.1}$$

   The length of the vector $\{x(t)\}$ corresponds to the n degrees of freedom of the system and matrices $[M], [C]$ and $[K]$ are square of dimension $n \times n$. In order to derive modal analytic solutions of this system (especially for real mode determination) it is required to have proportional damping (a linear combination of mass and stiffness matrices) of the form $[C] = \alpha[M] + \beta[K]$. This allows to treat the system as a eigenvalue problem and identify the system's mode shapes [4]. Further details are presented in Section 3.1.

2. **Forced Vibrations:** This type of vibration is caused by the effect of an external force on the system. The response of the system will depend on the nature of this external force $\{F(t)\}$, which can include harmonic, periodic, step, impulse and arbitrary force. This will extend Eq. (2.1), by the addition of the forcing term, to:

   $$[M]\{\ddot{x}(t)\} + [C]\{\dot{x}(t)\} + [K]\{x(t)\} = \{F(t)\} \tag{2.2}$$

   In milling, forced vibrations are clearly present whilst the tool is engaged in the material and generating a chip. They can also be present due to unbalanced

tools and bearings, and can even be transmitted through the foundations of a machine.

It is understood that with proper identification of the sources of free and forced vibrations, reduction and avoidance can be obtained for both external sources and internal sources of energy [3, 5].

3. **Self-excited Vibrations:** This type of vibration is generally known in the manufacturing environment as chatter and is caused by the interaction between tool and workpiece during cut. It can be further categorized into primary chatter and secondary chatter depending on the nature of the regenerative mechanism [7].

   Primary chatter is caused due to the alternating cutting forces of the cutting process in itself either by velocity dependant friction between tool and workpiece (Arnold type) [8], or thermo-mechanical effects occurring in the plastic deformation zone of chip formation area [9].
   A last source of primary chatter is mode coupling, which applies to systems with at least two degrees of freedom in different directions of the same plane of cut [10]. As per Gasparetto's [11] eigenvalue analysis, slight variation in stiffness for, in this case, perpendicular vibration modes result in elliptical spiral movements multiplied by an exponential. Depending on the sign of the exponential coefficient distinction is made between stable (decaying) and unstable (increasing) motion. His approach used a simple 2DOF undamped system under the assumption that damping would only increase the stability of the system [12].
   Mode coupling has been targeted extensively in robotic milling research due to the significant lower values of stiffness compared to conventional CNC machines [13, 14, 12]. When studying conventional milling machines, this type of chatter is usually considered less significant than the regenerative effect and cross FRFs of the machine tool are, in some cases, neglected [15]. Nevertheless, even if cross-coupled vibrations are considered, the stability models presented for the regeneration principle will inherently take them into account [10]. However, recent research targeting mode coupling chatter in robotic milling [16] concluded that mode coupling was not a limiting factor in milling stability, and associated the speed and depth of cut dependence on the regenerative chatter mechanism.

Secondary Chatter, also known as *Regenerative Chatter* is the most common form of self-excited vibrations in manufacturing environments [9]. Observing that each chip removes an amount of material, subsequent chip thickness is dependent, in part, on the previous chip. Based on this condition, regenerative chatter is caused by the relative phase difference between vibrations marks of these successive cuts. The vibration marks cause a fluctuation in chip thickness and, therefore, cutting forces of subsequent chips.

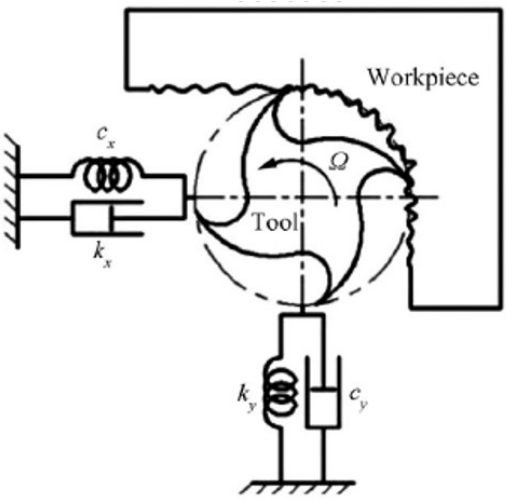

(a) 2DOF milling dynamic model [10]

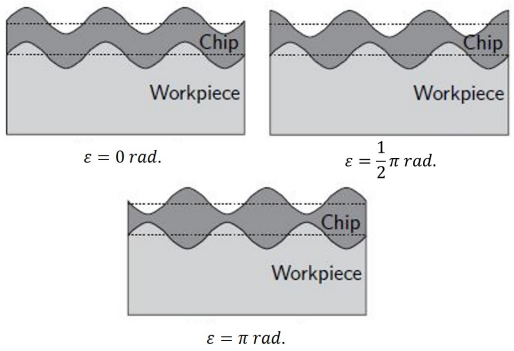

(b) Effect of relative phase (ε) of subsequent tooth passes on chip thickness [7]

Figure 2.1: Visual representation of regenerative chatter

A schematic visualisation of the common two DOF representation of a milling dynamic system and the effect the relative phase of vibration in successive tooth passes can be seen in Figure 2.1. Noting the effect of the relative phase in Figure 2.1b, if $\varepsilon = 0$ the system is considered *in-phase* and chip thickness is constant (equal to the static chip thickness), thus no variation in forces would be perceived. On the contrary, if $\varepsilon = \pi$ the system would then be *out-of-phase* and the maximum variation in chip thickness is observed. This fluctuation in chip thickness might further amplify the vibrations of tool and workpiece and build-up chatter, to the point were the tool might even escape the cutting zone and lose contact with the workpiece.

A widely accepted premise is that cutting force is linearly dependant on chip thickness (h) and the axial depth of cut (a_p) by constants called *cutting force coefficients* [17], and therefore the dynamic model of the system will not only depend on the current position of the tool, but the previous engagement as

well, redefining the external force of Equation 2.2 as a vector of functions $\{F(t, x(t), x(t-\tau)\}$. A more detailed review of this aspect and its implications, as well as the assumptions on system's degrees of freedom, are presented in the next sections.

2.1.1 Chatter Prediction Methods

The early works by Tlusty and Tobias paved the way for most of current prediction methods today. Tlusty derived from a one and two degree-of-freedom (DOF) model, a stability threshold relationship that linked depth of cut and spindle speed and which is known as a stability lobe diagram (SLD) [18]. A generic SLD graph is presented in 2.2 and shows the relationship between spindle speed and critical depth of cut, defining a boundary between stable and unstable machining conditions. Merrit built upon this phenomenon to present a first feedback model to describe the chatter loop and allow for a N-DOF linear system to be expressed based on the frequency response functions (FRF) [19].

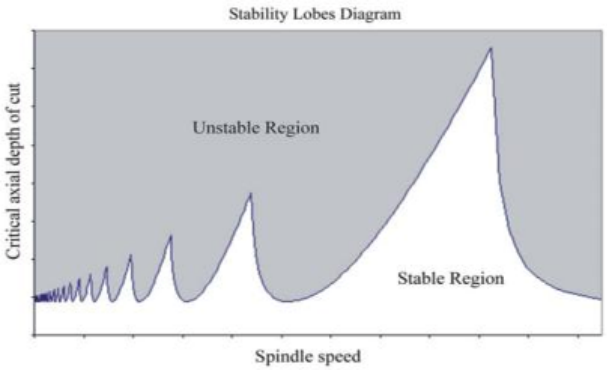

Figure 2.2: Generic SLD plot

Using Merrit's approach and Sridhar's development [20], the block diagram of Figure 2.3 is constructed in order to understand the chatter generation mechanism from a control theory perspective. This diagram was adapted from [19, 3, 7, 20] and was developed to include both tool assembly and workpiece dynamics.

The cycle of Figure 2.3 describes how the tooth path and static chip thickness of tooth j, $h_{j,stat}(t)$, will impart a force $F(t)$, on both the workpiece and the tool, which depends on cutting conditions. The displacement of the tool and the workpiece is determined by their FRF values, and when combined, define the relative displacement vector ($\overline{x}(t)$) that is evidenced as undulations on the workpiece. The primary

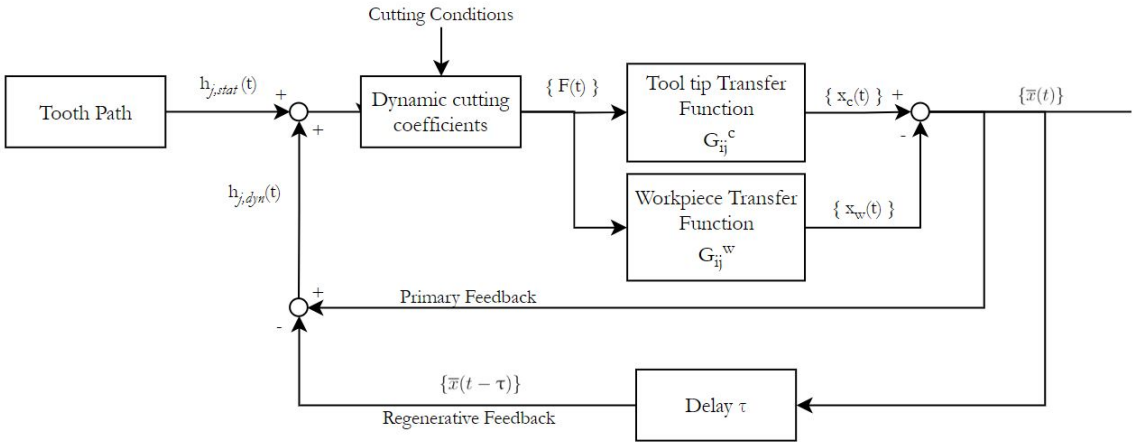

Figure 2.3: Block Diagram of a milling process with flexible tool and workpiece.

feedback loop is the inner modulation of the chip boundary, defined by the current state of vibrations, whilst the regenerative feedback is the outer modulation left by the previous tooth engagement and represented as a delay, τ. In other words, the previous tooth's inner modulation is the outer modulation for the current one.

In the early 1990s Minis [21] derived an analytical solution to the 2DOF system applying Floquet theory to solve delayed differential equations and Nyquist stability criterion considering cutting stiffness and damping values for a two dimensional mill model.

Closely after, Altintas and Budak published [17] one of the most iconic studies in the field. In this approximation a 2DOF flexible straight tooth tool was modelled and the force approximation of Equation 2.2 were presented as functions of the axial depth of cut (a_p), the directional cutting force coefficients constants (K_x) and the chip thickness h. For the tangential and radial directions of the tool the force can be modelled as follows:

$$F_{t,j} = a_p K_t h(\phi_j), \quad F_{r,j} = K_r F_{t,j} \tag{2.3}$$

For these expressions, chip thickness h depends on the angular position of tooth j, as seen in Figure 2.1a. In order to resolve these forces onto the x and y directions the following transform is applied:

$$\begin{aligned} F_{x,j} &= -F_{t,j}\cos\phi_j - F_{r,j}\sin\phi_j \\ F_{y,j} &= +F_{t,j}\sin\phi_j - F_{r,j}\cos\phi_j \end{aligned} \tag{2.4}$$

The chip thickness is modeled as the sum of a static and dynamic components. The static term is the nominal geometric path of the tooth, which in this case was assumed

circular as table feed is usually much lower than surface cutting speed, therefore $h_{j,stat} = f_z \sin\phi_j \cdot g(\phi_j)$, where $g(\phi_j)$ is a step function to define whether the tooth is in cut or not. The dynamic component, depends on previous and current modulation, defined by the relative displacement vector for both directions ($\{\Delta x(t)\}$). Therefore the dynamic chip thickness is approximated in this study, as:

$$h_{j,dyn} = g(\phi_j) \cdot [\sin\phi_j \quad \cos\phi_j] \underbrace{\left(\{\overline{x}(t)\} - \{\overline{x}(t-\tau)\}\right)}_{\{\Delta x(t)\}} \tag{2.5}$$

Combining equations 2.4 and 2.5 and using some trigonometric identities, the following two dimensional matrix system is defined:

$$\begin{Bmatrix} F_{x,j} \\ F_{y,j} \end{Bmatrix} = \frac{1}{2} a K_t \begin{bmatrix} a_{xx} & a_{xy} \\ a_{yx} & a_{yy} \end{bmatrix} \begin{Bmatrix} \Delta x \\ \Delta y \end{Bmatrix} \tag{2.6}$$

Where the *directional dynamic milling force coefficients* are given by:

$$\begin{aligned} a_{xx} &= -g_j[\sin 2\phi_j + K_r(1 - \cos 2\phi_j)] \\ a_{xy} &= -g_j[(1 + \cos 2\phi_j) + K_r \sin 2\phi_j] \\ a_{yx} &= \ \ g_j[(1 - \cos 2\phi_j) - K_r \sin 2\phi_j] \\ a_{xy} &= \ \ g_j[\sin 2\phi_j - K_r(1 - \cos 2\phi_j)] \end{aligned}$$

If more than one tooth is in cut at any given time, the model assumes that the total force in each direction is the summation of every tooth component, $F_x = \sum_j F_{x,j}$.

By knowing the angular velocity of the tool, then the system of equation 2.6 can be expressed in time domain as:

$$\{F(t)\} = \frac{1}{2} a K_t [A(t)] \{\Delta x(t, \tau)\} \tag{2.7}$$

Replacing this expression in the forced vibration equation (2.2) yields:

$$[M]\{\ddot{x}(t)\} + [C]\{\dot{x}(t)\} + [K]\{x(t, \tau)\} = \frac{1}{2} a K_t [A(t)] \{\Delta x(t, \tau)\} \tag{2.8}$$

Special care revolves around the directional time dependant factor matrix $[A(t)]$. Given that it is time dependant and periodic at the tooth pass frequency, the first approximations to solving this *Delayed Differential Equation* (DDE) used a Fourier Series expansion on the directional milling coefficients [17]. Another approach by Insperger and Stepan [22] proposed a semi-discretisation method to approximate the delayed terms as a piecewise constant function and solve the DDE as a series of ODEs. A small expansion of both methods is presented.

Fourier Series Approximation

The first option to solve equation 2.8 is using a Fourier series expansion on the time dependent directional milling coefficients. The number of harmonics of the tooth pass frequency to be considered in the Fourier expansion of $A(t)$ depends on the radial immersion of the tool and the number of teeth in cut. In early works [17] only the zeroth order component was calculated and hence the average was considered. This was very helpful for this semi-analytical solution as the directional factor would now be time invariant but immersion dependant (defined by start and exit angles of each tooth). This is where Altintas and Budak's method receives the generalised name of *Zeroth Order Approximation* (ZOA). In effect, the expression for the milling force vector of eq. 2.7 would now be:

$$F(t) = a_p K_t A_0 \{\Delta x(t, \tau)\} \tag{2.9}$$

Where A_0 is the average of the Fourier series expansion (Eqs. (2.10) and (2.11)) given by:

$$[A(t)] = \sum_{r=-\infty}^{\infty} [A_r] e^{jr\omega t} \tag{2.10}$$

$$[A_r] = \frac{1}{T} \int_0^T [A(t)] e^{-jr\omega t} \tag{2.11}$$

$$\implies A_0 = \frac{1}{T} \int_0^T [A(t)] = \frac{N}{2\pi} \begin{bmatrix} \alpha_{xx} & \alpha_{xy} \\ \alpha_{yx} & \alpha_{yy} \end{bmatrix} \tag{2.12}$$

Analysing this system in the Laplace domain, the displacement vector x caused by the force F can be expressed by means of the transfer function G (with more details provided in Chapter 3), as:

$$\begin{bmatrix} X(s) \\ Y(s) \end{bmatrix} = \begin{bmatrix} G_{xx}(s) & G_{xy}(s) \\ G_{yx}(s) & G_{yy}(s) \end{bmatrix} \cdot \begin{bmatrix} F_x(s) \\ F_y(s) \end{bmatrix} \tag{2.13}$$

By combining eqs. 2.9 and 2.13 a system of equations is obtained:

$$[\mathbf{I} + \Lambda(s) A_0 G(s)] F(s) = 0 \tag{2.14}$$

Where $\Lambda(s) = -a_p K_t (1 - e^{-s\tau})$ and $\mathbf{I}$ is the identity matrix. The non-trivial solutions are given when the determinant is equal to zero as:

$$\det[\mathbf{I} + \Lambda(s) A_0 G(s)] = 0 \tag{2.15}$$

If considering decoupled dynamics in x and y directions then the cross FRFs are neglected, $G_{xy} = G_{yx} = 0$. Expressing Eq. (2.15) in frequency domain, by $s = j\omega_c$ yields:

$$a_0\Lambda^2 + a_1\Lambda + 1 = 0 \tag{2.16}$$

with

$$\begin{aligned} a_0 &= G_{xx}G_{yy}(\alpha_{xx}\alpha_{yy} - \alpha_{xy}\alpha_{yx}) \\ a_1 &= \alpha_{xx}G_{xx} + \alpha_{yy}G_{yy} \end{aligned}$$

Finally the eigenvalue Λ is found by:

$$\Lambda = \frac{-a_1 \pm \sqrt{a_1^2 - 4a_0}}{2a_0} = \Lambda_R + j\Lambda_I \tag{2.17}$$

By analysing the real part of this solution and using $\kappa = \frac{\Lambda_I}{\Lambda_R} = \frac{\sin\omega_c T}{1-\cos\omega_c T}$ yields an expression for critical axial depth of cut given the chatter frequency ω_c:

$$a_{lim} = -\frac{2\pi\Lambda_R}{NK_t}(1+\kappa^2) \tag{2.18}$$

The spindle speed is calculated by using the trigonometric relation:

$$\tan\left(\frac{\alpha}{2}\right) = \frac{\sin\alpha}{1+\cos\alpha} \tag{2.19}$$

$$\implies \kappa = \tan\left(\frac{\pi}{2} - \frac{\omega_c\boldsymbol{\tau}}{2}\right) := \tan\psi \tag{2.20}$$

ψ is the phase of the eigenvalue ($\psi = \arctan\kappa$) and the phase shift between inner and outer modulation of a tool pass is $\varepsilon = \pi - 2\psi$ as seen in Figure 2.1b. The number of full vibration waves left on the arc by subsequent teeth is given by:

$$\varepsilon + 2k\pi = \omega_c\boldsymbol{\tau} \tag{2.21}$$

With k being the integer number of full vibrations between teeth, and the so-called *lobe number*. This yields the final expression for the spindle speed (N), using the delay as equal tooth pass period and the number of flutes (z):

$$N = \frac{60}{z\boldsymbol{\tau}} = \frac{60\omega_c}{z(\varepsilon + 2k\pi)} \tag{2.22}$$

Although this method has proven to be useful in cases where the forces don't vary considerably and the average is a good approximation, i.e. high radial immersion and large number of teeth, it has limited ability to accurately represent highly intermittent operations and low radial immersion cases [23]. In order to account for

these cases, multi-frequency methods were developed initially by Minis and Yanushevski [21] and later by Altintas and Budak [24]. Although these studies were able to consider harmonics of the tooth passing frequency, they did not focus on highly intermittent processes and the additional lobes that might be present due to perdiod doubling (or Flip) bifurcations [25]. This was covered by Merdol and Altintas [26] in a study of the multi-frequency method in interrupted and low radial immersion milling. Sims et al. evaluated three analytical methods to study stability in low immersion variable helix and variable pitch endmills [27]. Bachrathy and Stepan [28] further developed this multi-frequency approach to include distributed delays rising from variable pitch and variable helix angle tools.

This procedure has also been applied to describe milling operations with a different assumption on degrees of freedom of the system. Figure 2.4 shows different configurations that have been studied.

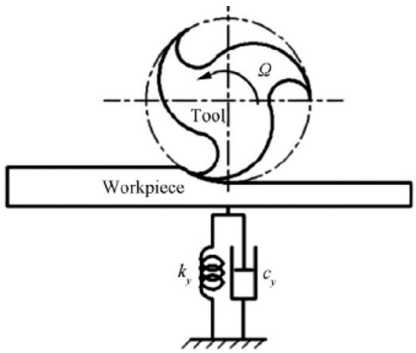

(a) Single degree of freedom [10]

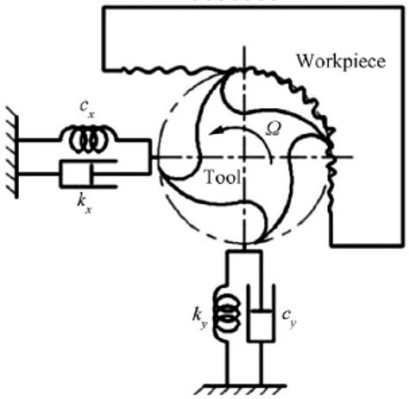

(b) Two degrees of freedom [17]

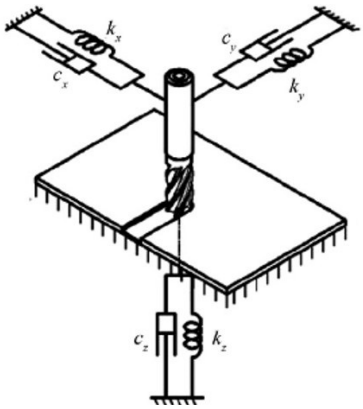

(c) Three degrees of freedom [29]

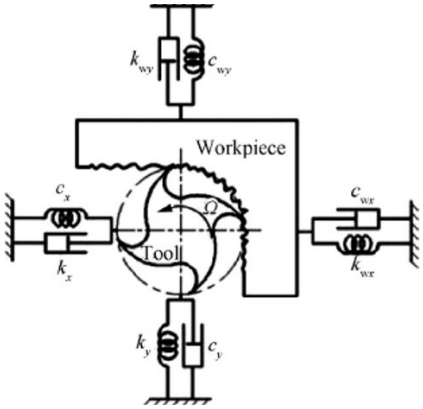

(d) Four degrees of freedom [24]

Figure 2.4: Different Chatter spring-damper models

Semi-discretisation

Another method to solve the DDEs of eq. 2.8 was presented by Insperger and Stepan [30, 31] and is called the semi-discretisation method (SDM). This approach approximates the time delayed term by a piecewise constant function and represents the DDE as a series of ODEs. Re-analyzing the 2DOF system, it can be re-written as:

$$[M]\{\ddot{x}(t)\} + [C]\{\dot{x}(t)\} + \big([K] + [Q(t)]\big)\{x(t)\} = [Q(t)]\{x(t-\tau)\} \tag{2.23}$$

Where $[Q(t)] = -a_p K_t [A(t)]$. What follows is to introduce a discretisation using a temporal interval $\Delta t = [t_i, t_{i+1})$, thus redefining the delay term as $\tau = (m + \frac{1}{2})\Delta t$, where m is an integer defining the coarseness of the discretisation. The effect of coarseness on the approximation of time-dependant delay can be observed graphically in Figure 2.5, obtained from [30].

The periodic coefficient $[Q(t)] = [Q(t-\tau)]$ and the delayed state $x(t-\tau)$ are approximated by:

$$\begin{aligned} &[Q(t)] \approx [Q(t_i)] = [Q_i] \\ &x(t-\tau) \approx \tfrac{1}{2}\Big(x(t_{i-m+1}) + x(t_{i-m})\Big) = \tfrac{1}{2}\Big(x_{i-m+1} + x_{i-m}\Big) \end{aligned} \tag{2.24}$$

Which in effect transforms eq. 2.24 into a series of second order ODEs:

$$[M]\{\ddot{x}(t)\} + [C]\{\dot{x}(t)\} + \big([K] + [Q_i]\big)\{x(t)\} = \frac{Q_i}{2}\Big(x_{i-m+1} + x_{i-m}\Big) \tag{2.25}$$

This approximation targets these equations by using Floquet method to solve differential equations with periodic coefficients. To do so, it is convenient to express eq. 2.24 as a first order ODE by using the variable $\mathbf{u} = [x,\ y,\ \dot{x},\ \dot{y}]$, $\mathbf{D} = (\mathbf{I} \quad \mathbf{0})$ ($\mathbf{I}$ is the 2x2 identity matrix), hence:

$$\begin{aligned} &\dot{\mathbf{u}}(t) = \mathbf{W}(t)\mathbf{u}(t) + \mathbf{V}(t)\mathbf{v}(t-\tau) = \mathbf{W}(t)\mathbf{u}(t) + \mathbf{w}(t) \\ &\mathbf{v}(t) = \mathbf{D}\mathbf{u}(t) \end{aligned} \tag{2.26}$$

where

$$\mathbf{W}(t) = \begin{pmatrix} \mathbf{0} & \mathbf{I} \\ -\Big(M^{-1}\big(K + A(t)\big)\Big) & -M^{-1}C \end{pmatrix} \quad , \quad \mathbf{V}(t) = \begin{bmatrix} 0 \\ M^{-1}A(t) \end{bmatrix} \tag{2.27}$$

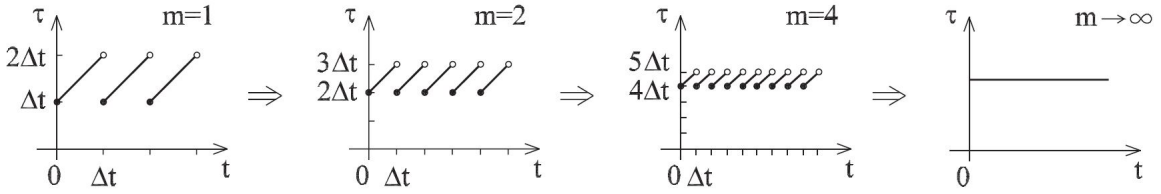

Figure 2.5: Time-dependant delay

For initial conditions $\mathbf{u}(t_i) = \mathbf{u}_i$ and assuming an invertible matrix $\mathbf{W}$ the solution to eq. 2.27 is given by:

$$\mathbf{u}(t) = \exp(\mathbf{W}_i \cdot \Delta t) \underbrace{(\mathbf{u}_i + \mathbf{W}_i^{-1}\mathbf{u}_i)}_{=K_i(\text{constant vector})} - \mathbf{W}_i^{-1}\mathbf{w}_i \tag{2.28}$$

where

$$\mathbf{W}_i = \frac{1}{\Delta t}\int_{t_i}^{t_{i+1}} \mathbf{W}(t)dt \tag{2.29}$$

Substituting $t = t_{i+1}$ into eq. 2.28 implies that:

$$\begin{aligned} \mathbf{u}_{i+1} &= \exp(\mathbf{W}_i\Delta t)\mathbf{u}_i + \Big(\exp(\mathbf{W}_i\Delta t) - \mathbf{I}\Big)\mathbf{W}_i^{-1}\mathbf{V}_i(\mathbf{u}_{i-m+1} + \mathbf{u}_{i-m}) \\ &= \mathbf{P}_i\mathbf{u}_i + \mathbf{R}_i(\mathbf{u}_{i-m+1} + \mathbf{u}_{i-m}) \end{aligned} \tag{2.30}$$

Therefore, eq. 2.24 relates the states of the system at time t_i and t_{i+1}, which can be represented as a discrete map:

$$\mathbf{y}_{i+1} = \mathbf{Z}_i\mathbf{y}_i \tag{2.31}$$

Where the state vector is $\mathbf{y}_i = [\mathbf{u}_i,\ \mathbf{u}_{i-1},\ \ldots,\ \mathbf{u}_{i-m}]$ and the coefficient matrix is of the form:

$$\mathbf{Z}_i = \begin{bmatrix} \mathbf{P}_i & 0 & 0 & \ldots & 0 & \mathbf{R}_i & \mathbf{R}_i \\ \mathbf{I} & 0 & 0 & \ldots & 0 & 0 & 0 \\ 0 & \mathbf{I} & 0 & \ldots & 0 & 0 & 0 \\ \vdots & \vdots & \vdots & \ddots & \vdots & \vdots & \vdots \\ 0 & 0 & 0 & \ldots & \mathbf{I} & 0 & 0 \\ 0 & 0 & 0 & \ldots & 0 & \mathbf{I} & 0 \end{bmatrix} \tag{2.32}$$

The last couple of steps are to determine the transition matrix Φ over the principal period $\boldsymbol{\tau}$ by coupling the solution of m successive intervals as:

$$\Phi = \mathbf{Z}_{m-1}\mathbf{Z}_{m-2}\ldots\mathbf{Z}_1\mathbf{Z}_0 \tag{2.33}$$

The stability of the system is determined by investigating the eigenvalues of Φ. The system is considered to be stable if all eigenvalues are in modulus less than 1 [32, 10]. Instabilities for this periodic milling case can be of three types. The first corresponds to complex eigenvalues and of modulus larger than 1. This case is due to Hopf bifurcation and causes quasi-periodic chatter. The second option is that the eigenvalues are real and of value lower than -1, and corresponds to a flip bifurcation (or period doubling) which causes periodic chatter, [23] [30] [31]. The third option is called fold instability and occurs for real eigenvalues larger than 1 [32]. Detailed analysis on both types of bifurcations have been conducted by Kalmar-Nagy [33], Stepan [34] and Fofana [35, 36].

Full discretisation, Temporal FEA and other numerical methods

From Insperger's work on semi-discretisation methods to predict chatter, the natural follow-up would be to consider discretizing all temporal dependant factors of the characteristic DDE. This was targeted in the same publication [30] and a finite-difference formula for the derivative as per Euler's method was used. The authors developed a series of stability charts for different values of m and concluded that the semi-discretisation method was far more effective than a fully discretized one. Nevertheless, other authors have also targeted full-disctretization methods with aims of improving computational time. Contrary to Insperger's approach with a direct difference scheme, an alternative full-discretisation method was proposed based on direct integration [37]. The main difference between this method and Insperger's SDM, lie around three main points. As stated before, the full-discretisation method approximates all temporal dependant terms of the equation and not only the delayed term. Secondly, this method also approximates the periodic coefficient matrices $\mathbf{W}(t)$ and $\mathbf{V}(t)$ via a linear interpolation between boundary values instead of an average over a small time interval. Finally, the full-discretization method presents the transition state matrix Φ solely as a function of cutting speed and not depth of cut. This results in the sweeping algorithm to find transition points for a_p in the construction of a SLD, does not require repeatedly computing the matrix exponentials.

Insperger then reviewed and compared both discretization methods [38] concluding that although both 1st order SDM and full-discretisation provided similar solutions, the rate of convergence for the SDM was faster than that of FDM by an order of magnitude. Computational time, however, proved to be quicker for the latter. An important insight refers to the similarities of both methods and the capability of SDM to handle various extensions, such as varying or multiple time delay, which can be transferred onto a full method as well. This is seen, for example, in projects that target curved surfaces [39].

Higher order models have been studied to approximate the time dependant elements within each interval with different techniques. Second order approximation [40] uses a second-degree Lagrange polynomial to interpolate the state item, and linear interpolation is used to approximate the time-periodic and time delay items. An improvement was found in convergence rate when compared to SDM and first order FDM. Third order [41] and hyper-third order [42] have also been evaluated to compare convergence rates and computational time. Both studies target the time dependant factors with

a third-order Newton interpolation theory and a fourth-order least squares approximation respectively. Interestingly all these publications simulate the same cutting process in order to compare their performance. An overall conclusion around the SDM and FDM techniques is that they all present similar results for the SLD predicted, however the improvements of each study can be better represented in the computational time improvements and convergence rates.

Following with time-domain approximations to predict the stability of milling operations, Bayly et al [43] presented a method known as a *temporal finite element analysis*. The approximation is based on the assumption that time delay is that of the tooth passing period and, thus, the response has a clear separation between forced regime while the tool is in contact and free vibrations when its not. When the tool is not in contact, free vibrations are assumed and the solution for the equation of motion is known for every interval of the discrete time domain array. When the tool is in contact, the vibration displacement is approximated by trial Hermite cubic polynomial functions, which are adequate for describing approximately one wavelength of periodic motion. With this, the discrete system is constructed by setting the position and velocity at the end of one element, equal to position and velocity at the beginning of the next. Replacing this type of solution into the equations of motion leads nonzero error, which then requires a weighted residual method to set the weighted error equal to zero. This is done by using either a constant or linear function adding two more equations per discrete element. With this, a discrete mapping of the dynamical system can be constructed and the stability analysed via Floquet theory.

A series of authors have targeted this method and obtained noticeable results [44, 45]. Patel [46] expanded the work of Zatarain et al. [32, 47] and collectively have studied the influence of end mill helix angle on the presence of isolated chatter islands in a SLD. It also provides further insights on the difference between Hopf and period-doubling bifurcations. Altintas and Campomanes [48] used the method to model very low radial engagement operations and defined a non-dimensional chatter coefficient.

A different approach to numerical time-domain simulations is that proposed by Zatarain [49] dubbed implicit subspace iteration. This is a time domain integration method which consists on numerically integrating the dynamic equations of the system in short time steps. The stability of a milling process is also based on the Floquet theorem, however this methods avoids the explicit use of the transition matrix and instead uses both step matrices for each time segment, and iterative determination of

dominant eigenvalues, rather than the eigenvectors of the transition matrix. In effect, further computational efficiency can be gained.

Further models have been identified and are worth mentioning. These include the Classic Runge-Kutta method [50] and a generalised form [51]. Also Lehotzky and Stepan's spectral element method [52] has shown some advances in the determination of SDOF and 2DOF milling stability calculations with improved convergence rates.

2.2 Chatter avoidance in flexible parts

Chatter is a well established limiting factor in productivity and avoiding its presence is a task that most subtractive manufacturing companies must tackle. In the more than 50 years that chatter has been reportedly studied as a engineering challenge, thousands of publications and articles have been published. As of January 2024, a quick Scopus search of *"Machining AND Chatter"* limited to engineering, results in over 3470 articles, with over 1900 articles in the last 5 years. These figures evidence the broad scale and popularity of the topic.

With this in mind, this section does not aim at providing a detailed analysis of the complete field, but rather focusing on articles centred on the workpiece's dynamic response influence on chatter and workholding based mitigation strategies. Some iconic publications have already targeted part of this topic, such as the Munoa et al. 2016 review [53] which covered well over 300 publications covering chatter suppression techniques. It highlights thin wall and flexible parts machining as a current and future driver for chatter suppression research, and dedicates a section to reviewing some approaches employed to improve machinability.

Studies that cover flexible workpieces and thin wall commonly employ an FEA integration for determination of pose dependant SLDs and adaptation of cutting strategies [54, 55, 56, 57].

Other approaches include the implementation of active and passive damping elements on the system to alter the response of the workpiece. On the first approach, active dampers use sensors and actuators in a feedback loop to continuously oppose and suppress vibrations. Semi-active approaches, on the other hand, use a feedback loop to tune dampers and provide passive damping. The implementation of these approaches have been developed both for workholding solutions [58, 59, 60], as well as portable devices that attach to the workpiece [61]. In these cases, the active dampers use a

feedback loop to constantly monitor and adapt the control parameters, either using electromagnetic or piezoelectric actuators. Semi-active and passive approaches, on the other hand are also commonly based in tuned mass damping suppression strategy without the need of feedback loops and actuators.[62, 63].

2.2.1 Fixture design approaches

Given that the focus of this Thesis is centred on the workholding effect for machining stability, a deeper insight on research focusing on fixture layouts for chatter avoidance and mitigation is critical. The active and damping strategies discussed previously can also be found in this field, by means of active and intelligent fixturing systems [64]. The review article of Bakker et al. [65] cover the main aspects of active fixture design, including re-configurable solutions and embedded control systems. Some relevant projects include Rashid and Nicolescu's work [66] on developing active vibration control on a palletized workholding system using piezo-ceramic stacks embedded within a steel frame, as well as the semi-active tuned mass damper attachment for modular fixturing system developed by Munoa et al. [67].

Within this realm of research, a particularly noteworthy research project is that of INTEFIX [68]. This multidisciplinary project was aimed at improving the development of intelligent fixtures for low rigidity components, and included topics in vibration, deformation and positioning aspects. The vibration chapter studies active vibration damping approaches for active clamping solutions, similarly to those described previously [68]. In addition, the deformation chapter presents a floating clamp fixture design that allows for residual stress deformation detection and adjustment. This approach can sense the strain buildup and actively adapt its clamping configuration to compensate and avoid spring-back. The authors realise the flexible nature of the system and conduct modal testing of the frame, both from an FEA perspective and experimentally. Their correlation is reportedly low due to oversimplifications in the FE models for joint interfaces and the consequential omission of model updating. Nevertheless, dynamic stability analysis is performed on the assembled system for a different machined states of the component highlighting the variable nature of the dynamic response. Despite these interesting results, the tooling vibration was deemed as the limiting factor in the cutting stability of the system.

A broad series of publications have targeted fixture layout optimisation with emphasis on minimising clamping distortion and form errors, using diverse reasoning

technologies such as genetic algorithms, ant colony algorithms and neural networks [69, 70, 71].

The review paper by Vasundara [72] clearly states that most of the efforts in fixture layout optimisation are targeting: workpiece clamping deformations, clamping sequences, minimisation of location errors, and fixture optimisation using evolutionary techniques. The review by Boyle [2] also concludes in a drive to improve and fixture structure stiffness estimations for computer-aided design studies. Similarly, in Li's work [73] which considers variable stiffness structure workpieces, the inclusion of dynamic force milling models is proposed as a future development.

Melkote and Deng have generated a series of publications optimising fixture layouts, and in some cases have targeted dynamic stability [74, 75]. These publications reviewed the minimum clamping forces needed, and although they considered the variation in the workpiece's FRF, they did not include cutting tool FRFs, SLD generation or process parameter identification for stable milling, and thus maintained the cutting speeds, feeds and depths of cut without consideration of regenerative chatter.

Newer studies on fixture optimisation consider static loads for topological optimisation, but do not include dynamic aspects [76]. Other research on feature-based design methodologies for aircraft structures also ignore dynamic aspects of the workpiece and cutting tool for the automation of fixture layouts based on a defined set of rules and minimal user interaction [77].

An interesting set of publications have compared different techniques for layout optimisation [78], comparing genetic algorithm approaches to particle swarm optimisation methods, the main optimisation solvers used in this area [74, 79, 69, 70]. The study concludes in favour of PSO methods over genetic algorithms for both result accuracy as well as convergence times. In these cases, fitness functions revolve around static deflection and stiffness metrics rather than evaluating dynamic response in a range of excitation frequencies. The first approach is justifiable for thin wall form errors, however these results may not be applicable for chatter avoidance of flexible parts.

Focusing on the contact modelling between workpiece and fixture, the study by Satyanarayana and Melkote [80] proposes a FE approach to improve modelling of boundary conditions and contact between workpiece and fixturing elements.

In summary, fixture layout and optimisation studies comprise a broad field that has mainly targeted clamping distortion issues and static form error, and few studies include regenerative chatter considerations in their optimisation routines. Most of the

articles also review external locators and clamps, while fewer studies focusing on the interfaces between stock and end component have been found. For effects of enabling double sided access to workpieces this area of research can provide a fundamental starting point to address stability in reduced fixture machining scenarios. Methodologies to part-off finished elements can be improved by machining dynamics research as finishing passes are critical stages that must ensure conforming dimensional and surface requirements. This topic does not have an evident body of publications and no articles were found which target this specific set of operations. This proposes novel research avenues to complement the few articles targeting workholding optimisation based on machining stability metrics, and also apply this approach on finishing stages and parting-off routines.

2.3 Double sided environments

One last area to review is double sided machining environments and opposing multi-spindle machining strategies. Some developments in this field target dynamic behaviour of opposed spindle milling (OSM). This approach is also referred to as pinch milling, mirror milling, duplex milling or simultaneous double-sided milling. The presence of two cutting tools working simultaneously on a component requires new approaches for the development of chatter prediction. The work done Olgac [81] is one of the first approaches at characterising the multiple spindle case, for both parallel and opposed milling. The works by Brecher [82], Budak [83] and Shamoto [84] have provided valuable guidelines to improve stability in OSM environments by targeting relative phase angle between units or spindle speeds of each tool. In the Shamoto study [84], the authors acknowledge the influence of workpiece dynamics and its dependence on fixturing setup, however no predictive methods are implemented to improve the dynamic response of the workpiece. Their chatter prediction method is based exclusively on experimental FRFs of the workpiece.

Double sided environments have also been useful to implement external damping onto the part by means of robotic assisted damping [85, 86]. Similarly, the 2019 study by Barrios et al. [87] uses an external robot to locally increase the stiffness of thin walled parts. Experimentally validated predictive models based on receptance coupling are able to analyse the dynamic response of the robot and part union. This type of research reaffirms potential benefits of exposing both main faces of a billet or component and allowing for the convenient implementation of external damping solutions and enhanced process monitoring utilities.

Particularly relevant to this project is the study by Fu et al. [1] which targets double-sided milling with parallel kinematic machines. Their study covers cutting operation sequencing, as well as chatter and machining stability. It highlights the importance of workpiece dynamics and provides experimental measurements in the out-of-plane direction (axial to the cutting tool), assuming rigid conditions for the other directions. An interesting aspect of this test is the consideration of support one machine provides on the workpiece as the other is cutting. The authors test this by running a shallow 0.5mm slot on one face of the workpiece and then moving the machine forward until a 50μm deflection is observed. This scenario is considered representative of the in-process tool/workpiece interaction and EMA data is extracted. The main result stemming from this work is a comparative improvement in surface quality (roughness and form deviation) when machining the double-sided part using both machines synchronised on either sides, rather than sequentially (i.e. machining one side at a time).

2.4 Summary

This chapter has firstly reviewed the main models employed to understand and predict the presence of chatter. This allows to establish the key variables that govern the system and construct a feedback loop to link each of them. Two methods to compute the stability lobe diagram of a milling operation are described, the zeroeth order Fourier approximation (ZOA) and the semi-discretisation method (SDM). Secondly, this chapter has also reviewed relevant literature that target chatter avoidance and suppression in flexible parts, and focuses on fixture design and optimisation studies. A brief review of double sided machining environments complements the latter and highlights both the potential benefits, but also the increased challenges associated with this type of approach. In conclusion, Chapter 2 has allowed to uncover interesting and novel avenues of research which target external and internal workholding layout optimisation by using receptance and stable depth of cut values as guiding metrics. This will combine the fields of machining dynamics, workpiece chatter and fixture layout optimisation into a single body of work, making use of chatter prediction methods and FEA dynamic models to guide a numerical optimisation program targeting workholding layouts.

Chapter 3

Background

This chapter specifies the mathematical, physical and computational procedures employed to develop and evaluate workpiece dynamic response and workholding layout optimisations. The first section presents a brief compendium classical mathematical approaches of modal analysis. It covers temporal, spatial and frequency domain expressions for both analytical and experimental evaluation of dynamic systems. From this formal base, the following section centres on the finite element analysis (FEA) method for numerical simulations.

With these first sections providing a concise and robust mathematical basis to study dynamical systems both analytically as well as numerically, a FEA framework is established in Figure 3.1. It depicts the process by which the FEA approach is used to incorporate analytical, numerical and experimental results for model validation. Section 3.3 covers experimental modal analysis topics. Based on the analytical concepts of the preceding sections, it specifies the procedure of extracting modal data of an unvalidated model to guide the design of experimental tests. Details of instrumentation and data processing these physical results are also covered in this section, in order to provide a correlation between model and physical part. The final section highlights the importance of model updating and the approach used to validate a model.

Understanding the modal analysis field from analytical, experimental and numerical approaches is paramount for the development of this Thesis. Making use of FEA models to numerically simulate the behaviour of dynamical systems [4] is central to this work and acute understanding of the method is therefore required. In order to improve the predictive capability of each model and reduce discrepancies to the physical system (either due to uncertainties in material properties, boundary conditions,

and other factors), EMA testing can then provide valuable information about the dynamic characteristics of the physical setup and be used to update FEA models. The goal of model updating is to improve the accuracy of the FEA model by adjusting its parameters to better match the experimental results. A validated model can then be utilised to further examine its modal parameters and derive valuable information of its dynamic response.

3.1 Modal Analysis

Modal analysis is a powerful technique to aid the understanding and description of the dynamic behaviour of structures and mechanical systems [88]. One of the main benefits provided by modal analysis is its capability to uncouple the ordinary differential equations of motion, and express the system as a linear combination of its normal modes [4].

In order to review these approaches, the most common description of the equations of motion for a structure with n degrees-of-freedom (DOFs) is that of Equation (2.2):

$$[M]\{\ddot{x}(t)\} + [C]\{\dot{x}(t)\} + [K]\{x(t)\} = \{F(t)\} \tag{3.1}$$

Where $[M]$, $[C]$ and $[K]$ are $n \times n$ square matrices for mass, damping and stiffness respectively. Acceleration, velocity and displacement are expressed as a function of time via $n \times 1$ vectors $\{\ddot{x}(t)\}$, $\{\dot{x}(t)\}$ and $\{x(t)\}$. The last term of the equation is $\{F(t)\}$, which represents the $n \times 1$ vector of the input forces. The symmetry and off-diagonal behaviour of the matrices M, C and K will depend on the coupling of degrees of freedom. As the complexity of the physical system increases, *modal analysis* offers a convenient evaluation method.

The most common approach to introduce this topic is to evaluate first the free vibration of undamped systems. The following set of equations are adapted from [4] and [89]:

$$[M]\{\ddot{x}(t)\} + [K]\{x(t)\} = 0 \tag{3.2}$$

Has solutions of the form:

$$x(t) = \mathbf{u}e^{i\omega t} \tag{3.3}$$

Where u is a non-zero vector of constants of dimension N, and ω is a non-zero frequency. Note that Eq. (3.2) describes a harmonic movement. Pre-multiplying the

reduced form of Eq. (3.1) by M^{-1}, and using a solution according to Eq. (3.3) we obtain:

$$([M^{-1}][K] - \omega^2 I)\mathbf{u} = 0 \tag{3.4}$$

This is an eigenvalue/eigenvector problem ($A\mathbf{u} = \lambda\mathbf{u}$) where the scalar eigenvalue is related to the mode frequency defined by $\lambda = \omega^2$, and the eigenvector is related to the mode shape $\mathbf{u}$, defined by the matrix $A = M^{-1}K$. Given that, mode shapes can have an arbitrary magnitude, it's common to normalise these using the Euclidian norm for the $\mathbb{R}^n$ space:

$$\|x\| = \sqrt{x^T x} = \left[\sum_i {x_i}^2\right]^{1/2} \tag{3.5}$$

An important characteristic of mode shapes is their orthogonality to both mass and stiffness matrices. This property can be used to uncouple each equation of motion. Using two arbitrary modes r and s, then Eq. (3.3) can be rearranged to:

$$K\mathbf{u_r} = {\omega_r}^2 M\mathbf{u_r} \tag{3.6a}$$

$$K\mathbf{u_s} = {\omega_s}^2 M\mathbf{u_s} \tag{3.6b}$$

Pre-multiplying the first equation by ${\mathbf{u_s}}^T$ and the second by ${\mathbf{u_r}}^T$, yields:

$${\mathbf{u_s}}^T K\mathbf{u_r} = {\omega_r}^2 {\mathbf{u_s}}^T M\mathbf{u_r} \tag{3.7a}$$

$${\mathbf{u_r}}^T K\mathbf{u_s} = {\omega_s}^2 {\mathbf{u_r}}^T M\mathbf{u_s} \tag{3.7b}$$

Transposing Eq. (3.7b) and subtracting it from Eq. (3.7a) results in:

$$({\omega_r}^2 - {\omega_s}^2){\mathbf{u_s}}^T M\mathbf{u_r} = 0 \tag{3.8}$$

This yields two possibilities:

$${\mathbf{u_s}}^T M\mathbf{u_r} = 0 \qquad r \neq s \tag{3.9a}$$

$${\mathbf{u_s}}^T M\mathbf{u_r} \neq 0 \qquad r = s \tag{3.9b}$$

These expressions show that mode shapes are orthogonal to the mass matrix (also stiffness) and that the product of the mode shape with the matrix is non-zero. This product is defined as the generalised mass m_{ii} and similarly the generalised stiffness k_{ii} in the ith normal mode:

$$m_{ii} = {\mathbf{u_i}}^T M\mathbf{u_i} \tag{3.10a}$$

$$k_{ii} = {\mathbf{u_i}}^T K\mathbf{u_i} \tag{3.10b}$$

Given the arbitrary normalisation of the mode shapes, the values of m_{ii} and k_{ii} are not unique. However, it is provable that k_{ii}/m_{ii} is unique of value ${\omega_i}^2$ (chapter 6.11 of [4]).

The most common normalistaion approach is on mass and therefore $m_{ii} := 1$ and consequently, $k_{ii} = \omega_i^2$. Defining $P = [\mathbf{u_1 u_2 ... u_n}]$ as the mode shape matrix, the diagonal modal mass and stiffness matrices (m and k respectively) are defined as:

$$m = P^T M P \tag{3.11a}$$

$$k = P^T K P \tag{3.11b}$$

Finally, the modal transformation $x = Py$ for the undamped case can be reduced to:

$$P^T M P \ddot{y} + P^T K P y = 0 \tag{3.12a}$$

$$\Leftrightarrow \quad m\ddot{y} + ky = 0 \tag{3.12b}$$

Introducing the mass normalised definition mentioned previously results in the well-known harmonic modal differential equation:

$$\ddot{y}_i + \omega_i^2 y = 0 \tag{3.13}$$

The temporal initialisation conditions must also be transformed into the new modal coordinate system $y(t)$ by using the original $x(t)$ through:

$$y_0 = P^T M x_0 \tag{3.14a}$$

$$\dot{y}_0 = P^T M v_0 \tag{3.14b}$$

Once these solutions are calculated, the general solution is the superposition of modal solutions, thus:

$$x(t) = Py(t) = \sum_{i=1}^{n} \mathbf{u_i} y_i(t) = \sum_{i=1}^{n} \mathbf{u_i} d_i \sin(\omega_i t + \phi_i) \tag{3.15}$$

When expressing the solution as a sine function, the factors d_i are determined by the temporal initialisation conditions and are called modal participation factors.

In the situations where the system is unrestrained, the case where $\omega = 0$ can yield solutions in the form $y(t) = \alpha + \beta t$. This type of solution describes a *rigid-body* translation. In this case, the undamped system can be determined to have rigid body modes if the determinant of matrix $[K]$ is zero [4]. It is important to note that for

any mDOF system, there can only be six rigid body modes. For each of the three Cartesian directions, there is a translational and rotational rigid-body mode.

In order to introduce damping to this analysis, it is important to first acknowledge that damping is a deep and complex field due to the fact that the physics behind damping mechanisms vary considerably compared to the inertial and stiffness forces [90]. In vibration systems, damping can be any model the dissipates energy, and can therefore present a broad range of underlying mechanisms including heat, sound, inelastic collisions, friction and many others [91, 92]. The most common approaches to model damping, is to assume a *viscous* linear model, where damping is solely dependant on the instantaneous velocities, a model that has been used for over a hundred years since its introduction by Lord Rayleigh in 1877 [93]. This definition of damping also involves a proportional condition in order to express it as a linear combination of the mass and stiffness matrices, as per Eq. (3.16), however both Caughey [94] and Adhikari [95] have expanded on a generalised proportional damping condition that extends beyond the scope of this section. This collective type of damping models are such that the matrix $[C]$ of Eq. (3.1) can be written as:

$$[C] = \alpha[M] + \beta[K] \tag{3.16}$$

These types of damping models are particularly useful for the application of modal analysis, given that the eigenvectors are identical to those of the undamped case [89], $P_{damped} = P_{undamped}$. Using this to uncouple the physical domain equations of motion and express them in modal coordinates:

$$m\ddot{y} + (\alpha m + \beta k)\dot{y} + ky = 0 \tag{3.17}$$

Mass normalising, the modal equations are reduced to:

$$\ddot{y}_i + \underbrace{(\alpha + \beta\omega_i^2)}_{=2\zeta_i\omega_i}\dot{y}_i + \omega_i^2 y_i = 0 \tag{3.18}$$

The introduction of the damping term $2\zeta_i\omega_i\dot{y}_i(t)$, results in solutions analogous to the viscously damped single degree of freedom system, of the form:

$$y_i(t) = A_i e^{-\zeta_i\omega_i t}\sin(\omega_{di}t + \phi_i) \tag{3.19}$$

With A_i and ϕ_i time initialisation dependant, and $\omega_d = \omega_i\sqrt{1-\zeta_i^2}$. ζ_i is known as the modal damping ratio for the ith normal mode.

The last step is to address the forcing term of Eq. (3.1). The modal equations of motion in this case are:

$$\ddot{y}_i + 2\zeta_i\omega_i\dot{y}_i + \omega_i^2 y_i = \bar{f}_i \tag{3.20}$$

The general solution is the sum of the transient, $x_h(t)$, and steady state, $x_p(t)$, solutions. Therefore, in the physical domain:

$$x(t) = \underbrace{\sum_{i=1}^{n} d_i e^{-\zeta_i\omega_i t}\sin(\omega_{di}t + \phi_i)\mathbf{u_i}}_{=x_h(t)} + \underbrace{Py_p(t)}_{=x_p(t)} \tag{3.21}$$

The physical and modal approaches to modelling the dynamic behaviour can be further complemented by using frequency domain analysis, particularly for sparse harmonic excitations of the form $F(t) = F_0 e^{j\omega t}$. This frequency domain model stems from the application of a Fourier transform to each degree of freedom in the system [89], and the expectation of particular solutions being of the form $x(t) = Xe^{j\omega t}$.

For an arbitrary function $g(t)$, the Fourier transform is defined as:

$$\mathbf{G}(j\omega) = \int_{-\infty}^{\infty} g(t)e^{-j\omega t}dt \tag{3.22}$$

This is a linear transformation, which then maintains the principle of superposition for each degree of freedom in the system. Therefore, Eq. (3.1) can be re-written as:

$$\underbrace{\left[-\omega^2 M + j\omega C + K\right]}_{\text{dynamic stiffness}}\mathbf{X}(j\omega) = \mathbf{F}(j\omega) \tag{3.23}$$

The more convenient way to express this equation is by defining the receptance of the system (or frequency response function, FRF) as:

$$\mathbf{H}(j\omega) = \frac{\mathbf{X}(j\omega)}{\mathbf{F}(j\omega)} = \left[-\omega^2 M + j\omega C + K\right]^{-1} \tag{3.24}$$

Again, matrices M, C, K have dimensions $n \times n$ and therefore the receptance matrix $\mathbf{H}(j\omega)$ does so as well.

Applying the Fourier transform on the the modal analysis approach on this system, and using variable $r_i = \omega/\omega_i$, Equation (3.20) can be expressed as:

$$\frac{\mathbf{Y_i}(j\omega)}{\bar{\mathbf{F}}_\mathbf{i}(j\omega)} = \frac{1}{k_{ii}}\left(\frac{(1-r_i^2) - j(2\zeta_i r_i)}{(1-r_i^2)^2 + (2\zeta_i r_i)^2}\right) \tag{3.25}$$

This expression corresponds to the complex frequency response function of the steady state responses in frequency domain. This expression is complemented by representation of its magnitude and phase, Eqs. (3.26a) and (3.26b), or by its real and imaginary components, Eqs. (3.26c) and (3.26d), as follows:

$$\left|\frac{Y}{F}\right| = \frac{1}{k}\sqrt{\frac{1}{(1-r_i^2)^2 + (2\zeta_i r_i)^2}} \tag{3.26a}$$

$$\Phi = \tan^{-1}\left(-\frac{2\zeta_i r_i}{1-r_i^2}\right) \tag{3.26b}$$

$$Re\left(\frac{Y}{F}\right) = \frac{1}{k}\left(\frac{1-r_i^2}{(1-r_i^2)^2 + (2\zeta_i r_i)^2}\right) \tag{3.26c}$$

$$Re\left(\frac{Y}{F}\right) = \frac{1}{k}\left(\frac{-2\zeta_i r_i}{(1-r_i^2)^2 + (2\zeta_i r_i)^2}\right) \tag{3.26d}$$

The final step in the frequency domain analysis is to link the modal form back to the physical domain. Using the coordinate transform $x = Py$ it can determined that the direct FRF is a sum of modal contributions, factored by the mass-normalised mode shape matrix P. With this,

$$H_{rs}(j\omega) = \sum_{i=1}^{n} \frac{\mathbf{u_i}(x_r)\mathbf{u_i}(x_s)}{-\omega^2 + 2j\zeta_i\omega_i\omega + \omega_i^2} \tag{3.27}$$

This expression defines each individual term of the receptance FRF matrix, where x_r is the input location and x_s is the output location. The diagonal terms are commonly referred to as direct-FRFs (or driving point), whereas the off diagonal terms are labelled cross-FRFs. An alternative notation for Equation (3.27) introduces the concept of *residue* or modal constant, $R_{rs,i}$, which relates locations r and s for the i^{th} mode as:

$$H_{rs}(j\omega) = \sum_{i=1}^{n} \frac{R_{rs,i}}{-\omega^2 + 2j\zeta_i\omega_i\omega + \omega_i^2} \tag{3.28}$$

A final approach to evaluating dynamic systems is similar to the Fourier approach, but instead using a Laplace transform. For this, the solution to the free vibration case of Eq. (3.1) is assumed of the form $x(t) = Ce^{st}$, where s is a complex number to be determined [4]. This can be expressed as:

$$\underbrace{\left([M]s^2 + [C]s + [K]\right)}_{=D(s)} Ce^{st} = 0 \tag{3.29}$$

The non-trivial solution implies the determinant of $D(s)$ is set to zero, defining the *characteristic equation* as:

$$|D(s)| = \left|[M]s^2 + [C]s + [K]\right| = 0 \tag{3.30}$$

In this case, the complex eigenvalues are paired with their complex conjugate and the total number is twice that of the degrees of freedom of the system. Therefore the eigenvalues are expressed as:

$$\lambda_i = \sigma_i + j\omega_i; \qquad \lambda_i^* = \sigma_i - j\omega_i \qquad \forall i \in [1, n] \tag{3.31}$$

σ_i is defined as the modal damping of the system, and ω_i the damped natural frequency. The real eigenvector for each eigenvalue is obtained by solving Eq. (3.29). These three parameters, are known as the modal parameters of the system.

One last expansion on this approach is expressing a solution for Eq. (3.30) as a polynomial expansion, which again is of order $m = 2n$ and expressed as:

$$|D(s)| = a_0 s^m + a_1 s^{m-1} + a_2 s^{m-2} + ... + a_{m-1} s + a_m = 0 \tag{3.32}$$

The stability of the system can then be evaluated by looking at the roots of the polynomial expression, $s_i = \sigma_i + j\omega_i$ [4]. If the real part of **any** roots is positive, i.e. positive damping, then the solution will contain an increasing exponential term $e^{\sigma_i t}$ and the solution is considered to be unstable. On the contrary, if **all** modal damping parameters are negative, then time decaying functions are obtained and the solution is considered stable. In the case that a pure imaginary root is found, this yields a pure oscillatory solution. However, if it is a multiple root, then solutions would have time increasing terms and the system is deemed unstable. Then for a linear system to be considered stable it would require all roots of its characteristic equations to have negative valued real parts, and not have pure imaginary multiple roots.

In summary, this subsection provides an in-depth derivation of the main expressions that aid the understanding of dynamic systems. Useful benefits can be obtained by transforming the physical time domain model into modal coordinates and uncouple the equations of motion into a set of ordinary differential equations. These are defined by specific mode frequencies and damping values. Alternatively, the use of a frequency domain analysis is particularly useful to determine receptances and frequency response functions of a system with harmonic excitation. These three approaches are commonly used in a complementary manner, each targeting specific aspects and increase the understanding and of the dynamic behaviour of the system. Lastly, a brief description of stability evaluation is presented.

3.2 FEA Modelling

The finite element method is a powerful numerical interpolation technique used for analysing complex systems in engineering and physics. Focusing on structural dynamics, this method is particularly useful to study the behaviour of non-trivial continuous structures where mathematical and analytical solutions are unattainable [96].

In order to study realistic models of complex structures, computational approximations can be established by means of spatial *discretisation* into a *finite* number of subdivisions. These *elements* are defined by a set of spatial points on the vertices, called *nodes*, some of which also serve to define adjacent elements, boundary conditions, or both. Depending on the nature of the problem to solve, a set of equations is defined for each element and subsequently assembled into a matrix form. In the dynamic evaluation case, the equations are commonly derived from the Lagrange method (also widely applied in analytical approaches to derive equations of motion) [4]. The Lagrangian is defined as:

$$L = T - V \tag{3.33}$$

Where T and V are the kinetic and potential energy respectively. The Lagrange equation implies that:

$$\frac{d}{dt}\left(\frac{\partial T}{\partial \dot{x}_i}\right) - \frac{\partial T}{\partial x_i} + \frac{\partial V}{\partial x_i} = F_i \tag{3.34}$$

In this equation, x_i are the generalised coordinates and F_i accounts for non-conservative forces acting on the system.

The displacement for an element,$w(x,t)$ can be expressed in terms of the displacement at each of its joints (i) as:

$$w(x,t) = \sum_{i=1}^{n} N_i(x) w_i(t) \tag{3.35}$$

Where n is the number of joint displacements and $N_i(x)$ is the shape function associated to joint displacement $w_i(t)$ [4]. Defining the vector of joint displacements as $W = w_i$, kinetic energy and potential energy for the element can be expressed as:

$$T = \frac{1}{2}\dot{W}^T[m_e]\dot{W} \tag{3.36a}$$

$$V = \frac{1}{2}W^T[k_e]W \tag{3.36b}$$

Substitution in Eq. (3.34) yields:

$$[m_e]\ddot{W} + [k_e]W = f \tag{3.37}$$

Where f in this case is the vector of joint forces applied onto the element and $[\bar{m_e}]$ and $[\bar{k_e}]$ are the mass and stiffness matrices for the element. It is useful to note that depending on the type of element and application, the amount of joint displacements can vary.

The next step is to assemble all the equations of motions for each element onto a global mass, stiffness and damping matrix for the complete system. Two coinciding methods arrive at the same solution using slightly different approaches. The first is via the introduction of an element specific rectangular matrix that isolates its joint displacements. The other is by defining the transformation matrix of the local element coordinate system onto the global coordinates. Both methods are described in chapter 12.5 of [4]. A brief description of the first method starts by defining the global joint displacement as:

$$\mathbf{U}(t) = \begin{Bmatrix} U_1(t) \\ U_2(t) \\ \vdots \\ U_N(t) \end{Bmatrix} \tag{3.38}$$

In this case the element joint displacements are expressed in global coordinates U_i rather than the local coordinates used for the single element in the previous section (W_i), and N is the total number of joint displacements . The element specific matrix in this case is defined for element e as:

$$[A^{(e)}] = A^e_{ij} = \begin{cases} 1, & w_i \in U^{(e)} \wedge j \in [1, n] \\ 0 & \text{otherwise} \end{cases} \tag{3.39}$$

$A^{(e)}$ is a $n \times N$ matrix of zeros and ones which yields $U^{(e)} = A^{(e)}\mathbf{U}(t)$. With this definition the total kinetic energy can be defined as the sum for the energy for the total number of elements E, and therefore:

$$T = \sum_{e=1}^{E} \frac{1}{2} \dot{U}^{(e)T} [\bar{m_e}] \dot{U}^{(e)T} \tag{3.40}$$

Introducing $A^{(e)}$:

$$T = \frac{1}{2} \sum_{e=1}^{E} \dot{\mathbf{U}}^T [A^{(e)}]^T [\bar{m_e}] [A^{(e)}] \dot{\mathbf{U}} \tag{3.41}$$

From here stems the crucial definition of the *mass matrix*, $\mathbf{M}$ of the complete structure:

$$[\mathbf{M}] = \sum_{e=1}^{E} [A^{(e)}]^T [\bar{m}_e][A^{(e)}] \tag{3.42}$$

And similarly, strain energy derives the expression for the *stiffness matrix* of the structure [88] as:

$$[\mathbf{K}] = \sum_{e=1}^{E} [A^{(e)}]^T [\bar{k}_e][A^{(e)}] \tag{3.43}$$

FEA has proven to be a powerful and useful numerical approximation tool for engineering and physics applications and has therefore seen numerous private and commercial software developments [88]. Codes such as ABAQUS, ANSYS, ADINA or NASTRAN have implemented GUIs and offer an extensive set of element libraries and are able to simulate diverse multi-physics problems, combining different fields onto the same evaluation process. In this study, both ABAQUS and FEMTOOLS are available resources for implementation of FEA simulations. A brief comparison on performance is provided in Section 5.2.1. In either case, the process to set up a model can broadly be summarised as [88]:

1. Structure discretisation and geometrical definition of elements.
2. Determination of approximate solutions for each element based on joint and nodal values.
3. Assembly and introduction of continuity and boundary conditions, as well as external loads.
4. Derivation of system of equations.
5. Solving of assembled system.
6. Post processing, if any additional variable is required.

Focusing now on the FEA solver engine, the most common solver for the eigenvalue problem is the *Lanczos* algorithm [97]. This method is oftentimes preferred for its ability to extract a given amount of lowest valued eigenvalues, in the least number of iterations.

As stated previously, in the proportional damping scenario, the damped and undamped eigenvectors are identical. Matrix $[K]$ of Equation (3.4) can be expressed in

a Cholesky decomposition form, $[K] = [L][L]^T$. This can only be done if the stiffness matrix does not have rigid-body modes (i.e. a positive semi-definite with no decomposition). The number of requested eigenvalues has to be from the lowest end of the spectrum. This can pose additional challenges if the structure is expected to present all or some of the six rigid body modes, or if a high number of flexible modes are under the relevant frequency band for the study. The latter point is particularly relevant in scenarios where the forcing frequency is high compared to the first modes of the structure, as could be high-speed milling of flexible structures. Nevertheless a spectral transformation method allows the Lanczos solver to treat the system as a shifted problem to a certain extent and accommodate for this issue [98]. Using the definition of $[L]$ and a series of algebraic steps, the problem can be solved by QR decomposition of an orthogonal matrix $[Q]$ and an upper triangular matrix $[R]$ that contains the eigenvalues on the diagonal. Inverse power iterative method is used to extract the eigenvectors [98].

Having the theoretical basis for how dynamic analysis FEA systems work, the following sections describe the each aspect of the modelling framework within this project. Figure 3.1 presents the process by which a model is set up and used to determine experimental procedures to evaluate a physical counterpart of the system.

The first quadrant of Figure 3.1 is the FEA modelling group which is in charge of generating a computer based dynamic analysis of the system, specifically based on an *input file (*.inp)*, which is used by the FEA solver to generate the model. This type of file is a native extension to ABAQUS FEA Software, however it can also be accessed by other FE solvers as well. The benefit of using **.inp* files is the flexibility within these two platforms; using ABAQUS to generate and evaluate meshes, and FEMTOOLS to script the automated dynamic evaluation of the components and updating routines.

An example of a **.inp* file is presented in Listing 3.1. After the main header, nodes are listed in a 4 column matrix with node numbers and X Y Z coordinate positions. Then elements are defined by type and composing nodes. A *section* is defined by type, element set and material, properties of which include density, elastic modulus and Poisson ratio. The solvers used to process the **.inp* files have no native units and consistency must then be extended to all parameters. In this case, all applications employ the SI(mm) units, which can be summarised in Table 3.1.

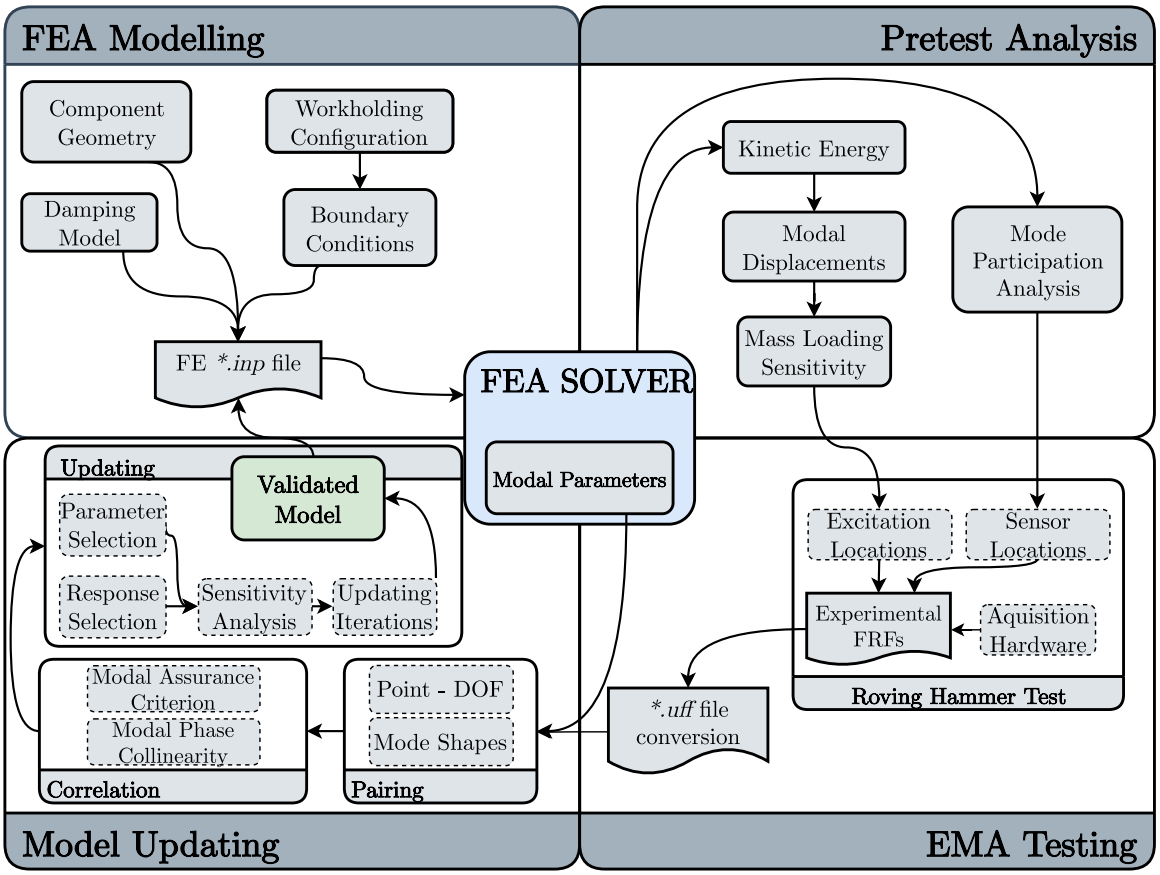

Figure 3.1: FEA Framework

Quantity	**SI(mm)**
Length	mm
Force	N
Mass	Tonne (10^3 kg)
Time	s
Stress	MPa
Energy	mJ (10^{-3} J)
Density	Tonne/mm^3

Table 3.1: Consistent Units

These types of files offer a direct way of extracting and modifying parameters for the FEA solvers, and re-writing new versions of the file to suit specific needs.

3.2.1 Meshing

Initialisation of a model requires the definition of the physical setup to evaluate and specifications of its geometry, material and workholding configuration. With this

```
*Heading
** Job name: BaseBillet Model name: Billet
** Generated by: Abaqus/CAE 2018
*Preprint, echo=NO, model=NO, history=NO, contact=NO
** PARTS
*Part, name=Billet
*Node
      1,         -350.,         -250.,           60.
      2,         -350.,          250.,           60.
      3,         -350.,          250.,            0.
      4,         -350.,         -250.,            0.
      ...
*Element, type=C3D10
    1,  2113,  2114,  2115,  2116,  3906,  3905,  3904,  3908,
   3907,  3909
    2,  1727,  2117,  1751,  2118,  3912,  3911,  3910,  3914,
   3913,  3915
    3,  2113,   843,  2119,  2120,  3918,  3917,  3916,  3920,
   3919,  3921
    ...
*Nset, nset=Set-1, generate
     1,  26675,      1
*Elset, elset=Set-1, generate
     1,  16760,      1
** Section: Section-1
*Solid Section, elset=Set-1, material=Al7050
,
*End Part
**
** MATERIALS
*Material, name=Al7050
*Density
 2.83e-09,
*Elastic
68947., 0.33
```

Listing 3.1: **.inp* file example

information, a CAD **.step* model replicates the setup and a finite element *mesh* is generated. Meshing is a critical step in the definition of an FE model, as the accuracy and performance of the solver depends directly on the mesh parameters [96]. As a brief summary, the main parameters that define FE meshes are:

1. Element Type: Elements are the fundamental discretization unit of the domain, which tend to be well defined simple geometric shapes [88]. These can take forms in all spatial dimensions depending on the application of the model, computational time availability and spatial aspect ratios. Further subdivision of element types can be determined by the number of nodes that defines each element.

For effects of this research, all meshes are generated using solid based elements (3D), of both the tetrahedral family TET4, TET10 (or C3D10) and linear brick elements C3D8, depending on the component and application.

2. Mesh Density: This factor relates to the size of the elements within the mesh, particularly around edges and corners, as well as other stress raisers like grooves, holes or notches. Localised refinement of a mesh around these key features is a common practice within FE analysis to ensure accuracy and numerical convergence.

   Guidelines on meshing procedures can be found in ABAQUS CAE 2018 documentation resource within the software, as well as troubleshooting with [99].

3. Mesh Quality: There are several metrics employed to evaluate the quality of a mesh. Native mesh analysis in both ABAQUS and FEMTOOLS provide verification functionalities tools and the ability to quantify the quality of a mesh. This ensures corrective measures are implemented before modelling, and metrics are kept within accepted values. The main metrics employed are:

   - Aspect ratio
   - Convexity
   - Quality Factor
   - Maximum Corner Angle
   - Taper
   - Warp angle

As mentioned before, the meshing procedures in this work are performed in ABAQUS given its ample capabilities to manipulate and control mesh generation. The final result of meshing is exporting as an **.inp* file, which can be accessed by FEMTOOLS.

3.2.2 Boundary Conditions

The physical constraints experienced by the component are modelled in FEA as boundary conditions (BC), and mainly prescribe displacement limits on any of the 6 DOFs a node has. The BCs can take different names depending on which DOF are restricted. For example *pinned* commonly refers to a situation that allows rotations but restricts translations. Alternatively, an *encastre* restricts movement on all DOF, however different platforms can vary their naming conventions and the documentation must be examined. If no boundary conditions are defined, a *free-free* condition can be modelled. Care must be taken when evaluating this type of system as some FEA solvers can run into errors. Due to rigid body modes, the uniqueness and convergence of

frequency estimations can be problematic when translations and rotations are unrestricted for all nodes.

A common issue encountered in the definition of BC is the over-simplification of the system and the assumption that the contact point with another component or surface is ideal and inert. This assumption can hold true in cases where boundary effects are not critical, or the adjoined surface has considerably higher stiffness and mass properties than the evaluated component. It is also relevant when considering that structural damping of metallic components can be comparatively low to damping at the interfaces. In any case, the joint or contact should be carefully evaluated before being modelled as a boundary condition. In this regard, mechanical joints have been identified to have localised stiffness and damping effects on the structure, and therefore, on the local component as well [100]. To enhance modelling capabilities, some sophisticated methods have been developed which include treatment of BC as translational springs [101], or employing *thin element interface layers* to provide damping parameters [102, 103, 104]

In this research optimisation efforts for placement and layouts of workholding elements is central and therefore demands a meticulous approach and strategy to define the BCs adequately.

3.2.3 Damping

As mentioned earlier, damping is far from being a straightforward aspect to address in vibrational analysis of assembled structures. Focusing on the FEA implementation of damping, and particularly when modelling linearly elastic and isotropic materials, the two main types of damping models that are used are viscous and structural models. The first was described in Section 3.1 and the second is assumed to be proportional to displacement, disregarding frequency and known as hysteretic damping or structural damping [105]. With this, for a SDOF system the structural damping force can be expressed in terms of the stiffness k and displacement x as:

$$f_s = jdkx \tag{3.44}$$

Here d is the structural damping coefficient (or loss factor) and the j is to provide a 90 degree phase shift. To evaluate the relationship between viscous and structural damping, it can be shown [105] that by calculating a frequency ω^* such that f_s is equal to the viscous force f_v yields:

$$f_v = jc\omega^* x = jdkx = f_s$$
$$\Rightarrow c = \frac{dk}{\omega^*} = d\omega^* m \tag{3.45}$$

Introducing the damping ratio $\zeta = c/c_r$, where the critical damping for a sDOF is $c_r = 2m\omega$, then:

$$\zeta = \frac{d\omega m}{2m\omega} = \boxed{\frac{d}{2} = \zeta} \tag{3.46}$$

In order to address damping arising from mechanical joints and material interfaces, researchers have develop a broad array of models to cover single and multiple DOF system, as well as linear and non-linear damping characterisation. Rigorous definition of mechanical interface damping should be weighed against the internal damping properties of the components. In metallic structures, internal damping properties can sometimes be relatively low compared to friction based joints. Described and compared in detail in [106], a broad range of joint damping approaches are reviewed. The study also highlights that discretised mDOF models can benefit of predictive capabilities and parameter identification, however an interface representation is required and the higher number of DOF lead to computationally expensive models.

3.3 Experimental Modal Analysis

Modelling the dynamic response of structures is greatly improved when experimental data can be used to update and improve the FE model. The feedback loop between FE modelling and EMA testing begins with an non-validated FE model used to generate a pretest analysis deriving excitation and sensor locations, as well as mass loading sensitivities. This information is employed to design the experimental procedure and testing on the structure. Data collected from these tests are then processed and prepared to be reintroduced into the FEA software to link the initial model to experimental data. The quality and correlation between model and physical test is evaluated with some statistical indicators.

This section describes the methods employed to test and experimentally evaluate the dynamic response of a physical component which cover pretest analysis and correlation metrics, as well as the instrumentation, data acquisition and signal processing.

3.3.1 Pretest Analysis

Pretest analysis covers the tools used to plan and derive quantifiable information for experimental test planning. As seen in the top-right quadrant of Figure 3.1, it makes use of a baseline FE model to evaluate the effects different test setups can have on the quality of the test data and eventual correlation metrics. It includes the screening of target modes, as well as the selection and optimisation of sensor and excitation locations. Another useful evaluation of pretest analysis is to determine the effects of mass loading on the structure, namely by the presence of sensors and wiring on the component.

The pretest process employed in this research follows:

1. Target Mode Selection: Given that some modes of the structure will fall outside the frequency band of interest, a way of determining the mode shapes of interest is required. For this, *Modal Participation Analysis* (MPA) computes the relative contribution of each mode to the overall response of the system [107]. This is a useful method as it is applicable to both suspended (free/free) and constrained structures. The MPA of mode j [107] is computed using the mode shape of the at the input DOFs i, $\Phi_{i,j}$ as:

$$\mathrm{MPA}_j = \frac{\mathrm{tr}(\Phi_{i,j}\Phi_{i,j}^T)}{\mathrm{tr}(D_e)} \tag{3.47}$$

Where the matrix D_e uses the n_m modes in the frequency range of interest and is computed using [107]:

$$D_e = \sum_{j=1}^{n_m} \Phi_{i,j}\Phi_{i,j}^T \tag{3.48}$$

Finally, MPA can also compute the contribution of DOF i to the response at mode j as:.

$$\mathrm{MPA}_{i,j} = [\Phi_{i,j}^2]^T[D_e]^{-1} \tag{3.49}$$

To complement the MPA metrics, the modal kinetic energy of the structure also allows to determine whether some modes are predominantly local or global [108, 109]. In particular, a local mode usually distributes the kinetic energy in a limited number of DOFs, whereas a global mode spreads the energy distribution throughout all the DOFs. The MKE associated to the ith DOF due to the jth

mode is defined by [110]:

$$\begin{aligned} \mathrm{MKE}_{i,j} &= \Phi_{i,j} \sum_{s=1}^{n} M_{i,s} \Phi_{s,j} \\ &\propto M_{i,i} \Phi_{i,j}^2 \end{aligned} \tag{3.50}$$

Where i denotes the DOF and j the mode shape. $M_{i,i}$ is the mass matrix coefficient associated to DOF i.

2. Sensor Selection: The type and location of sensors is physically governed by the available hardware and structure accessibility, and has a strong influence in the quality and amount of modal test data that can be extracted. To derive optimal sensor locations under these conditions, a large number of candidate locations are evaluated using modal metrics to then run an iterative sensor elimination routine and obtain the best locations based on said constraints. The location array must ensure the best possible quality of test data and avoid spatial aliasing to distinguish between mode shapes. The modal metrics used for sensor placements include the use of normalised modal displacements, kinetic energy, mass loading sensitivities, whilst the sensor eliminations techniques are based on the effective independence method and MAC methods, depending on the characteristics of the component. In any case, of the initial list of possible candidates, iterative elimination steps remove sensor DOFs until the the allowable number of sensors is reached. With a satisfactory array of locations, these are exported with generalised coordinate and direction, as well as a model node counterpart.

3. Excitation Location: Similar to the sensor selection, the excitation placements must also be evaluated to ensure sufficient energy is imparted onto the structure and all target modes are excited. The most common method is using the aforementioned definition of MKE an focusing on the points that exhibit a large displacement for all relevant nodes [108]. MPA is also a metric that is relevant to excitation location, as it describes how energy is propagated through the structure. It can identify which modes are excited by each input location and also if all target modes are sufficiently activated by the set [107].

4. Sensor acceptance: The last stage in the pretest analysis is to evaluate the selected sensor and excitation arrangement. The main tool in this case is to perform an autoMAC evaluation of the mode shapes at the measured locations. The autoMAC is a self-intersecting modal assurance criterion (MAC) analysis on

the mode shapes at each evaluation point [105], and therefore presents a type of idealised version of the common MAC metric to compare the difference between mode shapes and avoid spatial aliasing. In this case, the main diagonal terms of the MAC matrix will, by definition (Eq. (3.51)), equate to 1 and therefore the interest is set on the off-diagonal terms. The general formulation for the MAC between two mode shape vectors Φ_i and Φ_j is defined as:

$$\text{MAC}(\{\Phi_i\},\{\Phi_j\}) = \frac{|\{\Phi_i\}^T\{\Phi_j\}|^2}{(\{\Phi_i\}^T\{\Phi_i\})(\{\Phi_j\}^T\{\Phi_j\})} \tag{3.51}$$

The sensor arrangement must provide the low correlation between different modes, i.e. off-diagonal terms should be the lowest possible.

3.3.2 Instrumentation

The available hardware for the inspection of structures consists of an impact hammer and various accelerometers, which allow for *roving hammer tests* [111]. This type of testing system is common in machining environments [53], and is capable of offering satisfactory results within a specific frequency band [112, 105]. Expansion on the strengths and limitations of this is presented in this section.

In the present research, the data acquisition suite is based on NI-9234 sound and vibration modules. CutPro software from MALinc is used for some small scale tests, and an 8-slot National Instruments cRIO-9049 chassis is used on more demanding test involving higher number of sensors. All instrumentation data can be summarised in the following table:

Impact Hammer			
Model		Kistler 9722A500	
Sensitivity		11.45 $[mV/N]$	
Accelerometers			
Type	Model	Nominal Weight [gr]	Measuring Range [g]
Uniaxial	8702B50T	8.7	±50
Uniaxial	8778A500	0.6	±500
Triaxial	8763B050BT	4.5	±50
Data Acquisition Components			
Type		Model	
IEPE Analogue Input Module		NI9234	
DAQ Chasis		cDAQ9171	
compactRIO		cRIO 9049	

Table 3.2: Excitation and Response Transducer Data

Flexible structures can oftentimes be challenging to excite using a modal hammer test. The main drawbacks of this method are potential signal-to-noise ratio issues and double impacts, which affect the spectral evaluations, particularly of output signals [105, 10]. It is therefore common to utilise a set of masses and varying stiffness tips on the impact hammers to counter these effects. Properties of these tips affect the excitation signal, where softer tips present a reduction in frequency range as the contact time is increased. The quality metrics of this test are presented in Eqs. (3.59) and (3.60).

Understanding the benefits and limitations of the impact hammer test, it is key to examine the excitation spectrum the hammer can impart on a structure for each one of these tips and have a quantified bandwidth for each. A relevant frequency band for this study is determined both by the expected frequencies of the structure, as well as by the nominal machining parameters commonly used for aluminium. Typical spindle speeds range between 12 to 18 [kRPM] with 3 and 4 flute tools that yield tooth passing frequencies between 600 and 1200 [Hz]. Inspecting the hammer with different stiffness tips, using a suspended mass, results in Figure 3.2:

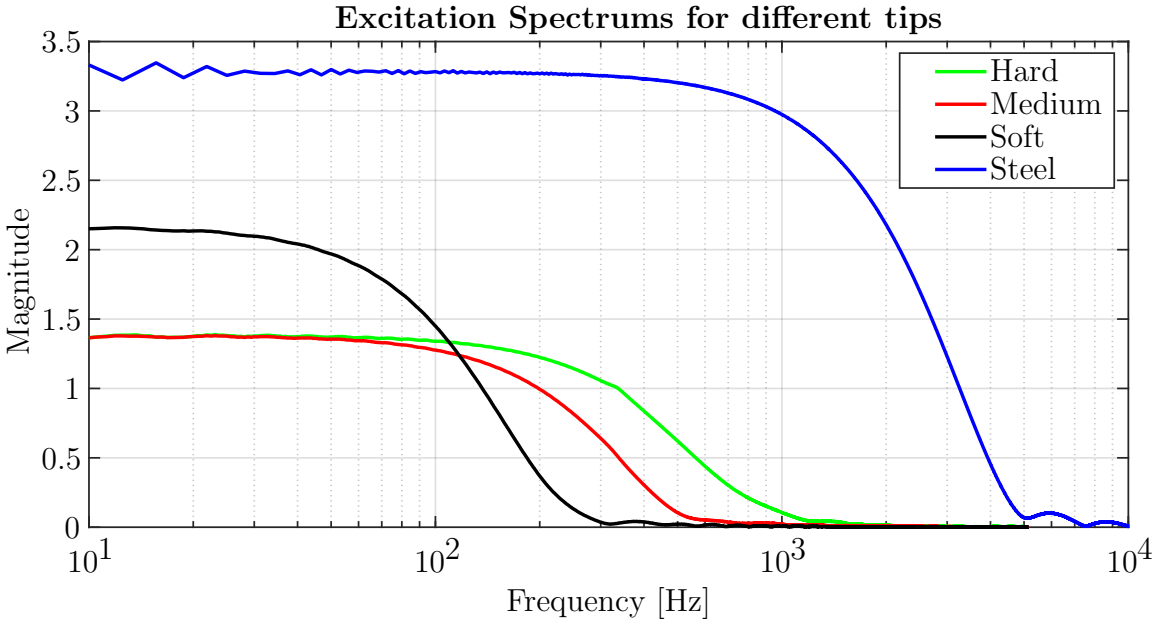

Figure 3.2: Hammer Tip Spectrum Comparison

Figure 3.2 clearly exhibits the reduction in frequency content depending on the stiffness of the tip. As expected, the stiffer the tip, the wider the range. It also confirms the requirement to employ the steel tips in all impact tests, as any softer tip would fail to input a sufficient bandwidth.

3.3.3 Experimental Data Processing

EMA testing software for machining applications usually focus on tool-tip dynamics and off-the-shelf testing kit (such as MALInc. CutPro or Metal Max) can only accommodate a limited amount of analogue signals per measurement recording. With a focus set workpiece dynamics, a larger amount of acceleration signals is preferable and therefore a broader data acquisition system is employed.The measurement system follows a similar chain, to that described in [105], and data acquisition parameters are closely selected in order to avoid common sources of error of spectral analysis and Discrete Fourier Transforms (DFT), such as aliasing or leakage.

The starting point of the acquisition parameters is using the sampling theorem (also known as the Nyquist frequency) to define the frequency spectrum range, ω_{max}, and resolution $\Delta\omega$ as a function of sampling frequency ω_s and sample length T.

$$\omega_{max} = \frac{\omega_s}{2} \tag{3.52}$$

$$\Delta\omega = \frac{2\pi}{T} \tag{3.53}$$

Equation (3.52) states that the maximum frequency that can be extracted from a signal is equal to half of the sampling frequency. This is a result of the discretisation of the continuous time history and the inability to determine high frequency signals if the sampling rate is too low. The overall term for this effect is named *aliasing* and is a well covered topic in all signal processing domains. To address this problem, a sufficiently high sampling rate is chosen taking into account the spectral range of the hammers, expected FEA frequencies for the first 10-20 modes of the structure and eventual machining tooth passing frequencies. Sampling frequencies in the range of 50kHz is sufficient to avoid any aliasing effects within the expected spectral ranges.

Another common issues that arises from the measurement, discretisation and subsequent frequency domain evaluation of a time signal, is *leakage* [105]. This effect is related to the finite nature of the sampling time and expected periodicity of the evaluated signal. Possible solutions to reduce leakage include increasing the duration of time captured, adjusting the period to an integer factor of the signal period, windowing the raw signal or zero padding the final portion of it. As most of this work involves the measurement of transient response due to hammer inspection, leakage is handled by firstly ensuring a correct tapping methodology avoiding *double hits*. By allowing the structure to have a sufficiently long sample length and allow a natural

fade and decay in the structure's vibration, the quasi periodic assumption in this type of transient excitation is met. In second place, if the spectral analysis still presents symptoms of leakage, then exponential windowing is employed as a remedial solution. Finally, if double hits and leakage are still corrupting the FRF calculation, revaluation of hammer tips and tapping process is conducted.

Once the voltage signals for excitation and response are digitally acquired, the sensitivity values for the sensors are factored in to the convert the time signal into its corresponding units. With an adequate DFT of input and output signals, a Frequency Response Function (FRF), $H(\omega)$, is calculated as the ratio between response $X(\omega)$ and excitation $F(\omega)$ DFTs [89], shown in Equation (3.54):

$$H(\omega) = \frac{X(\omega)}{F(\omega)} \tag{3.54}$$

To add robustness to the calculations of the FRFs, a series of taps are performed for each location. This allows repeatability metrics to evaluate the quality of the signal and effects of noise, by calculating the *coherence*. In this case, coherence uses the complex domain of DFT to calculate the *cross-power spectrum* between vibration and force using the complex conjugate properties. Thus, the cross-power spectrum can be defined as:

$$S_{xF}(\omega) = X(\omega) \cdot F^*(\omega) \tag{3.55}$$

$$S_{Fx}(\omega) = X^*(\omega) \cdot F(\omega) \tag{3.56}$$

$$\Leftrightarrow S_{xF}(\omega) = S^*_{Fx}(\omega)$$

In a similar manner, the auto-spectrum for force and vibration can be expressed as:

$$S_{FF}(\omega) = F(\omega) \cdot F^*(\omega) \tag{3.57}$$

$$S_{xx}(\omega) = X(\omega) \cdot X^*(\omega) \tag{3.58}$$

The expressions 3.55 and 3.56 can conveniently express Eq. (3.54), either as:

$$H_1(\omega) = \frac{S_{Fx}(\omega)}{S_{FF}(\omega)} \tag{3.59}$$

$$H_2(\omega) = \frac{S_{xx}(\omega)}{S_{xF}(\omega)} \tag{3.60}$$

These expressions would be identical if the signals were free of noise. However, it is well established that noisy data, in both input and output signals, degrades the

measured spectra and therefore both FRF estimators (H_1 and H_2) will present different values. For impact hammer tests, H_1 is better suited as the response signal usually contains higher level of noise compared to that of the force signal [10]. Coherence is then calculated as the ratio between these FRF estimates, and requires constant monitoring whilst performing impact testing. It is defined as:

$$\begin{aligned} \gamma^2 &= \frac{H_1(\omega)}{H_2(\omega)} \\ &= \frac{|S_{Fx}(\omega)|^2}{S_{FF}(\omega) \cdot S_{xx}(\omega)} \\ &\leq 1 \end{aligned} \tag{3.61}$$

Detailed analysis on the linear algebra and definitions of this *magnitude squared coherence* indicator can be found in sections 2.11 and 3.8.4 of [89], as well as in section 3.5.1 of [10].

The final step in processing the physical data is to translate the estimated FRF into universal file format *(*.uff)* so that the FEA solver can make use of the experimental data and perform model updating. To do this, an adapted version of the MATLAB `writeuff` function is employed. It requires FEA mesh association for all FRFs extracted, by specifying impact location node number, impact direction, response location node number and response direction. To automate this aspect, careful description of the physical location of the sensors is noted, then the mesh of the `inp` file is scanned against it and the closest node selected. With the associated node numbers and directions for each of the sensors, a single excitation point yields a series of direct and cross FRFs.

3.3.4 Correlation

Modal correlation analysis is used to quantify the correspondence and fit between experimental data and the FEA model. This section reviews the associated methods used to compare them. The steps required follow:

1. Importing test FRF data:
   The import of all experimental FRFs into the FEA platform is done via the aforementioned `uff` file, details of which are available in [113]. For modal analysis testing, the direct and cross FRFs are compiled into a single file under a series of #58 data set entries. The FRF data is presented with the abscissa for frequency and real/imaginary data in the ordinate.

2. Modal parameter extraction:
   The extraction of modal parameters commonly consists in curve fitting a theoretical mDOF expression (Eq. (3.28)) to match the experimental measured data FRFs. It is considered as one the most significant activities in modal analysis and multiple methods to address it have been developed. In this case, the built in solver from the FE solver is based on a *Least Squares Complex Frequency* method [114], and provides a robust global frequency domain estimator. Physical and mathematical poles of the system are distinguished using a stabilisation chart, which allow for mode shapes and residuals to be obtained. With the use of driving point FRF mass normalisation of the mode shapes is performed with the least square method provide the modal scaling. If the system is deemed to be influenced by mass loading, then a Dobson method local parameter extractor can be employed [115]. With extracted mode shapes, participation factors and residuals (both upper and lower), the FRFs can be re-synthesised using eq. 47 of [114]. Finally, a comparison between the test and these re-synthesised FRFs offers a quality check of the curve fitting method and parameter extraction.

3. Spatial and Shape Correlation:
   Spatial correlation ensures adequate matching (within a tolerance margin) between the coordinate system of both the model and the test. By calculating spatial deviations between grid locations of both sets, topological coincidence and transformation tools quantify spatial correlations. The aim of this step is to *pair* the corresponding test location point and DOF to its corresponding FE mesh node and DOF.

   With the test grid and FE mesh linked, a mode shape correlation can be performed. The numerical metric used in this case is the aforementioned (Eq. (3.51)) *Modal Assurance Criterion* (MAC) [116]. This MAC matrix compares the similarity of all combinations of extracted mode shapes in the test and model using a normalised dot (or scalar) product of the complex modal vectors at the paired points. If the value is close to 100%, both vectors describe the same type of deformation. Alternatively, a value close to 0% indicates non-matching shapes. With use of this MAC matrix, manual or automated mode shape pairs can be performed over a predefined similarity threshold.

The correlation efforts culminate in a numerical evaluation of the test data against the FE model. The different instances of correlation provide a rich set of comparison metrics that aid the modal analysis effort in two fronts. Firstly, the correlation data

is used to verify the FE model, i.e. determine whether the FEA approach is suitable enough to provide an accurate representation of the physical component. Secondly, the correlation data allows for improvement of the model via model updating procedures. Parameters within the FE definition (either direct or indirect) are corrected to produce an improved model with closer resemblance to the physical structure, eventually resulting in the derivation of a validated model.

3.4 Model Updating

The process of correcting the parameters of a numerical model using experimental data is referred to as model updating. This is an important step in structural dynamics as it allows validation of said analytical models and ensures dynamic response predictions are as accurate as possible. The field of model updating is rich with several publications and books [105, 117, 118] covering the topic. This section describes the main procedures employed to update FE models, based on [117], and how the thesis uses the validated models to drive the subsequent optimisation efforts.

Initial modelling efforts can only estimate key *parameters*, that might differ from real-world conditions and therefore result in discrepancies between predicted and measured *responses*. The main sources of uncertainty in FE modelling are grouped into three main categories:

- Modelling uncertainties arise from the geometrical representation of the component via an FE mesh. Mesh density and refinement has a significant impact in the accuracy of the model on the backhand of CPU time trade off, which is central for accurate joint modelling. Geometrical mismatches between the modelled dimensions and details of the physical structure are also grouped in this source of uncertainties. This issues becomes more relevant as the models become larger and higher number of components and joints are included.
- Physical properties uncertainties are due to errors in the definitions of element properties. For example, material constants, boundary conditions, or even non-linear effects and damping, are sources of this type of uncertainty. Mechanical joint modelling, in particular, can be a considerable source of uncertainty if dynamic models are not addressing this effect explicitly and are disregarding localised joint parameters.
- Analysis uncertainties are the result of accuracy costs within numerical simplification methods employed by the FE solver. Eigenvalue extraction, for example,

can be performed on a reduced set of degrees of freedom with a somewhat satisfactory accuracy. Nevertheless these types of uncertainties must be evaluated prior to the employment of reduction techniques. Mistakes within the implementation of the model also fall in this category and include, among others, inconsistent or wrong units and typing errors. The reduction of manual inputting of key parameters can help the reduction in this type of error.

From the previous list, only the physical property based uncertainties can be addressed successfully by model updating methods. The other sources of error are difficult to identify and cannot be automatically corrected by software. It is therefore paramount to establish a correct FEA implementation procedure prior to any automated updating or optimisation efforts.

The initial requirements for structural dynamic updating are the FE mass and stiffness matrices, the modal counterparts for natural frequency and mode shapes, as well as FEA based FRFs. Alongside these, updating also uses a limited set of responses and modal property matrices of the experimental model, usually of a smaller size than analytical ones. This last aspect implies an under-determination of the problem which represents a mathematical impasse. In order to address this issue, updating efforts will firstly define the *sensitivity* of responses to modelling parameters.

An iterative model updating method is used, based on a penalty function of the sensitivity formulation. The basic linear approximation for finite differences is given by:

$$\{\Delta R\} = [S]\{\Delta P\} \tag{3.62}$$

Where the sensitivity matrix $[S]$ contains the gradients of responses R respect to parameters P, as:

$$[S] = S_{ij} = \frac{\partial R_i}{\partial P_j} \tag{3.63}$$

In order to update the parameters on the next iteration, weighting matrices ($[W]$) are introduced to change the influence of particular responses or parameters. This is due to the fact that in most vibration tests, mode shape data is generally less reliable than natural frequency data [117], or similarly, higher frequency modes are not usually measured as accurately as lower ones (particularly with impact hammer tests). With this, the updated parameters can be expressed as:

$$\{P\} = \{P_0\} + \left([W_P] + [S]^T[W_R][S]\right)^{-1}[S]^T[W_R](\Delta R) \tag{3.64}$$

This expression is nested under the assumption that the matrix $S^T W S$ is square and full rank. Further expansion on the determination of the updated parameters can be found in equation 8.20 in chapter 8.2.3 of Friswell and Mottershead's FEA model updating book [117], and the sensitivity-based model section of [118].

Depending on how the FE model has been constructed, the available parameters to update upon may vary. In this research, much of the updating efforts go into quantifying the effects of boundary conditions, joints and multi-body assemblies on the dynamic response. The uncertainty arising from modelling coupled parts is a common driver for updating routines. In particular, the main methods used in this research evaluate different methods in boundary condition modelling via material property update, spring stiffness [101] and interface layer methods [100, 119, 104, 102]. The applicability and effectiveness of these methods are also evaluated based on global parameter approaches, as well as local parameter updating methods.

The responses used to update the model, are modal using resonant frequencies and MAC values. Correlation coefficients are based on absolute difference between simulation and response, $(\frac{|\omega_i^s - \omega_i^t|}{|\omega_i^t|})$, rather than mean values. The evolution of parameter values is tracked and evaluated using a convergence curve to ensure the iterations are updating the model adequately.

Chapter 4

Optimisation Programming

With a comprehensive understanding of analytical modal analysis, numerical modelling, and experimental methods, this chapter defines an optimisation programme centred on FEA simulations. The primary focus is on the evaluation and improvement of workholding configurations, mostly targeting double-sided access (DSA) environments. The development of a robust computational framework to analyse DSA environments is central to the project's goals, as outlined in Section 1.2. As highlighted previously (Section 2.2.1), minimally held environments can offer benefits for components where low inventory costs, manual handling and lead times requirements are critical, nevertheless these will evoke a compromise on the components' stiffness and ultimately the potential MRR it could achieve under more traditional methods. Therefore, providing these types of workholding arrangements with an optimisation protocol to maximise the overall stiffness of the component is a step forward to enabling this type of technology.

This chapter aims to introduce an original program capable of taking a set of user defined variables and autonomously conducting iterative dynamic modelling of workholding layout simulations to resolve in an optimal layout solution. For this, three main key components are required. Firstly an automated FEA scripting program is essential for generating simulations based on numerical arrays of layout candidates. This subroutine should operate in such a way that sequential executions of FEA models is performed automatically, without the need for human intervention. Secondly, a numerical optimisation method must be implemented in order to evaluate the exported data and defining the candidates for subsequent stages. Lastly, an overall software integration program is required to link the FEA simulation platform with the numerical

evaluation system. In this case, the FEA codes used are DDS FEMTOOLS and Simulia ABAQUS CAE with Mathworks MATLAB as the numerical programming environment.

The optimisation architecture is also expected to operate for a broad range of applications where this type of FEA approach is suitable. Hard-coding definitions are to be minimised throughout the code and ancillary functions are to be implemented wherever required. The benefits of this versatility in the code is to broaden the possible implementation avenues the end user can target, tailoring simulations to particular needs and restrictions that may be necessary. This removes some limitations for the optimisation to run exclusively for a particular billet size, shape, material, clamp geometries, machining stage, fitness functions, and others.

The sections in this chapter firstly present the development of the mathematical basis by which workholding layouts can be parameterised, and using this approach, formally define the search space domain. A second section uses modal analysis and machining dynamics functions to discuss and define a set of possible fitness functions the optimisation program can target to improve workholding layouts. With these definitions, the computational optimisation approach is programmed alongside the software integration code that will command the FEA software on the layouts to evaluate. Finally, before performing full scale optimisation runs, a set of pre-simulation checks are compared against exhaustive searches in order to troubleshoot and compare the performance of the optimisation architecture.

4.1 Workholding Layout Parameterisation

The first step for layout optimisation is an analytical layout definition and parametrization, which aims to quantify and evaluate the relevant variables for any arbitrary external or internal workholding layout around a perimeter. To aid the definition and visualisation of variables, Figures 4.1 and 4.2 are presented. For simplicity, the stock condition of the billet is considered rectangular of size L_1 and L_2, the number of vices in a layout is given by N. This parameterisation can then generalised to an arbitrary perimeter domain.

4.1.1 Combinatorial analysis of layouts

Not losing generality, the combinatorial analysis of the amount of possible layouts can firstly be evaluated for a single side.

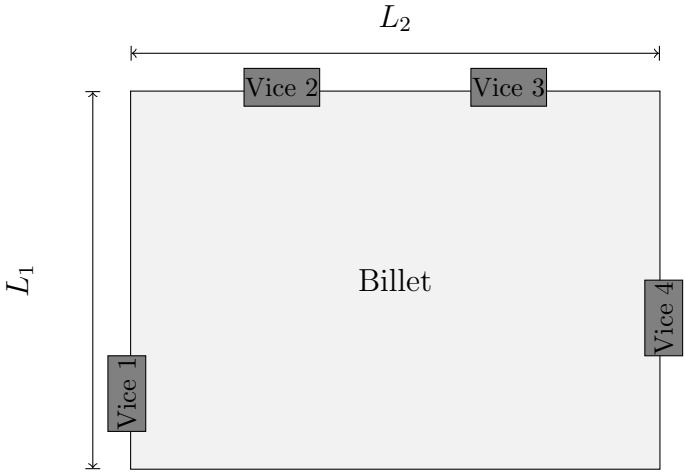

Figure 4.1: Arbitrary vice layout

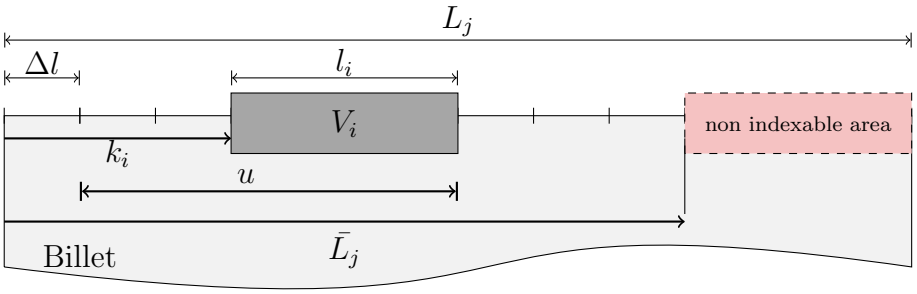

Figure 4.2: Definition of parametrization variables

Figure 4.2 shows the definition of relevant parameters for a given side j of length L_j, from here we identify the spatial resolution, Δl, length of the vice V_i is l_i, the position (or index) of the vice is k_i, which can take values within the indexable length $\bar{L}_j$. An early assumption can be made, considering all vices of the same length, therefore:

$$\bar{L}_j = L_j - l_i \tag{4.1}$$

Next, the definition of the total number of layouts as Γ_T, and the total available positions for vice V_i as P_i, is:

$$\Gamma_T = \prod_{i=1}^{N} P_i \tag{4.2}$$

The explicit formulation for the available positions for a vice, P_i requires the definition of total possible positions a vice can take P_T. For a single side j this is:

$$P_{T,j} = \left\lfloor \frac{\bar{L}_j}{\Delta l} \right\rfloor + 1 \in \mathbb{N} \tag{4.3}$$

Equation (4.3) uses a floor operator on the ratio between the indexable length of the side and the spatial resolution to calculate P_T as an integer. The addition of 1 is to account for indexing at the origin.
This definition of P_T allows the trivial definition of the available positions to place one vice $P_1 = P_T$ as a single vice can take any position. For a second and subsequent placement of vices, an explicit formulation can take the following form:

$$P_i = P_{T,j} - \sum_{i-1} u_{v,j} \tag{4.4}$$

Where the sum on u_v is the amount of unavailable space used by all previous vices on side j. The definition of u_v is dependent on the index position, k_i, of each vice, as placement near the edges disables fewer spaces than when the vice is located more than a vice length away of the edge. Formally the disabled space vice i uses is:

$$u_i = u_{i,k} = \begin{cases} \lfloor \frac{l_i}{\Delta l} \rfloor + k_i, & k_i < \frac{l_i}{\Delta l} \\ 2\lfloor \frac{l_i}{\Delta l} \rfloor - 1, & k_i \in \left[\frac{l_i}{\Delta l}, \bar{L_j} - l_i \right] \\ \lfloor \frac{l_i}{\Delta l} \rfloor + (\bar{L_j} - k_i), & k_i > \bar{L_j} - l_i \end{cases} \tag{4.5}$$

Again, Eq. (4.5) uses a floor operator to quantify u_i as an integer. The strict definition of this variable is made to highlight the fact that when the vice is less than a vice length from the edge, the disabled length is smaller. Nevertheless, when a vice is located far from the edges, the disabled space equates to twice the length of the vice, which is intuitive, as the vice itself uses one length, and adding another one requires at least half the length on either side.

With this in mind, it is assumed all vices are the same length and that the disabled space is just $u_i = u = 2\lfloor \frac{l_i}{\Delta l} \rfloor - 1$, to provide a lower bound. Evaluating this case for the total number of layouts, Γ_T in Eq. (4.2), takes the form:

$$\boxed{\Gamma_T = \prod_{i=1}^{N} \Big(P_T - u(i-1) \Big)} \tag{4.6}$$

$$= P_T \cdot (P_T - u) \cdot (P_T - 2u) \cdot \ldots$$

$$< {P_T}^N \tag{4.7}$$

To generalise this description to all four sides of the billet:

$$P_T = \sum_{j=1}^{4} P_{T,j} \tag{4.8}$$

Depending on the internal geometry of the component, lines of symmetry can further define congruent layouts and halve the layouts.

As any given layout is defined by the position of its vices (x_i), a general parametrization of an arbitrary vice, Γ_i, can be defined as a vector:

$$\Gamma_i = (x_1, x_2, ..., x_n), \quad x_i \in [0, \bar{L_T}] \tag{4.9}$$

With n being the number of vices composing layout Γ_i and $\bar{L_T}$ the total indexable perimeter length ($\sum_j \bar{L_i}$)

Sensitivity analysis

Expanding the expression of Eq. (4.6) and rearranging the terms it can be observed that:

$$\begin{aligned} \Gamma_T &= \prod_{i=1}^{N} \Big(P_T - u(i-1) \Big) \\ &= \prod_{i=1}^{N} \left(\frac{\bar{L_j} - 2l_i(i-1)}{\Delta L} + i \right) \\ \Rightarrow \Gamma_T &\propto \left(\frac{\bar{L_j}}{\Delta L} \right)^N \end{aligned} \tag{4.10}$$

Where the total number of layouts is proportional to the ratio between the perimeter and spatial resolution, and exponential to the number of vices.

Numerical Example

Consider the following numerical example: Substituting this values in Eq. (4.4) gives:

$$\begin{array}{lcl} L_1 & = & 500 \text{ mm} \\ L_2 & = & 700 \text{ mm} \\ N & = & 4 \text{ vices} \\ l_i & = & 100 \text{ mm} \\ \Delta l & = & 10 \text{ mm} \end{array}$$

$$
\begin{aligned}
P_T &= \sum_{j=1}^{4} P_{T,j} \\
P_{T,1} = P_{T,3} &= \left\lfloor \frac{\bar{L_1}}{\Delta l} \right\rfloor + 1 = \frac{500 - 100}{10} + 1 \\
&= 41 \\
P_{T,2} = P_{T,4} &= 61 \\
&\boxed{\Rightarrow P_T = 204} \\
u &= \left\lfloor \frac{2l_i}{\Delta l} \right\rfloor - 1 \\
&= 19
\end{aligned}
$$

Using Equation (4.6) and 4.7:

$$
\begin{aligned}
&\Gamma_T = 204 \cdot (204 - 19) \cdot (200 - 2 \cdot 19) \cdot (200 - 3 \cdot 19) \\
&\boxed{\Gamma_T = 9.21 \cdot 10^8} \text{ possible layouts}
\end{aligned}
$$

Now using $\Delta l = 100mm$

$$
\begin{aligned}
\Rightarrow \Gamma_T &= 24 \cdot 23 \cdot 22 \cdot 21 = 255024 \\
&= 2.55 \cdot 10^5 \text{ possible layouts}
\end{aligned}
$$

4.2 Fitness and Objective Functions

Understanding that the total number of layouts is significant and performing dynamic evaluations for each is unfeasible, a method to derive optimal layouts needs strict definition. However, the first step is to define what constitutes an optimal layout and the metrics employed to evaluate each one.

A common objective in machining is to maximise the material removal rate (MRR) for a given tool path. Focusing on milling operations, the MRR is defined as:

$$
\text{MRR} = a_p a_e f_t N_t \Omega \tag{4.11}
$$

Where a_p and a_e are the axial and radial depths of cut respectively, and f_t, N_t and Ω are the feed per tooth, number of teeth and spindle speed of the tool. As presented in Equation (2.18) the relationship between the stable limit for the axial depth of

cut, $a_{p,lim}$, is proportional to the transfer function of the system following the generic expressions [10, 120]:

$$a_{p,lim} \propto \frac{\Lambda_R}{K_t}\left(1+\left(\frac{\Lambda_I}{\Lambda_R}\right)^2\right) \tag{4.12}$$

$$\frac{f_c}{\Omega} = N + \frac{\varepsilon}{2\pi} \tag{4.13}$$

Λ_R and Λ_I is the real and imaginary valued parts of a driving point receptance in the system and K_t is the cutting force coefficient. This expression state the relationship between the system's dynamic response and the stable axial depth of cut limit. Given that a_p is a physical quantity, the negative valued part of the real transfer function is required. The inverse relationship also showcases that flexible structures will reduce the axial depth of cut and eventual productivity, as well as harder materials that exhibit a larger K_t value. Given that boundary conditions have a direct influence on the equations of motion of the system, and therefore determine the mode shapes and natural frequencies, the fitness function of the optimisation program must evaluate the real valued part of the FRF targeting optimal locations of work-holding elements to increase the stable depth of cut limit. This fitness function can then be expressed as either calculating the minimum value of direct real part FRF data, or implementing tooling parameters and directional coefficients to yield an oriented FRF (Section 2.1.1) to calculate an SLD and maximise $a_{p,crit}$.

4.2.1 Evaluation Points

Before describing each proposed fitness function in detail, a procedure to quantify the dynamic response of the modelled system is required. For a given layout, an FE model is generated to simulate the workholding arrangement and extract modal parameters and direct FRFs. Points within the workpiece extract driving point FRFs in a uniform rectangular grid, as seen in Figure 4.3. For each of these points, FRFs are computed in each of the three main directions. The figure shows an example of plotting together 3 points for a single direction. Once all FRFs are obtained, a numerical software can use them to evaluate the fitness functions and determine the best layout by comparing these values across all evaluated layouts.

4.2.2 Receptance Approach

The first fitness function aims at maximising the receptance FRF factors of the depth of cut formulation. An initial observation of Equation (4.12) can define a maximisation

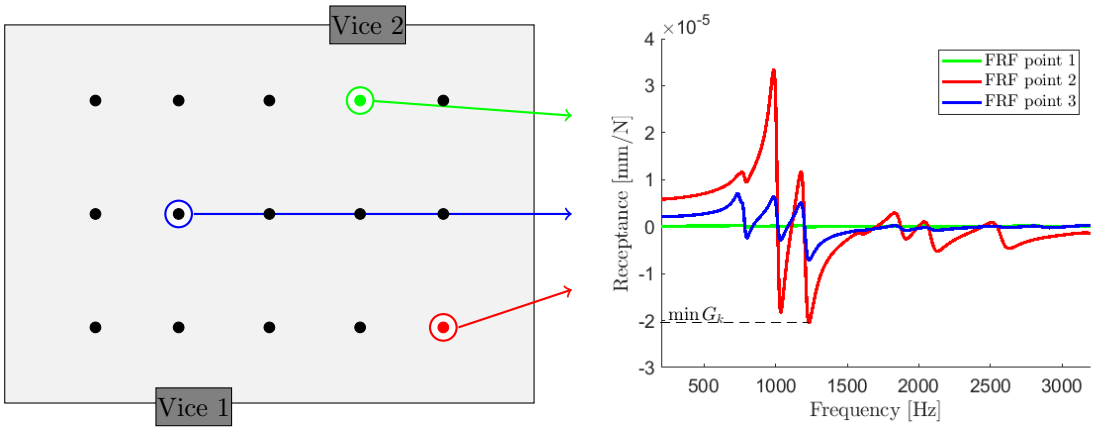

(a) Evaluation points on workpiece (b) Example FRF from 3 points in $\hat{k}$

Figure 4.3: Example of FRF extraction from (a) evaluation points and (b) real FRF plot

of the right-hand expression as a fitness function. However, this approach can be simplified even further by evaluating the negative real part of the FRFs extracting the minimum value (Fig. 4.3b). For the given set of evaluation points (k) within the workpiece a preliminary optimisation objective can then be stated as:

$$\max_{\Gamma_i} \quad \min_{k,\omega_c} G_k(\omega_c) \tag{4.14}$$

This optimisation formula evaluates an arbitrary layout (Γ_i) by selecting the minimum value of the real part FRF for a set of evaluation points on the component (G_k). By comparing this value over a set of layouts, the optimal is that which has the highest minimum real part FRF.
This approach is independent of tooling and cutting parameters, as it bases all calculations strictly on the dynamic response of the workpiece.

4.2.3 Depth of Cut Approach

This fitness function performs an additional operation on the extracted FRFs to associate generic tooling parameters and cutting conditions ($\dot{\phi}_{tool}, a_e$) in order to derive $a_{p,crit}$ values for every evaluated point. The directional effect approach used in this case is that of a zeroeth order Fourier series approach (ZOA), described in Section 2.1.1 for its time invariance convenience, noting its low immersion limitations. Once the FRFs are imported, calculations for the eigenvalues of the characteristic equations are performed and values for $a_{p,lim}$ are computed as functions of the chatter frequency. The minimum value is associated to the $a_{p,crit}$. The objective function can then be

stated as:

$$\max_{\Gamma_i} \quad \min_{k,\omega_c} \quad a_{p,lim}(\omega_c) \tag{4.15}$$

Which translates into finding layout Γ_i that has the highest $a_{p,crit}$.
The $a_{p,crit}$ is preferred, over a simple maximum of a_{lim} (making use of the lobing effect), given the fact that the inspection grid set to evaluate each layout has been purposefully designed to avoid any nodal effects of the mode shapes. This metric also provides a reduction in computational costs which benefits the overall convergence time of the optimisation program. Expansion on to more powerful computing platforms capable of increased numerical optimisation demands, should be justified based on the results of simpler cases with lower complexity and processing requirements. If proven successful in said cases, the use of high performance computing platforms for optimisation focusing on maximising a_{lim} within each lobe can ensue. Alongside this, higher complexity models can als be evaluated, including multi-frequency estimations and introducing helix angles and 3D stability models.

4.3 Optimisation Algorithm

In this instance a *particle swarm optimisation* (PSO) approach is chosen given it is a well documented metaheuristic [121] that has been successfully used to evaluate static displacements of workpieces, but not dynamic stability [122, 78]. As covered in the literature review section (Section 2.2), particle swarm approaches have been identified as a useful numerical optimisation approach, and have reportedly time and accuracy benefits when compared to genetic algorithm methods [78]. Alongside this, PSO also offers a broad range of adjustable parameters to tailor the behaviour of the optimisation program for user-specific needs. Other optimisation approaches considered can surely provide a different set of benefits and limitations, however, the reported suitability for this type of problem, a wide programming flexibility and ample documentation available, make PSO optimisation algorithms a justifiable approach to employ in this research.

The PSO method considers a selection of layout particles that are randomly generated within the search space. Secondarily, a velocity vector is associated to each layout seed to define the direction in which subsequent generations are set to travel. These vectors can be defined as:

$$\begin{aligned} \Gamma_i &= (x_{i1}, x_{i2}, ..., x_{in}) \quad x_{ij} \in [0, \bar{L_T}] \\ \dot{\Gamma}_i &= (v_{i1}, v_{i2}, ..., v_{in}) \quad v_{ij} \in [-V_{max}, V_{max}] \end{aligned} \tag{4.16}$$

For every generation the objective function must be evaluated for each particle, which requires an FE model to to export the FRFs and modal parameters; this query is done via scripting and command programming to export data. After evaluating the results from the FE software, the four parameters from the PSO approach are stored. These parameters are:

- P_i is the vector array containing the best position for each particle for all generations.
- P_{best} is the value of the fitness function for each position of P_i.
- P_g is the single overall best particle position for the entire swarm. $P_g \in P_i$
- g_{best} is the single overall best fitness function value for the entire swarm. $g_{best} \in P_{best}$

The first two PSO parameters (P_i and P_{best}) are defined for each particle of the swarm. As the generations progress, these arrays are evaluated and updated to compare the evolution any individual particle has had. The next two PSO parameters are defined for the entirety of the swarm, defining the best overall position (P_g) and best overall fitness function value (g_{best}). Once these parameters have been stored for a given generation, the particles new position is updated following the expressions:

$$\begin{aligned} \dot{\Gamma}_i(t+1) &= \dot{\Gamma}_i(t) + C_1 r_1 (P_i - \Gamma_i(t)) + C_2 r_2 (P_g - \Gamma_i(t)) \\ \Gamma_i(t+1) &= \Gamma_i(t) + \dot{\Gamma}_i(t+1) \end{aligned} \tag{4.17}$$

The speed of the particle contains three main terms: the first is the "*inertia or momentum*" as the tendency to travel in the same initial direction. The second, "*memory or nostalgia*", attracts the particle to its own best experience. And the third term, the"*cooperation or shared information*", attracts the particle towards the best global experience of all particles. The constants C_1 and C_2 are positive weighting factors for the randomised coefficients r_1 and r_2 which are uniformly distributed in the $[0, 1]$ interval. The implementation procedure is detailed in [121]; this article also surveys studies that have evaluated the performance of a PSO using linear and non-linear rules to dynamically change the weighting of the inertia. Upon inspection of results and performance of the search algorithm, weighting of the inertia component can be explored.

4.3.1 Software Integration

As mentioned previously, one main component in the optimisation architecture is a software integration program which scripts automation for the link between the FEA platform and the numerical evaluation that updates the PSO parameters. This main compiling algorithm is generated in MATLAB, and the workflow of which is depicted in Figure 4.4. All simulations are performed on a DELL workstation (Intel Xeon 3.0GHz CPU, 16GB RAM).

4.3.2 Pre-Processing

User defined variables initialise the optimisation program by determining the physical constraints on the number (N) and length of vices (l_i), the billet's size and spatial resolution, material properties and edge availability, as well as the swarm parameters (number of particles $i \in [1, S]$, and iterations $t \in [1, T]$), FRF frequency range and resolution, and the preferred damping model (proportional viscous, or modal damping values). File specific identifiers such as directory and simulation name are also required to create the folders and files for the optimisation.

With the user inputs defined, MATLAB will first read the native mesh **.inp* file and store all node and element information. A node set is defined for the FRF evaluation points and the swarm arrays for the first step are created. Checking the minimum and maximum values of node positions against the user input billet size prompts a safeguarding error if a mismatch in coordinate system or dimensions exists.

Layouts are defined in two analogous manners: a linear version lists the vices' position along the perimeter of the billet, as per definition 4.9, resulting in a $\{1 \times n\}$ vector. The second version is a $\{n \times 2\}$ array denoting the $[X, Y]$ positions for each vice. Functions have been developed to convert from the linear to the array form and vice-versa. The purpose of this is to aid the automated reporting and graphic visualisation of results as well as node selection. With these definitions, all particles of the swarm are generated alongside their respective velocity vector according to the definition in 4.17. For each layout particle, MATLAB must then identify all nodes within a vice half-length distance from the position (in each direction equates to a full vice length) and write **.cmd* files defining the node sets for each layout. The final result in the pre-processing stage is a first generation group of *cmd* files for each particle to be executed on the FEA platform.

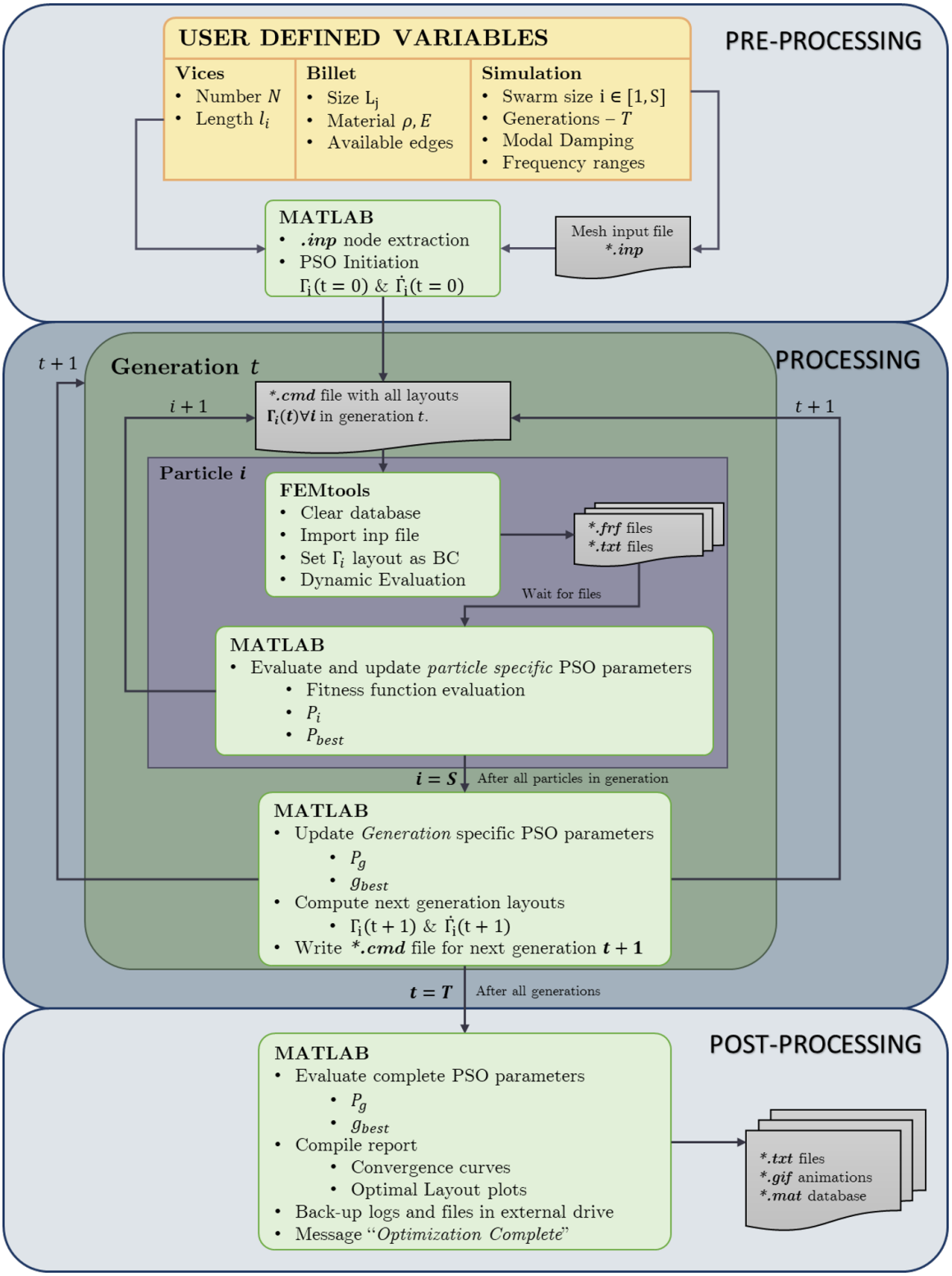

Figure 4.4: Flowchart of the optimisation algorithm process

4.3.3 Processing

Once the first generation files are generated, a consecutive evaluation of each layout begins. A subroutine function is scripted in such a way that for each particle file, all FE databases are cleared, then imports of the FE *inp* file, read the node set definition for that specific particle layout. After this, the set is defined as a boundary condition (or coupling interface, depending on the application and joint method), and prompts the FEA platform for a dynamic evaluation of the system. Once computed, x, y and z direction FRFs are defined and extracted based the aforementioned grid and exported to a user defined folder. The function also requests a *txt* file export with the natural frequencies. It then moves immediately onto the next particle and will repeat the process described above. MATLAB is constantly monitoring the existence of these files. As soon as the last particle is found, a secondary function must import each particle's set of FRFs, evaluate the fitness function update the particle specific parameters P_i and P_{best}. Once all particles are evaluated, swarm specific parameters P_g and g_{best} are stored and used to calculate the new positions and velocities for the next generation. Again, the MATLAB script uses the new layout positions and the node data to find the new node sets for each particle and write the generation's *cmd* file for FEMTOOLS to evaluate and repeat the process. This sequence of evaluating the dynamic response and exporting FRFs, whilst MATLAB reads the files and updates the swarm continues until all generations are computed.

4.3.4 Post-Processing

The last stage in the algorithm is executed by a function that compiles all the generated data and performs an evaluation of the whole swarm evolution. The final value of P_g is presumed as the optimal layout. An automated report is generated by plotting the convergence curve of the swarm, which corresponds to the values of g_{best} at each generation. The report also includes a graphical depiction of the optimal layout. An automated backup of all FRF and swarm layout files is stored in a local folder, as well as a secondary backup on an external hard drive. The program has also been scripted with the capability to extend the evaluation if the convergence curve has not settled smoothly into its maximum value and further generations are required. This has been programmed to only take place after a manual inspection of the results. Hard-coding extensions or even premature terminations of the optimisation routine depending on the behaviour of the convergence curve can be implemented quickly if required.

4.4 Pre-simulation Check

Before venturing into running long simulations, a series of checks are performed on the optimisation algorithm to ensure the system is fit for purpose. This task compares the PSO method to exhaustive searches on simplified problems, namely vice number simplifications for both single and double vice layouts; computed using full factorial arrangements. The aim is to gauge initial performance characteristics of the optimisation solver against a combinatorial mapping of the solution space. These tests do not require explicit joint characterisation in order to explore the behaviour of the optimisation program, and therefore damping characteristics of each model are assumed to be representative of lightly damped metallic structures and is set at 1%. As long as modelling setups between both approaches are consistent, having a known map of the solution space allows to determine whether the optimisation converges onto the correct position.

4.4.1 Single Vice Search

This is a fairly trivial scenario where a single vice has to be placed along the perimeter of the billet. The exhaustive search is performed on 2mm increments, and yields a plot showing the fitness scalar value as a function of the vice position. Figure 4.5a shows that the maximum fitness value is obtained at the centre of either side #2 or side #4. The positioning of the vice has been projected onto a linear domain linking all sides together, and joining all "indexable" vice position (Eq. (4.1)), where the red dotted lines indicate a change from one edge onto the next. This domain can be thought of as the perimeter of the workpiece starting from the top left corner, and therefore care must be taken when interpreting these results.

The irregular smoothness of the curve can be associated to the spatial resolution of the simulations and the interaction with the evaluation grid exporting the fitness function from fixed points. Contrasting this search result to a PSO routine based on the same conditions, the optimal layout results and convergence curve are presented in Figure 4.5c. In this case, the swarm reached the optimal layout at the third generation and shares the same result as the exhaustive search, providing initial reassurance in the PSO system.

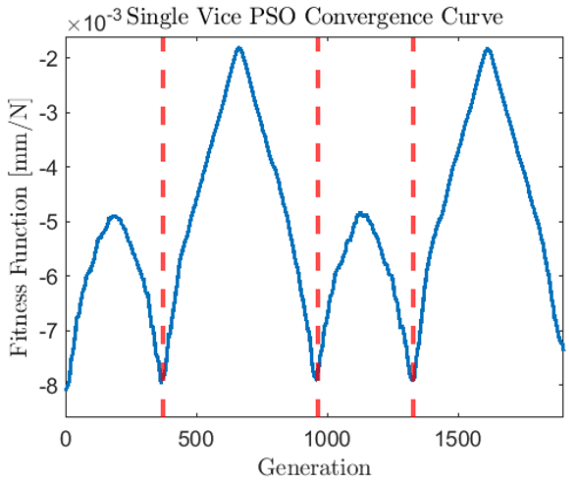

(a) Single vice exhaustive search

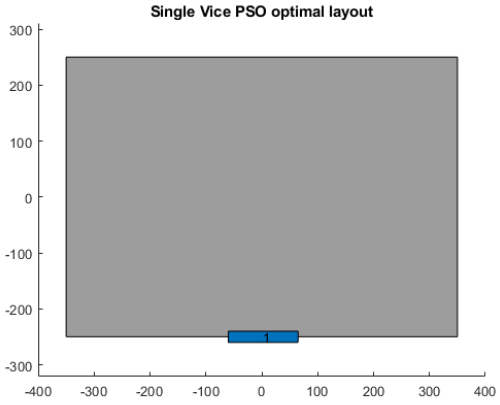

(b) Single Vice PSO optimal layout

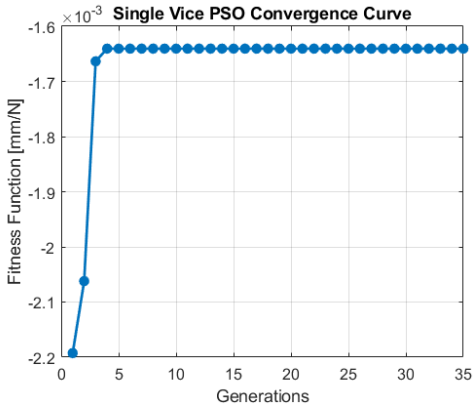

(c) Single Vice PSO Convergence Curve

Figure 4.5: Single Vice PSO results

4.4.2 Dual Vice Search

In this case, all combinations of two vice placements are evaluated using a full-factorial design. As per the combinatorial analysis of Equation (4.10) the total amount of layouts is inversely proportional to the spatial resolution, therefore to avoid running into a unmanageable simulation, the spatial resolution is set at 50mm intervals. For this case the superposition of vices is going to be allowed in order to avoid gaps in data of a surface plot. This case results in a search space of $39^2 = 1521$ combinations. After running all these simulations and obtaining their FRFs, the fitness function is plotted as a surface graph, with the indexable vice positions in the XY plane and the resulting fitness in Z, as per Figure 4.6a. This graph is accompanied by its contour plot shown in Figure 4.6b.

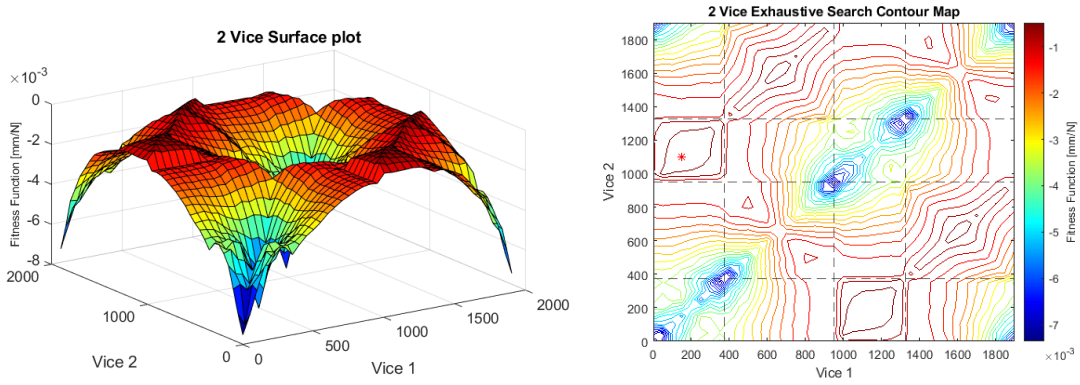

(a) Exhaustive search surface plot (b) Contour plot

Figure 4.6: Dual Vice Exhaustive search results

Due to the symmetry of the system, the upper diagonal section is identical to the lower diagonal. The diagonal itself, corresponds to the single vice placement of Section 4.4.1 (Fig. 4.5a). The results at this stage, propose a maximum at coordinates of (150,1100) which has been highlighted in Figure 4.6b with $*$.

Once observed that the maximum was located in the quadrant where each vice is located at opposite short sides of the billet, a subsequent search was performed for this area alone, but at a finer spatial resolution of 10mm. This allows to hone into the interested area and search for a more accurate optimal layout. The results show that the optimal layout in this case corresponds to coordinates (130,1080), which is the close to the one obtained in the coarser full space evaluation. Interestingly, this finer resolution effort, has highlighted the interesting behaviour along the main diagonal, Figures 4.7a and 4.7b, the maximum has also been highlighted with $*$. Remembering the definition for the indexable length, and its interpretation as a perimeter linear domain, the trajectory along the diagonal corresponds to vices starting at opposite corners (top-left and bottom-right) and moving towards the centre and back again. Plotting this diagonal against a vice, shows in better detail the behaviour of the fitness function around placing both vices at the centre. As seen in Figure 4.7c, the fitness functions presents a dip at the centre point of the billet (dotted line), which indicates that placing both vices at the centre of the edge does not necessarily equate to the best placement possible (under this particular evaluation method and fitness function). Therefore, the last step to present the optimal result derived from this exhaustive search inspection, which can be visualised in Figure 4.7d, displaying the slightly off-centred vices.

(a) Short Sides Search Surface plot

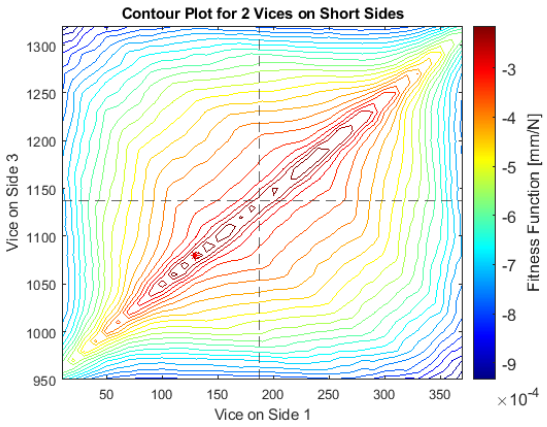

(b) Short Sides Contour plot

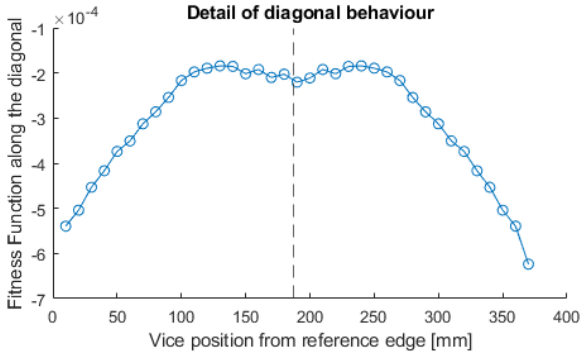

(c) Diagonal plot for 2 vice refined search

(d) Exhaustive search optimal layout

Figure 4.7: Dual Vice Exhaustive search results

Having inspected this dual vice layout definition, a PSO routine was launched to evaluate the effectiveness of the optimization system. In this case, the PSO was defined with 30 particles and 50 generations. The optimal layout derived from the PSO was at coordinates (121.9 , 1077.4) and presented a marginally higher fitness function value than those obtained in either exhaustive search. The overall difference between the high resolution and PSO optimal are 8.1mm in vice #1 and 2.5mm in vice #2, which are under the spatial increments of the exhaustive search, and therefore this exact point was not scoped initially. Another interesting observation is that this PSO optimal does not lie exactly within the diagonal previously discussed, meaning that the vices are not placed at the same distances from the edges. In this case, vice #1 is placed around 5mm further towards the centre than vice #2, and therefore not contained within the strict definition of the main diagonal of Fig. 4.6a. A possible explanation of this result lies in the potential coupling effect repeated symmetrical modes has on the FRFs. By offsetting the vices from the main centreline symmetric mode frequencies drift apart and isolate the FRF locally, improving the

fitness function values. The convergence curve for this PSO can be seen in Figure 4.8a while the layout definition of the PSO is plotted over the optimal of the exhaustive search for comparison in Figure 4.8b. The resemblance of both layouts is evident and the fact that the PSO actually derived a slightly better fitness function value is a good indication that the PSO system is working in a reliable manner

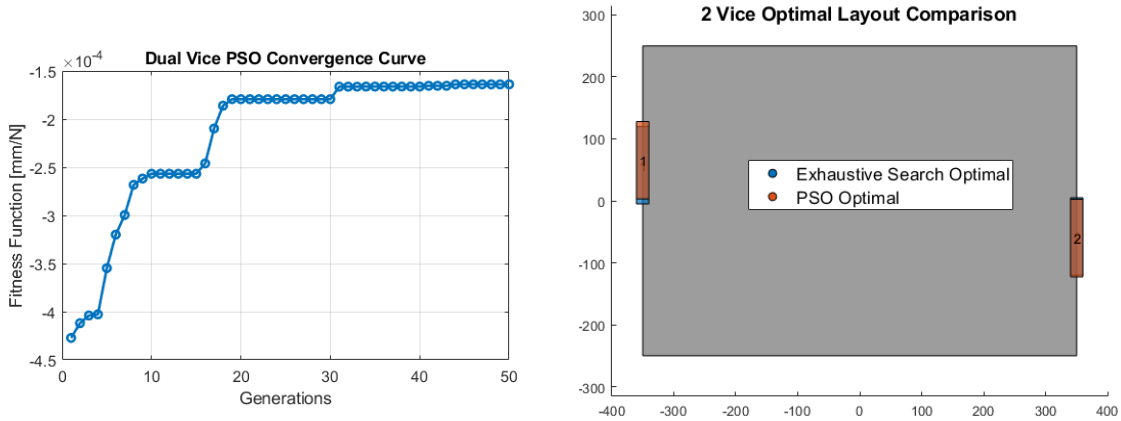

(a) Dual vice PSO convergence curve

(b) PSO optimal layout plotted over the exhaustive search optimal

Figure 4.8: Dual Vice PSO results

The application of this optimisation system will be showcased in Chapter 6 and Chapter 7. Each of these will target a different application of the optimisation program. Chapter 6 presents cases targeting external workholding, complementing this evaluation by looking at the influence of different user defined variables, swarm sizes and fitness function definitions. Chapter 7 focuses on semi-finished machining and targets the optimisation of breakaway tabs.

The upcoming Chapter 5 will focus exclusively on model updating routines based on EMA data, in order to run the optimisation program on updated and validated model parameters.

4.5 Summary

This chapter presents an original optimisation architecture programmed to use FEA based simulations in order to derive optimal workholding configurations under a set of dynamic fitness functions. It firstly determines the layout parameterisation and geometrical discretisation of the search space. This step is a cornerstone as it allows spatial discretisation and indexation of layouts within the search space.A PSO

heuristic method is used to evaluate FEA model particles within the search space and iteratively search for optimal solutions. These areas are linked together in the software integration section, which describes the algorithm that combines the numerical evaluation environments and allows for automation of the optimisation routines. The optimisation program is described in three stages: The pre-processing of initialisation parameters and user defined variables, followed by the processing stage of the swarm and its iterative generation loops, and ending in the post-processing routine where data is compiled and evaluated for the entirety of the optimisation run. The final part of this chapter offers a troubleshooting and debugging stage. The optimisation routine is checked against exhaustive search results that comb the solution space using a full factorial grid. This allows to evaluate the behaviour of the system against a known solution and confirm its capability. The setup used for these pre-simulation checks is similar to that explored in Chapter 6 and optimising for external workholding layouts.

Chapter 5

Model Updating of a Single Pocket Coupon

This Chapter investigates how different FEA modelling and updating approaches behave for dynamic analysis of a single pocket aluminium coupon. It constitutes the first instance of model updating in this project and serves as a training ground to tune the practical aspects surrounding model updating and validation of FE simulations. In this sense, it aims to develop the appropriate tools required to produce reliable and validated FEA model of the component. To do so, a sequential approach is established by initially analysing the free-free condition of the component and updating it based exclusively on material properties. Then, a bolted joint on the base of the component is modelled using different FEA approaches. Each of these methods are evaluated and updated upon using experimental data, which allows for a direct comparison on the effectiveness each approach has to model the interface dynamic behaviour. An overall improvement of a non-validated baseline model was achieved by reducing the average frequency estimation error from 4.8% to 1.5%, whilst the maximum individual error was improved from 14.6% down to 3.3%. These improvements affirm the benefits model updating has on the predictive capabilities of FEA models.

5.1 Background and Evaluated Setups

The main motivation behind this chapter is based on the need to provide highly accurate FEA models of workpiece dynamics. In this regard, model updating is deemed as a necessary step to reduce the error gap between nominal (and non-validated) models and the real physical component. Given that this project aims to enhance machining stability, modal parameter estimations (natural frequency, mode shapes

and damping) must be as close as possible to the physical responses measured on the part. This is a central activity for the optimisation program to derive trustworthy solutions. A key objective in this project is to evaluate and quantify the improvements model updating has in the predictive capabilities of FEA models, and in order to target this, thorough inspection of the experimental methods is required as well. This Chapter scopes and determines the required procedures to attain these objectives.

Complementing this research target, the component and setup studied originates from an internal GKN project which studied the evolution of workpiece dynamic response during the finishing operation of a thin walled single-pocket component. This work made use of a non-validated FE model which sequentially exported direct and cross FRFs throughout the tool path trajectory using an adaptive mesh sub-routine which replicated the material removal. Valuable insights were derived from this work, however when the FEA data is compared to experimental FRFs obtained from a physical coupon, a considerable mismatch was observed in the frequency predictions. This highlights the need to improve dynamic modelling capabilities and validation methods, in particular, by addressing the uncertainties and errors arising from joints. The applicability of the different methods for joints and boundary condition characterisation investigated in this chapter, and the results are used in subsequent applications of the optimisation architecture.

The physical component studied consists of a finished single pocket coupon of Al-7050 depicted in Figure 5.1. Overall dimensions are 245x100x42mm with a central pocket of 175x96x39mm, resulting in 2mm thick walls and a 3mm floor. The coupon has been defined as a simplified geometry that encompasses some of the challenges of a full-scale monolithic element in terms of thin wall, floor and web machining operations.

The evaluation of the component and the FEA updating methods is done in two stages; firstly evaluating a free-free condition, and in a second stage whilst bolted onto a test table.

5.2 Free-free Vibration Analysis

The first modelling and updating study corresponds to a free-free vibration analysis of the component. This initial stage aims at evaluating the capability of two different modelling platforms (Femtools and Abaqus), troubleshooting procedural aspects

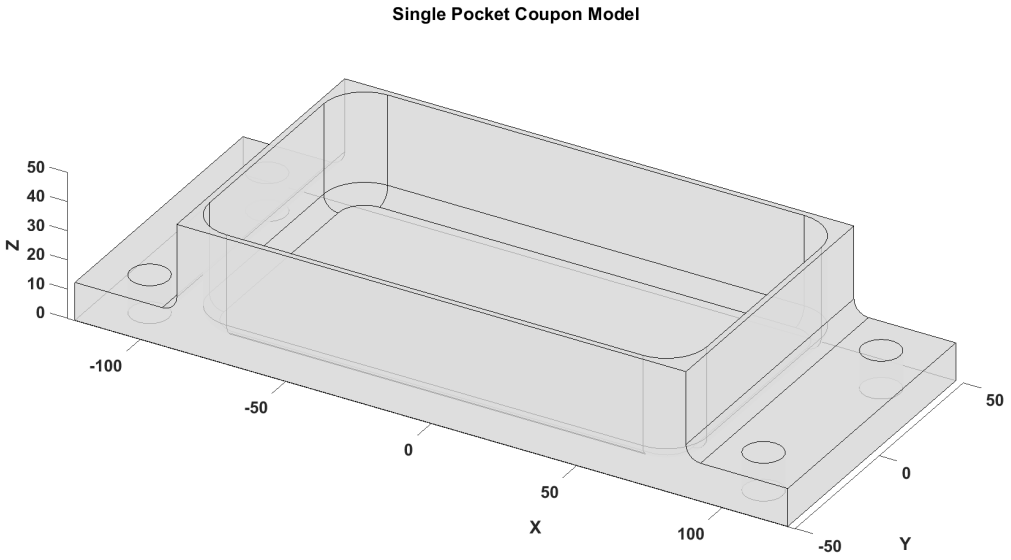

Figure 5.1: Single pocket coupon model, dimensions in mm

in EMA activities, develop the framework and scripting required to import experimental data onto the FEA platform, and finally, updating the model on the material parameters of the component and use these results on the bolted condition.

5.2.1 Free-free Baseline Model

The specific details for the free-free condition are presented for the baseline model and its fixture arrangement (or lack thereof). The dynamic solver is set on both FEA platforms to extract the first five vibration modes within a frequency range of [100-5000Hz]. The lower bound is set to avoid rigid body modes that can arise from free-free modelling. The higher is above the expected tooth pass frequencies observed in current high speed milling operations. The parameters for modelling the coupon and the results for the first five vibration modes are as shown in Table 5.1.

Visual and numeric comparison of both frequencies and mode shapes confirm that the platforms are presenting analogous results, with the slight numerical differences (all under 0.1%) attributed to the inherent differences in numerical approximations processed by both solvers. The main difference between these two platforms was observed in the computational and setup times required to evaluate the models. Initialisation of both software with a meshed component, ABAQUS took close to 38 seconds to setup, run and export the results, whereas FEMTOOLS compiled the model in just 15 seconds, yielding a considerable benefit in processing time of this model.

Free-Free Modelling Parameters			
Mesh	49159 TET4 elements		
Density	2830 $[kg/m^3]$		
Elastic Modulus	68.947 [GPa]		
Poisson's Ratio	0.33		
Baseline FEA Results			
	ABAQUS	FEMTOOLS	
Mode	Frequency [Hz]	Frequency [Hz]	Δ[%]
1	483.5	483.3	0.03%
2	1008.0	1007.5	0.05%
3	1302.0	1301.0	0.08%
4	1599.3	1598.4	0.05%
5	1869.3	1868.1	0.07%

Table 5.1: Free-free modelling parameters and results

5.2.2 Free-Free EMA

With the baseline FEA results in place, an EMA trial was performed on the component. In order to replicate the free-free condition, the coupon was suspended on elastic bungees of low stiffness as seen in Figure 5.2. The rigid body oscillations due to the suspension were checked to be at least ten times under the first vibration frequency (∼50Hz) expected from the FEA model.

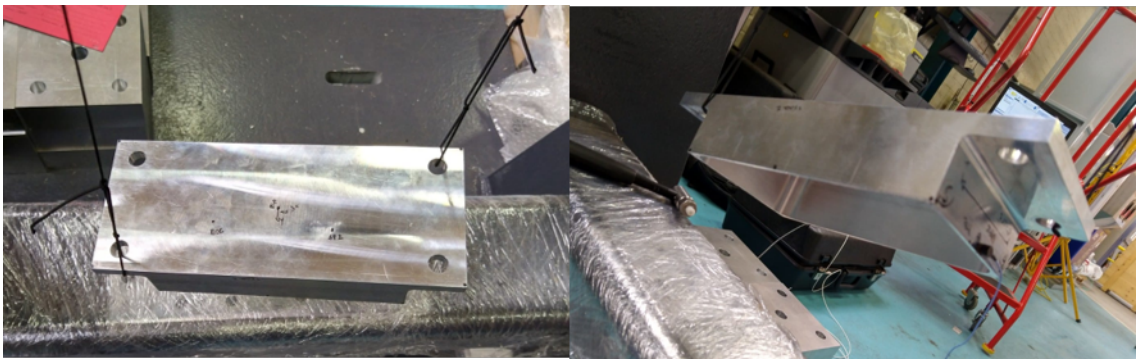

Figure 5.2: Experimental setup for free-free EMA

Pretest analysis yields a significant sensitivity to mass loading, and therefore the EMA trial ran as a roving hammer impact test on the coupon. Using normalised modal displacements metrics and mass loading sensitivities a set of 6 sensor placements and 22 excitation positions equate to an EMA trial of 132 tests.

Each impact test is ran under the impact testing unit of CutPro and exported into FRF format (real/imaginary). All resulting FRFs are then translated into UFF and

imported into FEMTOOLS for correlation and model updating activities. The correlation between modelled and experimental results is described in Section 3.3.4. It follows: point pairing, DOF pairing, modal parameter extraction and mode shape pairing.

The initial extraction on the free-free component yields the first five modes at frequencies 518, 1015, 1326, 1646 and 1899 [Hz]. Magnitude plots on all experimental FRFs is seen in Figure 5.3.

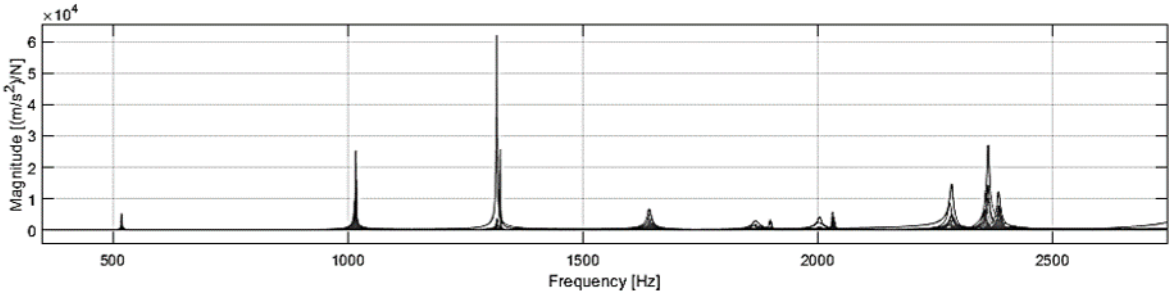

Figure 5.3: Free-free magnitude FRF plot of all 132 tests

5.2.3 Free-free Model Updating

The first step for updating of this model is a sensitivity analysis of the responses to the modelling parameters. The free-free condition limits the available parameters to global material properties, particularly density (ρ), elastic modulus (E) and Poisson's ratio (ν). The responses in this case are the first five mode frequencies and the five diagonal terms of the MAC matrix.

Figure 5.4 shows the sensitivity of these three parameters to the 10 responses (five natural frequencies and five MAC diagonal coefficients). There is an evident dominance of density and elastic modulus over Poisson's ratio for the frequencies, and relatively low sensitivity on MAC coefficients. The sign of the sensitivity relates to whether the parameters is affecting the mass (positive) or the stiffness (negative) of the system. Given that frequency is directly dependant on the ratio of stiffness to mass (Eq. (3.13)), the parameters ρ and E are expected to contribute equal proportions to variations in response. The updating iterations are then taken over ρ and E as parameters and the mode frequencies as responses.

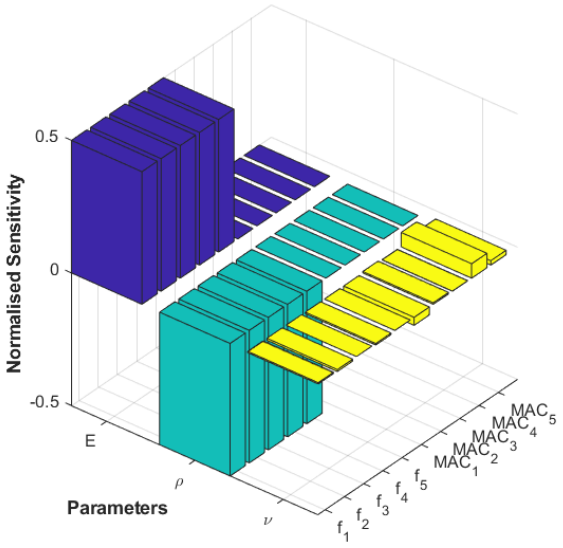

Figure 5.4: Free-free sensitivity analysis of density, elastic modulus and Poisson's ratio on frequency and MAC coefficients.

After running the updating module over these parameters and responses, a summary of the results can be seen in Table 5.2.

	Parameter	Old Value	New Value	$\Delta\%$
	E	68.947 [GPa]	70.935 [GPa]	2.88%
	ρ	2830 [Kg/m^3]	2751 [Kg/m^3]	-2.79%
Mode	$\omega_{n,EMA}$	$\omega^{old}_{n,FEA}$	Δ %	$\omega^{new}_{n,FEA}$	Δ %
1	518.5	483.34	-6.78%	497.5	-4.05%
2	1015.5	1007.5	-0.79%	1037.0	2.11%
3	1326.0	1301.0	-1.75%	1339.1	0.99%
4	1646.2	1598.4	-2.90%	1645.2	-0.06%
5	1899.2	1868.1	0.03%	1922.8	1.24%

Table 5.2: Free-free EMA results and summary of model updating, frequencies ω_n are expressed in Hz

The first set of observations is that both parameters have been updated to values within acceptable ranges for the alloy, and therefore are deemed as physically valid results. With these changes, the frequency difference between model and EMA results have changed from an average of 2.6% to 0.4%, with mode #1 have the most noticeable variation from around 7% to 4%. A secondary observation is that the initial model appeared to mostly underestimate the frequencies, while the updated version has

a mixture of slight over and underestimations for these responses. Finally, having reached individual estimations under 5% and overall mean of 0.4%, these parameters are taken forward to evaluate and model the dynamic response of the coupon bolted to a testing table.

5.3 Bolted Coupon

After the updating in free-free conditions, the same coupon was bolted onto a testing table. This table is a ground cast iron inspection plate, with pre-drilled and tapped holes to accommodate the bolting configuration of the coupon. The bolted component was then placed on a box filled with air filled protective packaging material to serve as an alternative to free-free suspension in order to isolate the coupon and table assembly from further interactions with a solid surface and focus solely on the coupon vibration modes (Fig. 5.10).

5.3.1 Bolted Coupon Modelling

This setup differs from the free-free condition given the presence of a joint fastener between the component and the base table. In order to predict the dynamic response of this new assembly, three different models are evaluated. The difference between each model is the definition of boundary conditions and fixed nodes on the mesh. Figure 5.5 shows the selected nodes for each model, where the first model only fixes the translation and rotation of the nodes in the bottom edge of the bolt holes of the coupon. The second has fixed nodes for the complete flange that house the bolts, while the third model fixes the whole bottom face of the coupon.

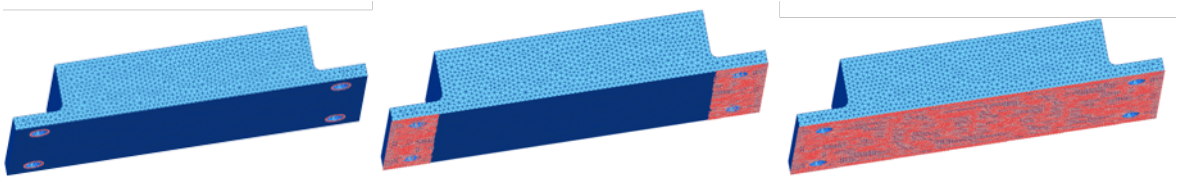

Figure 5.5: Boundary condition node definition

The first step is to compare each model's result for frequency estimation for the first ten modes, summarised in Table 5.3.

Initial inspection and comparison of the results of these models show some degree of similarity between models #1 and #2, given the un-restrained nodes of the bottom

Mode #	Model 1 *Bolt edges* [Hz]	Model 2 *Fixed Flanges* [Hz]	Model 3 *Full bottom* [Hz]
1	999.23	1013.31	1519.75
2	1269.47	1281.09	1520.42
3	1606.71	1700.82	2197.96
4	1917.69	1935.53	2204.70
5	2016.58	2033.84	2847.65
6	2403.13	2567.08	2889.12
7	2510.68	2797.09	3269.27
8	2638.50	2875.63	3332.57
9	2829.64	3076.67	4555.84
10	3133.31	3153.97	4712.14

Table 5.3: FEA mode frequency estimation for the three models for the bolted joint.

of the coupon. This condition generates modes dominated by base (pocket floor) displacement, which requires attention when associating the model to the physical component.

5.3.2 Bolted Coupon EMA

The EMA tests in this case were defined in a slightly different manner than that of the free-free condition. The main difference was the inspection and analysis of FEA modal parameters for the location and direction of the sensors and excitations.

Excitation Layout Analysis

Excitation locations and directions were evaluated using modal participation analysis (MPA). Using normalised modal displacements a proposal of excitation locations is created and this configuration is compared in all models using the MPA as a metric. Iterations over these locations were made in order to obtain a balanced and even distribution of modal excitation for the same layout, for all three different models. The resulting layout is conformed by 49 points distributed around the component, although some of these placements have to be shifted to accommodate feasible testing, for example if the bolt head is in the way or placements in the bottom face are projected onto the floor of the pocket. Table 5.4 and Figure 5.6 summarises the mode participation analysis for the same sensor layout in all three models.

The aim of this analysis is to provide an even distribution of modal participation for at least the first ten modes in all models. As seen Figure 5.6, most modes have a modal participation within 8% and 12%, with some outliers such as mode #7 for model #1,

	Model 1 *Bolt edges*		**Model 2** *Fixed Flanges*		**Model 3** *Full Bottom*		
Mode	Freq. [Hz]	MPA	Freq. [Hz]	MPA	Freq. [Hz]	MPA	Average MPA for all models
1	999.23	8.32%	1013.31	8.31%	1519.75	9.79%	8.81%
2	1269.47	13.11%	1281.09	12.48%	1520.42	9.79%	11.80%
3	1606.71	8.35%	1700.82	8.07%	2197.96	10.08%	8.83%
4	1917.69	10.93%	1935.53	10.87%	2204.7	10.07%	10.62%
5	2016.58	13.73%	2033.84	13.07%	2847.65	10.13%	12.31%
6	2403.13	5.92%	2567.08	5.02%	2889.12	10.10%	7.01%
7	2510.68	2.04%	2797.09	13.76%	3269.27	9.48%	8.43%
8	2638.5	11.94%	2875.63	13.84%	3332.57	9.35%	11.71%
9	2829.64	13.42%	3076.67	4.85%	4555.84	10.90%	9.72%
10	3133.31	12.24%	3153.97	9.73%	4712.14	10.32%	10.76%

Table 5.4: Mode participation analysis for the proposed excitation location layout

which has a comparatively low 2.04%. Nevertheless, this impact test layout is deemed to satisfactory excite most modes evenly, independent of the FEA model.

Sensor layout analysis

Determination of sensor locations follow a similar analysis as the excitation layout, but with different metrics to compare the models and proposed layouts. In addition, after defining 49 excitation positions, the sensor layout has to considerably reduce the number of placements to avoid an unmanageable number of tests. In linear system, the roving hammer approach should theoretically yield the same result as a roving sensor test (Eq. (3.28)), nevertheless from a testing point of view, a roving hammer approach is preferred in this case to avoid constantly changing the placement sensor and instead vary the impact location with a fixed sensor.

The first analysis on the models is mass loading sensitivity; the metric which quantifies the effect the mass of the accelerometer has on the response of the system. The addition of the accelerometer as a lumped mass can alter the modal solution (shapes and frequencies), and therefore, dynamic re-computation is performed to incorporate this effect. The mass of the accelerometer is set at 5 gr. which accounts for the accelerometer mass and cabling.

Figure 5.7 shows a mass loading sensitivity colourmap on the mesh for all three models and highlights the area that are more susceptible to mass loading effects (in red). Intuitively, the top section of the thin walls are problematic for all models.

Inspection of the absolute value of this sensitivity analysis, quantifies the amount that a sensor placement can vary the natural frequency of each mode. This is a useful

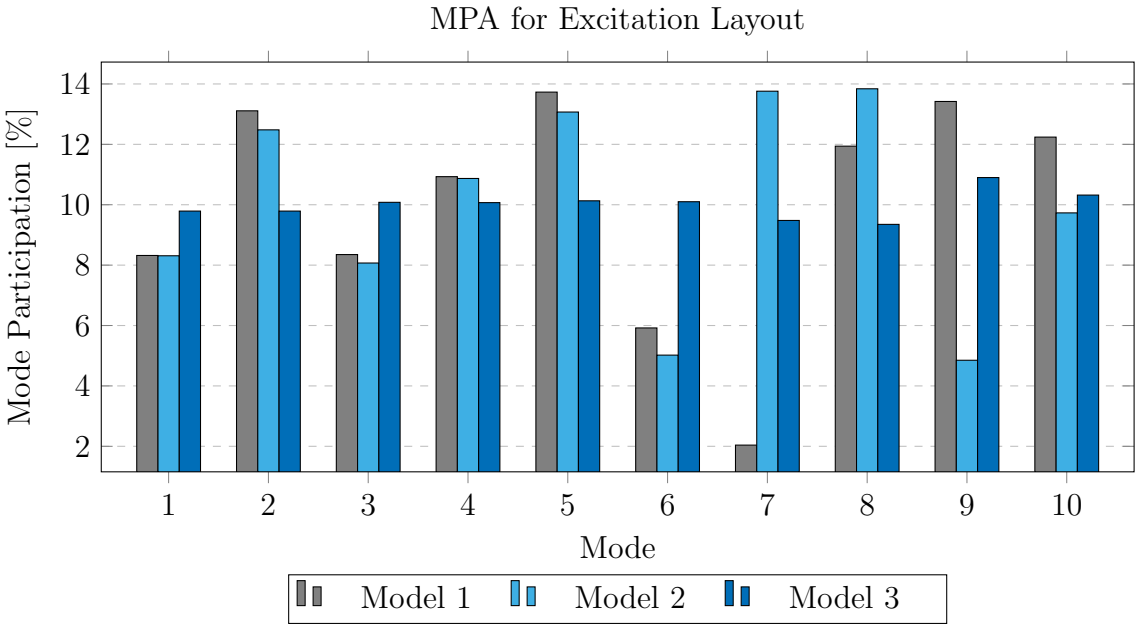

Figure 5.6: Mode participation analysis graph for the proposed excitation layout

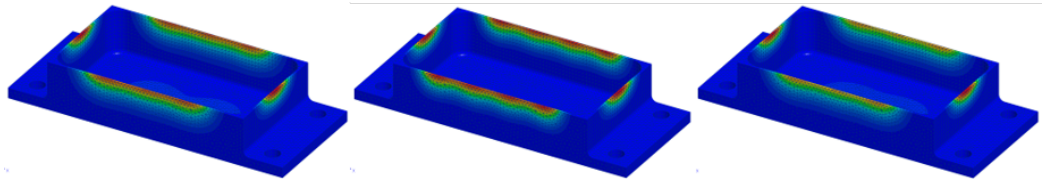

Figure 5.7: Average Mass loading sensitivity for models 1, 2 and 3 respectively

tool for understanding shifts in FRF peaks from one test to another. Given the roving hammer approach with alternating sensor placement, a re-computation of the modes and frequencies occurs for all of the proposed positions of the accelerometers.

As well as taking the mass loading effect into account, an important metric to determine an adequate positioning of the accelerometers is autoMAC computation (described in Eq. (3.51)). AutoMAC is a variant on the modal assurance criterion but instead of measuring consistency and linearity between analytical and experimental results, it checks for spatial aliasing and linear independence within the numerical result [116]. The diagonal terms are evidently unity (mode n is perfectly correlated to itself), but the off-diagonal terms can indicate whether spatial aliasing is possible and if more sensors (or at different locations) are required. Using these metrics, a sensor selection routine is conducted using the AutoMAC technique for the first five modes of each model. The resulting layout is compared with the AutoMAC metric on all three models. A successful sensor layout is one that has low number of placements,

and low off-diagonal terms.

When running iterations for five sensor placements and balancing AutoMAC values for all three models, Figure 5.8 shows that modelling the joint at the edges and flanges (models #1 and #2) have a close similarity between modes #1 and #3. The main difference between these modes is the phase relationship between the floor displacement and the long walls, resulting in a high AutoMAC off diagonal value for modes #1 and #3 in both models as seen in Figure 5.9.

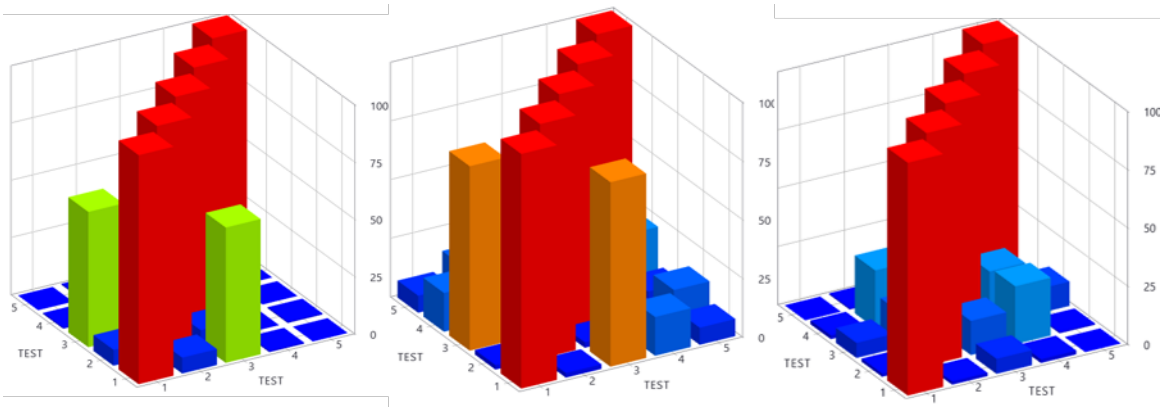

Figure 5.8: AutoMAC graphs for the proposed sensor configuration in models 1, 2 and 3 respectively

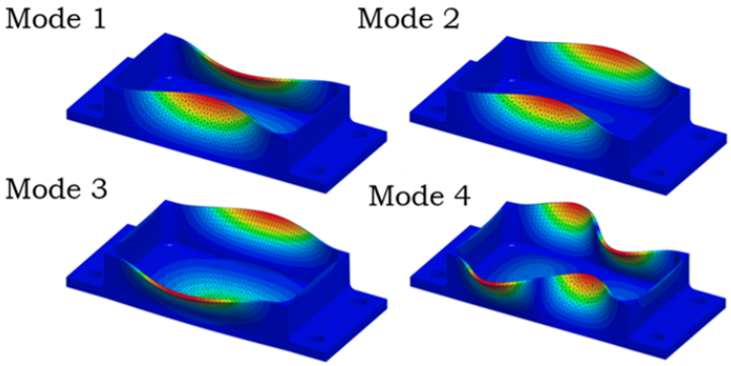

Figure 5.9: First four modes for the bolted model

If configurations were tailored for models #1 and #2, then model #3 is poor and vice versa. Given that the physical coupon has a hard backing at the bottom as a contact with the test table, low displacement of this face is expected and therefore it is decided to follow a better suiting layout for that of model #3.

Impact Hammer Testing

With the 5 sensor and 49 excitation layouts defined, the resulting 245 impact tests were performed on the coupon. The component was mounted on the table with the four M10 bolts and torqued to 30Nm using a calibrated torque wrench.

The component was also marked before the test, as seen on Figure 5.10, to indicate the excitation positions (marked with blue dot) and the accelerometer position (marked with black cross).

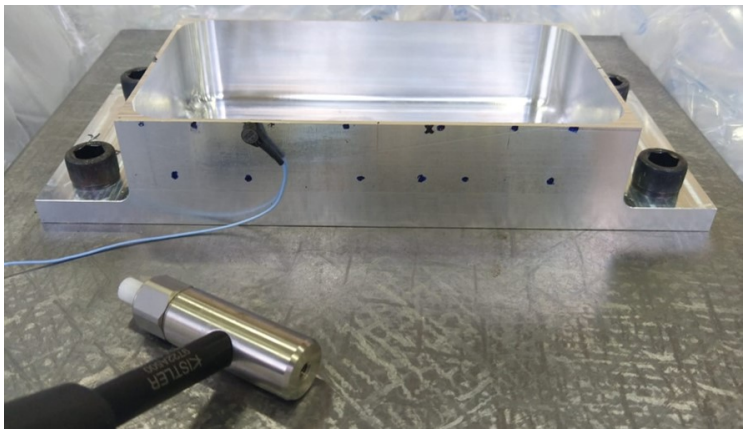

Figure 5.10: Experimental setup for the bolted coupon

Once these tests were performed using the CutPro suite, the resulting FRF was exported and translated into Universal File Format (UFF).

A series of observations are clear when plotting all these FRFs in Figure 5.11. Evident peaks can be observed at similar frequency ranges. By using the mass loading sensitivity analysis mentioned before, the plot is divided for the different sensors and colour-coded. Table 5.5 is a quantification of the frequency shift mass loading has, per sensor location, for each mode for the FEA result of model 3 (full bottom nodes fixed).

Joining the results of the FRFs with the mass loading sensitivity and quantification table, can explain the shifts and frequency ranges observed by each peak in the graph. The predicted FEA modes for model #3 have also been included. An example of this is the considerable shift in sensor #1 (blue curve) near the 2500 Hz region. This is mode #5, which has shifted considerably left. According to the mass loading table, the presence of this sensor can reduce the frequency of mode #5 by almost 360Hz. In similar fashion, sensor #2 (orange) does similar effect on mode #3 (observable at around 2000Hz) and sensors #3 and #5 (yellow and green) in mode 1.

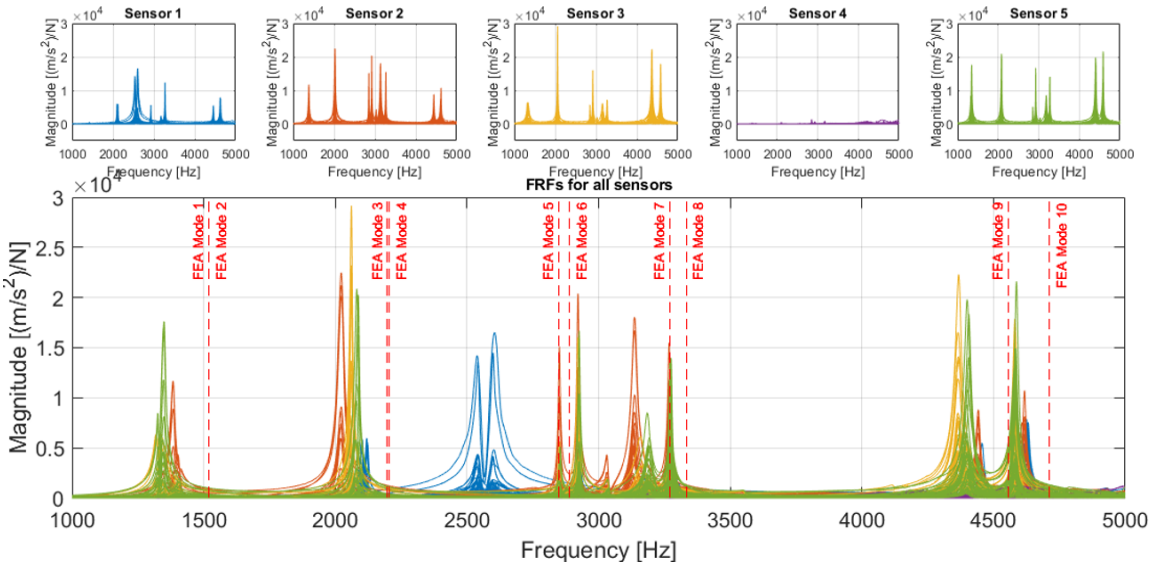

Figure 5.11: All magnitude FRFs for the bolted EMA with dashed lines marking the FEA mode frequencies

		Sensor 1		Sensor 2		Sensor 3		Sensor 4		Sensor 5	
Mode #	FEA freq. [Hz]	Mass Load freq. [Hz]	Δ%	Mass Load freq. [Hz]	Δ%	Mass Load freq. [Hz]	Δ%	Mass Load freq. [Hz]	Δ%	Mass Load freq. [Hz]	Δ%
1	**1520**	1520	0.0%	1482	-2.5%	1427	-6.1%	1520	0%	1427	-6.1%
2	**1520**	1520	0.0%	1520	0.0%	1520	0.0%	1520	0%	1520	0.0%
3	**2198**	2194	-0.2%	2079	-5.4%	2144	-2.4%	2198	0%	2145	-2.4%
4	**2205**	2205	0.0%	2202	-0.1%	2202	-0.1%	2205	0%	2201	-0.2%
5	**2848**	2489	-12.6%	2842	-0.2%	2846	-0.1%	2848	0%	2846	-0.1%
6	**2889**	2868	-0.7%	2888	0.0%	2887	-0.1%	2889	0%	2887	-0.1%
7	**3269**	3269	0.0%	3154	-3.5%	3248	-0.6%	3269	0%	3249	-0.6%
8	**3333**	3318	-0.4%	3308	-0.7%	3321	-0.3%	3333	0%	3321	-0.4%
9	**4556**	4555	0.0%	4536	-0.4%	4418	-3.0%	4556	0%	4418	-3.0%
10	**4712**	4702	-0.2%	4686	-0.5%	4653	-1.3%	4712	0%	4653	-1.3%

Table 5.5: Mass Loading effect of the proposed sensor layout on Full-bottom model

Having these mass loading effects in mind when running the modal parameter extractor requires attention in order to account for these apparent frequency shifts. Mass cancellation [105] is considered as a simple way of cleaning some signals of the mass loading effect, however this method can only be applied to point loading measurements (where excitation and response are considered at the same point), which is a single FRF per sensor. Expressions and derivations for cross FRFs have also been proposed [123].

Another interesting observation is the relatively inert response from sensor 4, which is located in the floor of the pocket. This is due to the low displacements expected on this section of the component.

One last observation on the FEA predicted modes has to do with the apparent pairing

between at least the first four modes differed in the phase of the opposing walls' displacement. This results in the frequencies for these pairs of modes to be close to each other, with differences of less than 7Hz.

EMA and FEA Pairing

With the previous observation in mind, a modal parameter extraction is performed on the EMA FRFs, following point and DOF pairing. To avoid the mass loading effects, the resonant frequencies and operational deflection shapes (ODS) are extracted referencing the less affected sensors, per predicted mode. The result is the extraction of nine experimental modes from the FRFs.

The first analysis of these extracted modes is to compare them with each other, using the same AutoMAC analysis of the sensor placements, seen in image (a) of Figure 5.12. There is an overall good independence of the extracted modes. Modes #1 and #2 , and of the EMA share a low degree of similarity (27.1%), which is acceptable given their difference in shape.

When these EMA results are compared to those of the FEA, side (b) of Figure 5.12, shows the level of correlation between the observed modes as a MAC matrix. Low levels of off-diagonal terms indicate a good independence of both FEA and EMA modes

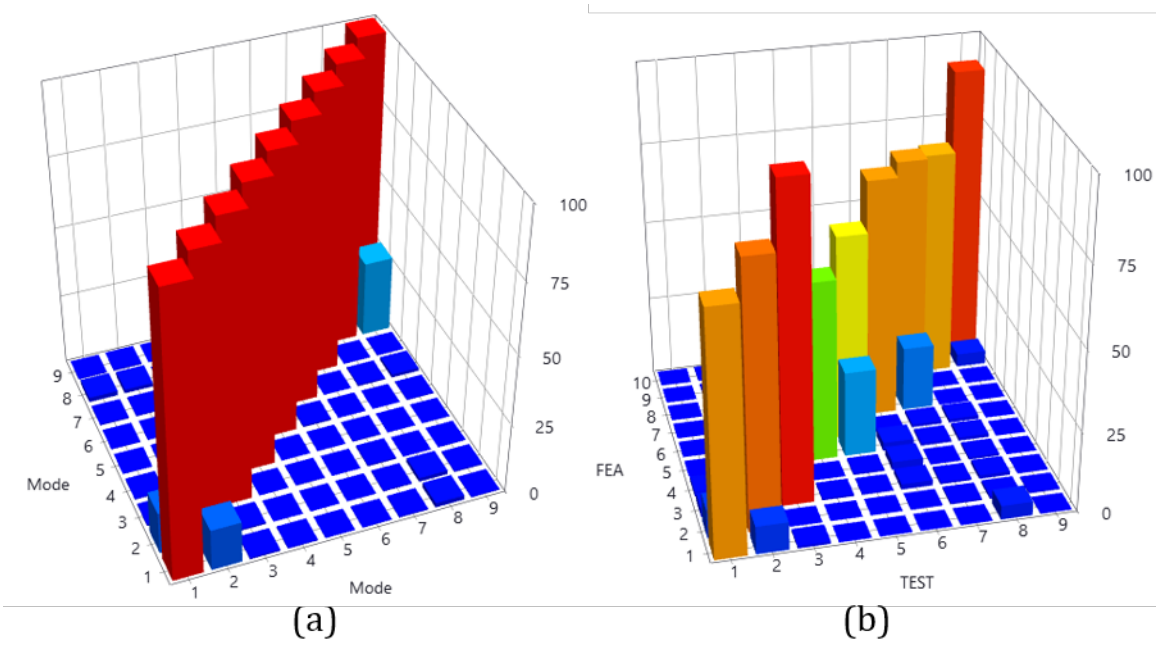

Figure 5.12: AutoMAC for the extracted EMA data (a). Initial MAC matrix between FEA and EMA data (b)

individually. The diagonal terms show better correlation in the first two modes, as well as the higher order from 7 to 10. The next step to understand these relations is through mode shape pairing, summarised in Table 5.6.

The results from this pairing can be analysed according to their mode shapes and the frequency estimation. On average the identified modes share around a 70% correlation coefficient for shape of paired modes under a MAC assessment. FEA modes #5 and #6 show the lowest level of correlation with 56 and 63% respectively. Despite adequate levels of shape correlation, frequency estimations are generally overestimated in FEA, with mode 1 presenting almost 14% difference. Even taking into account the mass loading quantification of the FEA modes, the overall EMA results are under the expected FEA frequencies. Model updating is the next step to calibrate the model to the observed dynamic behaviour.

5.3.3 Bolted Coupon Model Updating

Having adequate levels of pairing between the full bottom model and the EMA results, the next step is to update the model to get closer estimations on frequency and higher MAC coefficients. To perform these updating iterations, a secondary set of models looks at different methods by which this can be achieved. In summary the following approaches are employed:

a) *Material property update*: Similar to the free-free condition, only global values for E and ρ are updated for the complete coupon. This is the simplest form of updating and can only target frequency estimations and not mode shapes. This model is referred to as "Material Properties" in the following analysis.

b) *Boundary condition as spring elements*: This model converts the bottom face boundary condition nodes into Z direction spring elements to replicate a contact stiffness. Updating occurs locally allowing each element to adopt a required value needed to ensure better correlation. Two simulations are ran for this model, one targeting only frequency estimation and the other using both responses of frequency and MAC coefficients. These methods are referred to as "K_z" and "K_z+MAC" respectively.

c) *Interface layer modelling*: This method is adapted from various publications in the field of contact mechanics and interface models [100, 104], and tool holder assembly modelling [119]. A single simulation targeting frequency and MAC responses is performed. This method is referred to as "Interface layer".

	FEA		EMA			
Pair	Mode	Freq. [Hz]	Mode	Freq. [Hz]	Δ%	MAC %
1	1	1519.7	1	1326.3	14.58	74.9
2	2	1520.4	2	1391.7	9.25	82.2
3	4	2204.7	3	2109	4.22	97.8
4	5	2847.7	4	2850.9	-0.12	56.2
5	6	2889.1	5	2921.3	-1.1	63.9
6	7	3269.3	6	3133.5	4.33	74.8
7	8	3332.6	7	3267.7	1.99	74.8
8	9	4555.8	8	4364.5	4.38	71.1
9	10	4712.1	9	4581.3	2.86	91.7

Table 5.6: Mode shape pairing between FEA and EMA and MAC Matrix coefficient

The correlation parameter for all four models is the absolute difference between simulation and test,$\left(\frac{|\omega_i^s - \omega_i^t|}{|\omega_i^t|}\right)$, rather than mean. These correlation coefficients are applicable for both frequency estimations and MAC coefficients, depending on the selected responses.

Finally, all models undergo a parameter convergence analysis to ensure the iterations are approximating the desired values properly. After running all simulations and updating routines, a summary is presented in Table 5.7 and Figures 5.13 and 5.14.

All results are contrasted with the baseline FEA model that has not been updated and is the original starting point for all. The first overall observation has to do with all updating routines being able to reduce the overall error of the frequency estimations, despite the fact that they also increase the error of modes #4 and #5, which have the lowest MAC coefficients of the pairings. This raises the discussion on the importance of having high MAC coefficients in order to provide better updating results for all

	Mode	**1**	**2**	**3**	**4**	**5**	**6**	**7**	**8**	**9**	**Mean**
Model	**EMA** [Hz]	**1326**	**1392**	**2109**	**2851**	**2921**	**3134**	**3268**	**4365**	**4581**	**Error**
Baseline	f_n [Hz]	1520	1520	2198	2848	2889	3269	3333	4556	4712	
FEA	Error [%]	14.6	9.2	4.2	0.1	1.1	4.3	1.9	4.4	2.9	4.76%
Material	f_n [Hz]	1457	1458	2107	2730	2770	3135	3195	4368	4518	
Properties	Error [%]	9.8	4.7	0.1	4.2	5.2	0.0	2.2	0.1	1.4	3.09%
Kz	f_n [Hz]	1407	1516	2115	2609	2797	3218	3283	4437	4668	
	Error [%]	6.1	8.9	0.3	-8.5	-4.3	2.7	0.5	1.7	1.9	3.87%
Kz	Frequency [Hz]	1270	1517	2096	2659	2779	3188	3245	4394	4503	
+ MAC	Error [%]	-4.3	9.0	-0.6	-6.7	-4.9	1.7	-0.7	0.7	-1.7	3.37%
Interface	Frequency [Hz]	1370	1372	2059	2800	2863	3129	3222	4396	4567	
Layer	Error [%]	3.3	-1.4	-2.4	-1.8	-2.0	-0.1	-1.4	0.7	-0.3	1.49%

Table 5.7: Summary of updated simulations

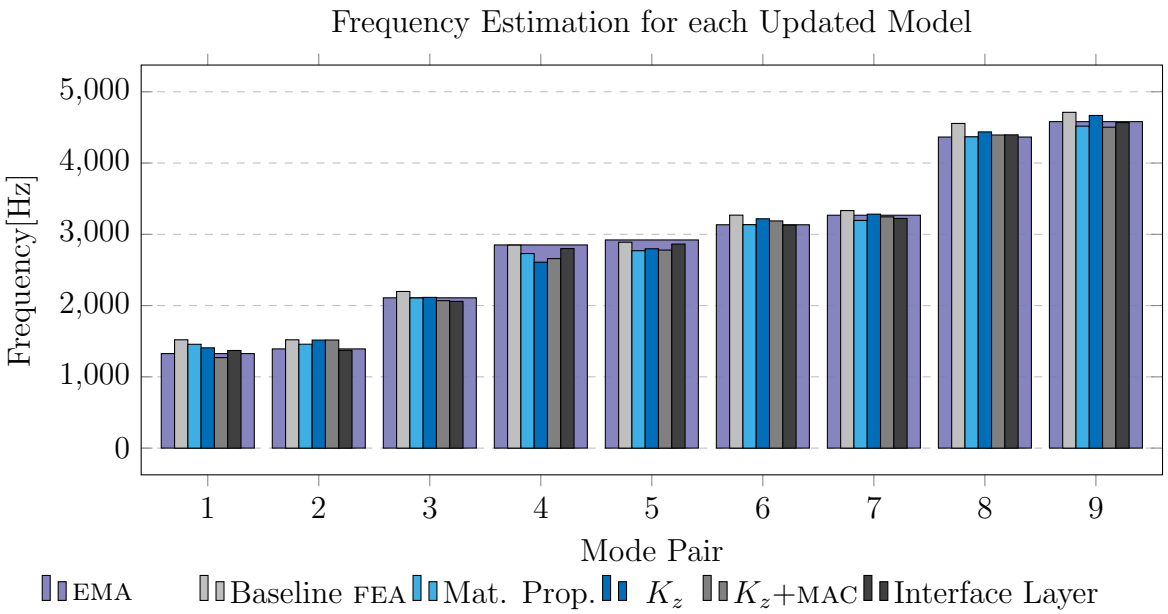

Figure 5.13: Frequency estimation for baseline and updated models

modes.

Interesting behaviours can also be observed for each model. When updating solely on material properties, the overall error decreased from 4.8% to 3.1%, however the resulting material parameters are physically questionable as elastic modulus was up-

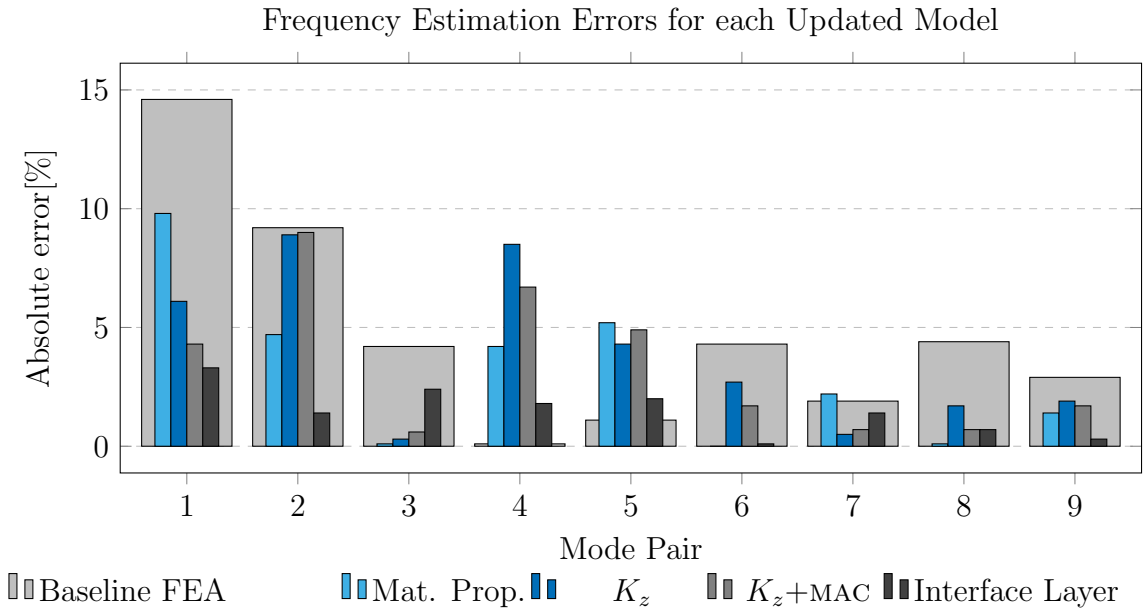

Figure 5.14: Absolute error in frequency estimations for all methods and baseline FEA model.

dated to 67.9 GPa, which is slightly under the lower limit for the alloy (70 GPa) and even farther from the updated free-free condition value. The updated density of this model, however, is still within expected values at 2867 kg/m^3. Nevertheless, the frequency estimation for mode #1 (which has the highest error in the baseline model) decreased from 14.6% to 9.9%.

When the boundary condition is transformed to spring elements and updated locally, the overall result closes in to the desired values within a 4% error band, however there is a large discrepancy on modes #2, #4 and #5, despite the second model targeting the MAC coefficients as well. The stiffness values for each node present a wide range with some areas having an order of magnitude difference between them. Figure 5.15 shows a map of the updated stiffness values on a normalised/relative scale. Stiffening has occurred at the flange edges and also, but to a lesser degree, under the floor of the pocket. The result does not show clear indication of bolt pressure cones as areas of increased relative stiffness, and instead a potential distortion in the coupon is stressed by the joint when clamped onto the surface and impart a greater effect on the overall joint characterisation.

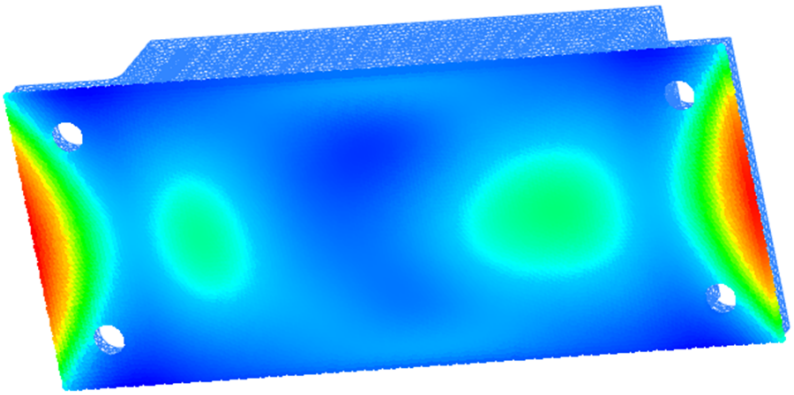

Figure 5.15: Relative stiffness values for the Kz model

Overall observations for this method have to highlight the fact that more iteration steps and computational times were involved, namely 11 iteration steps on each model. Because this method updates values individually for each node of the bottom surface, around 11601 in total, convergence is harder and requires more resources to ensure. The method can provide enhancements to initial FEA simulations, however the feasibility and efficacy to run batch simulations for further applications is questionable. The last method employed is the interface layer method. This substructuring technique linearly approximates the interaction of contacting surfaces by means of a vir-

tual material. This useful technique has been employed in bolted joint modal analysis [100], [104]. Global parameters for this layer were updated and yielded values of 42.7 GPa for elastic modulus, density of 2741 kg/m^3 and 0.29 Poisson's ratio. Despite the odd values obtained, they are in the same order of magnitude as the original parent material, furthermore, this method has reportedly been taken extremes [100] and, despite the updated interface layer having more than two orders of magnitude difference with the parent material, results are still deemed serviceable for modelling activities. With this in mind, the updated results obtained for this model are capable of reducing the overall error from 4.76% to 1.49%, with any individual frequency estimation under the 3% range. Furthermore, this method was also capable of increasing slightly the diagonal MAC coefficients from an average 76% to 79%. Again, the repeated issue with modes #4 and #5 can be observed as the error increased from 0.1% and 1.1%, respectively, to 1.8% and 2.0%. Nevertheless, the overall behaviour of the model is a considerable improvement from the baseline FEA model.

A final observation on this method has to do with the lower computational times and required iterations when compared to the spring element method. As this model works globally on elements rather than nodes, the number of parameters is considerably reduced to around 5820, enhancing computational times and convergence of parameters. Compared to the previous method, the interface layer took 7 iteration steps to fulfil the target criterion. This is a promising aspect for application on other geometries and batch file runs.

5.4 Discussion and Summary

The evaluated component has served as a learning experience for a number of aspects of modal analysis in general. Starting with the comparison of modelling platforms, namely ABAQUS and FEMTOOLS, and the differences their solvers impart onto the results obtained. Despite narrowing the analysis to linear evaluation some (although small) discrepancies were observed. In this area, a valuable observation is that FEMTOOLS is somewhat limited, compared to ABAQUS, for non-linear modelling, despite having some tools for non-linear analysis of experimental data. However, given that the quantification of non-linear behaviour is not within the scope of this project, FEMTOOLS provided considerable benefits in computational times and model updating capabilities. It is determined that dynamic solving and updating activities are carried out in FEMTOOLS, whilst meshing and *inp* file creation are performed on

ABAQUS. This separation of modelling activities highlights the importance of capable meshing protocols and quality checks required prior to modelling.

Another valuable lesson learnt in this Chapter is the need for feedback from the model to create proper EMA planning, particularly in the sensor and excitation layout definition. The free-free condition section saw the shortfalls of over-simplifying this point and employed layouts that were sub-optimal. This issue was rectified for the bolted component, which saw a clear improvement reflected in a better MAC matrix for the paired modes. Although in this case mass loading played a relevant role in the treatment of experimental results, using the FEA capabilities, these frequency shifts were calculated and corroborated against the experimental FRFs.

With respect to the modal testing in general, it can be concluded from this work that in order to develop a comprehensive EMA analysis on the component, a high number of tests are beneficial. Unfortunately in this case, only a single accelerometer was available, which slowed the process down considerable and also slightly changed the characteristics of the system between each test by changing the position of this lumped mass.

Nonetheless, the model updating showcased its capabilities for calibrating FEA models. Different approaches were compared by looking at either restitution coefficients of the contacting elements, or by introduction of a virtual interface layer. All these methods offered an improvement to the baseline model which is a step forward. The interface layer method in particular produced both a better result and also lower computational times than the other methods. However, this method is known to linearize the interface dynamics, which for use in this study is acceptable due to the linear approach premise sustained in both FE modelling and impact hammer testing approaches used. The scope of this study did not include the evaluation of non-linearities of the bolted joint (although an interesting avenue of research), and given low input forces from the impact hammer, expected the system to remain in the linear non-slip range of the joint's behaviour without a marked hysteretic behaviour [124, 125, 126].

This uncovers the final point this chapter aimed to target, which has to do with the definition and applicability of these methods for the determination of reduced fixturing alternatives and optimal workholding layouts to enable double sided access. Understanding that detailed evaluation of fixturing elements has a defined non-linear behaviour, the presented updated methods offered an acceptable level of improvement

to a nominal and non-validated model. This can then be employed as a resource for updating routines in DSA simulations and optimisation. Furthermore, in the upcoming Chapter 6, model updating based on the interface layer method is employed to complement the optimisation of a DSA assembly. Working in two stages, model updating is firstly performed on the fixturing frame to improve the characterisation of welded joints. In a second stage, the assembly of the frame, vice clamps and billet are also experimentally measured and the FEA model updated using the interface layer for joints between billet and vice. Interestingly, Chapter 7 bases the optimisation of breakaway tabs on updated stiffness parameters for boundary condition spring elements, as it provides better results in that particular case. These next chapters are constantly evoking the tools and methods discussed previously and confirm the utility in the detailed examination of updating approaches presented in the present chapter.

Chapter 6

External Workholding Optimisation for Double Sided Billets

In Chapter 4 an executable program was developed to automate FEA based simulations within an optimisation routine. In this Chapter, the system is extended to include the model updating procedures studied in Chapter 5 and derive optimal layouts for external workholding of double-sided workpieces. This chapter aims at expanding the optimisation application to scenarios where exhaustive searches are impractical.

The initial goal is to evaluate the repeatability and reliability of the PSO and provide guidelines for adequate implementation, which is a central objective of the project. For this, the first part of this Chapter, Section 6.1, explores the of effects different user-defined variables has on optimal layout solutions for a single isolated billet, representative of an initial stock condition in DSA environments. Variations in the simulations include number of vices, edge restrictions, billet aspect ratios, swarm parameters and objective function definitions. This latter point relates to another key objective of the Thesis, which aims at linking chatter avoidance and machining stability with fixturing and workholding design optimisation. A secondary objective of this section is to provide a varied set of application cases for the optimisation program and measure its performance and reliability.

In the second part, Section 6.2, the additional complexity of representative DSA assemblies is introduced by means of incorporating a fixture frame where the workholding

elements are mounted. Understanding how the holding elements of a billet on a support structure alters the dynamic behaviour of the assembled system is paramount for industrial applications. Targeting this central objective requires multi-body assembly techniques to be introduced in order to model the complete structure. This activity is also complemented by the experimental evaluation and model updating tools developed in Chapter 5 as a basis for the optimisation routine.

6.1 Isolated Billet

As presented in the optimisation programming section of Chapter 3, the initialisation of the optimisation program requires a set of user defined variables. These are grouped into two main areas; the physical properties of billet and vices, and the simulation parameters.

The first group determines all relevant physical quantities for both the part and the work-holding elements. These include the clamping lengths and numbers of available vices, as well as the size of the billet, material properties, and edge availability. This edge availability aspect determines whether particular sections of the billet perimeter must be free of vices. Either for loading and unloading of the workpiece or due to pre-imposed design features of the machining environment, a billet might require a definition of edge availability, and therefore the optimisation program has been coded to account for this requirement and enhance its versatility. In a similar way, the number of vices is also a point of careful consideration. When implementing various vices, precise alignment between them must be ensured in order to avoid workholding-based deformations and stresses on the part. A higher number of vices is associated with longer setup times and maximising this variable does not necessarily ensure more efficient workholding solutions.

The second group of user defined variables gathers all the simulation specific terms, for both the FEA modelling, as well as the PSO swarm parameters. On the modelling front, a part mesh (and its associated **.inp* file) are predefined and the material properties introduced. The relevant mesh quality metrics (Section 3.2.1) are assessed and the necessary refinements introduced. In this case, given the steep transition a vice boundary condition imposes on the part, a localised element refinement is performed on the outer perimeter, as seen in Figure 6.1.

An objective function must be defined against which the optimisation program shall operate. Two related objective functions have been programmed to run on the PSO

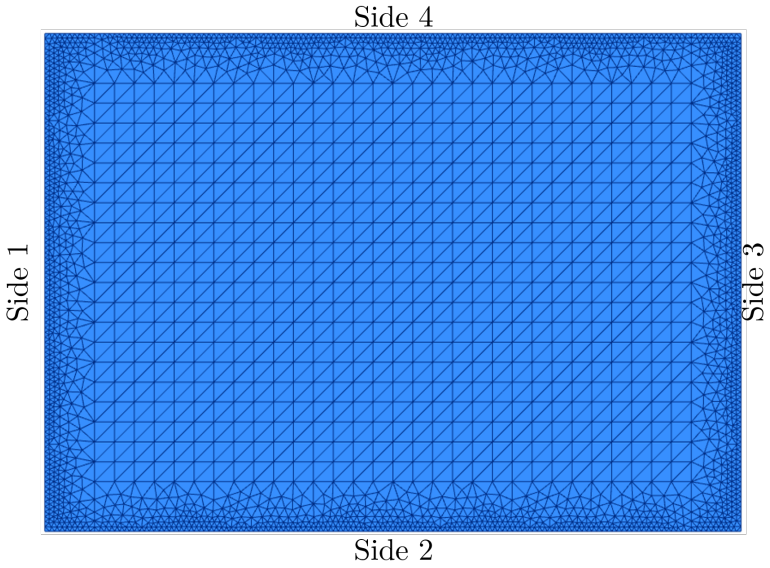

Figure 6.1: Billet mesh and side numbering

(detailed in Section 4.2). One approach prioritises the direct receptance values and will only evaluate and determine the optimal layout based on the FEA receptances. The second approach adds the $a_{p,crit}$ calculation and presents a secondary computation instance on the FEA receptances, introducing generic cutting conditions, to determine an $a_{p,crit}$ value at each extraction point (Fig. 4.3). This method is hereon referred to as the depth of cut approach.

Finally, one last crucial user defined variable for simulation definitions is the swarm size and extent. The comparison section of exhaustive searches against PSO routines used different swarms for each case. The single vice PSO runs a 25 particle and 35 generation swarm, whilst the dual vice case uses a 30 particle 50 generation swarm. This highlights the relevance of running multiple simulations that can test the effect of these variables and aim to provide a good balance between solution convergence and simulation time. It is expected that larger search spaces will necessarily require larger PSO routines for adequate convergence behaviour.

6.1.1 Receptance based simulations

This section focuses on troubleshooting and evaluating the performance of the PSO optimisation using different swarm parameters and using a direct receptance fitness function definition (Section 4.2.2). This approach looks at maximising the negative real-valued part of the direct receptance FRFs from the evaluation points (Eq. (4.14)).

The initial objective in this section is to gauge what balance of swarm size, generation limits and computational times associated to derive adequate and stable convergence curves. This is targeted using a common stock material format of a rectangular billet and using the receptance fitness function approach mentioned previously. An edge restriction is placed on four vice simulations to replicate physical loading procedures and potential constraints a billet might have.

Four vices with edge restriction

The first pair of simulations (Sim-1 and Sim-2) compares the convergence behaviour using the same billet and swarm parameters, and are therefore considered to be a repeated set of simulations. Although a repeat of each other, given the randomised seeding of particles within the PSO definition, the swarm behaviour is expected to differ in its initial stages. For this case, a rectangular billet of dimensions 700 $\times$ 500 $\times$ 60 mm is used as the workpiece with four 125mm long vices. The first two swarms are based upon 50 particles and 25 generations, using a receptance approach. Side 4 (topmost long edge) is restricted from vice placements, to reflect a vertical loading configuration. A third trial is also ran on this set-up, but inverting the swarm parameters and using 25 seeds for 50 generations.

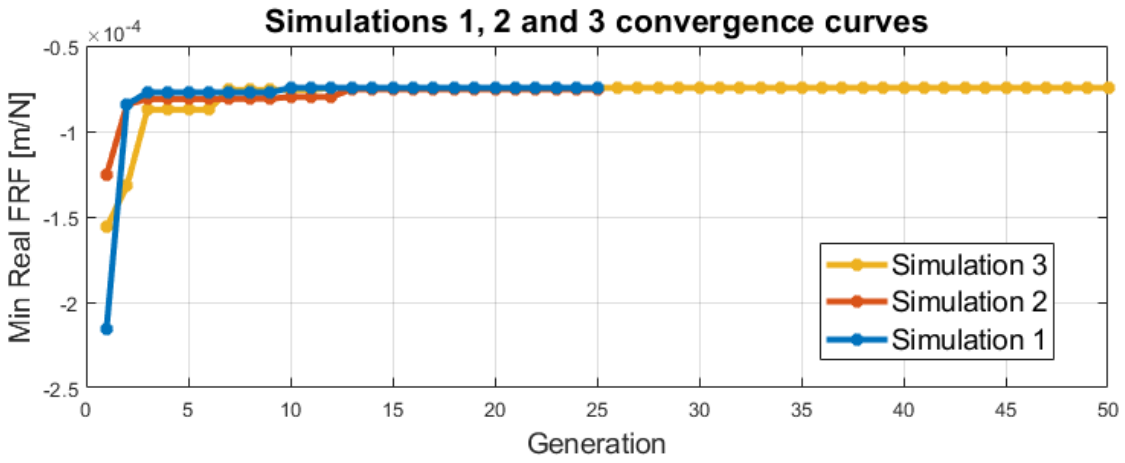

Figure 6.2: Simulations 1,2 and 3 convergences curves

The results from these repeated simulations are observed by their *convergence curve*, which plots the evolution of the best fitness function result of all particles (P_{best}) at each generation. In this case, Figure 6.2 exhibits that all three simulations reach the same fitness function value of approximately $-7.5 \cdot 10^{-5}[m/N]$. Sim-1 settles in this value after 10 generations, whilst Sim-2 does so at generation 13 and Sim-3 at

11. Interestingly, Sim-1 started the search with worse seeds than Sim-2 and Sim-3, represented by the notable difference in fitness value at generation 1.

A complementary way of evaluating the optimal layouts obtained is to graphically plot each optimal solution. Overlaying the sets of results yields Figure 6.3, which highlights the closeness of results obtained by all simulations, with vice placements differing by less than 3mm. The results present a somewhat intuitive layout for the presented setup, with the vices placed on opposite short edges, which increases confidence in the suitability of the PSO based on common machining practices.

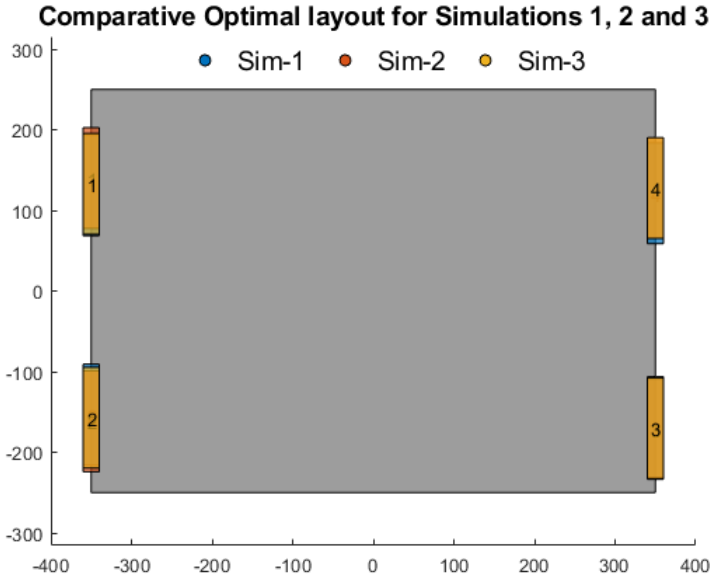

Figure 6.3: Simulations 1, 2 and 3 optimal layouts

Three vices on all edges

The next set of tests use the same billet, but looks at placing three vices with no limitations on the edge availability. It aims at complementing the swarm size parameter tuning by running slightly different swarms. Both simulations are based on 40 generations, but Sim-4 uses 20 particles whereas Sim-5 uses 25.

In the same fashion as the previous simulations, results are compared by observing their convergence curves of Figure 6.4, where both simulations converge onto the same fitness function value of around $-9.1 \cdot 10^{-5}[m/N]$. In this case, Sim-5 reached its maximum at generation 11, whilst Sim-4 took until generation 18 to reach the same value. This difference is, as stated before, due to the random nature of seeding within the PSO, but it is also sustained by a smaller swarm size, which is known to contribute to slower convergence rates y lower performance [127].

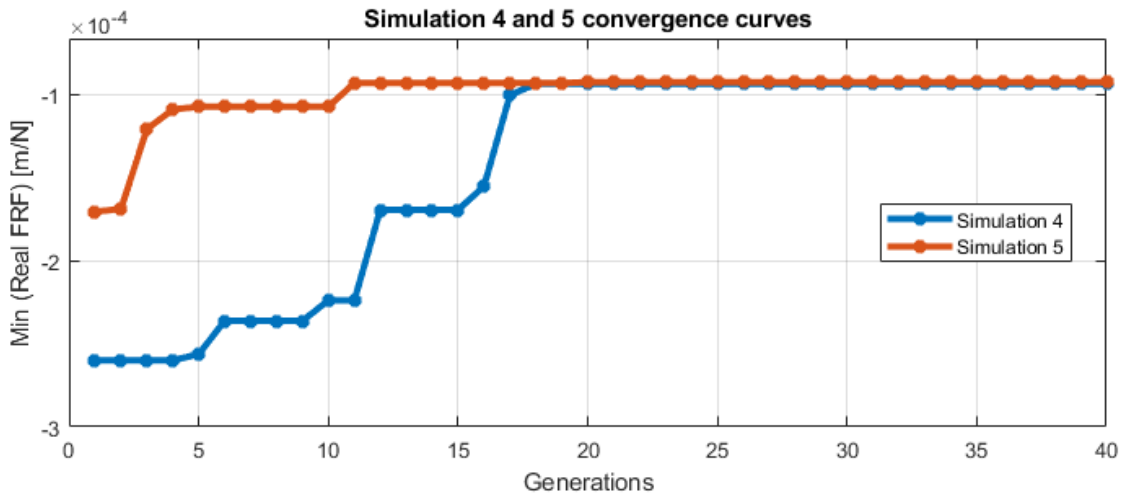

Figure 6.4: Simulations 4 and 5 convergences curves

The graphical layout representation of these optimal layouts is presented in Figure 6.5a and highlights some interesting results. First, and most importantly, is that initial inspection could deem both layouts to be considerably different from one another, despite their close fitness function values. However, due to the twofold symmetric nature of the search space, a reflection along the central Y axis, projects Sim-5 onto nearly identical results as Sim-4 (Figure 6.5) and can be considered to be coinciding layouts. In this case, the vices have been given a slight degree of transparency in order to observe acute alignment comparisons, particularly the difference in the top vice, which has a slight positioning difference of 6.14mm. The other vices are within 2mm of each other. This subtle variation in positioning results in a variation of fitness function values under 0.97% between both simulations.

Another observation is that the resulting layout is not necessarily an expected result for the given variables and common machining practices. This optimal and slightly off-centre disposition of vices provides an increase of 54% in fitness function values, when compared to fully centred vices on all three available edges (-1.98 to -0.91 $[\cdot 10^{-4} mN^{-1}]$). Despite these simulations being intended for testing the reliability of the optimisation programming, this result goes on to showcase the applicability and usefulness that can stem out of it by presenting an unconventional arrangement of external workholding.

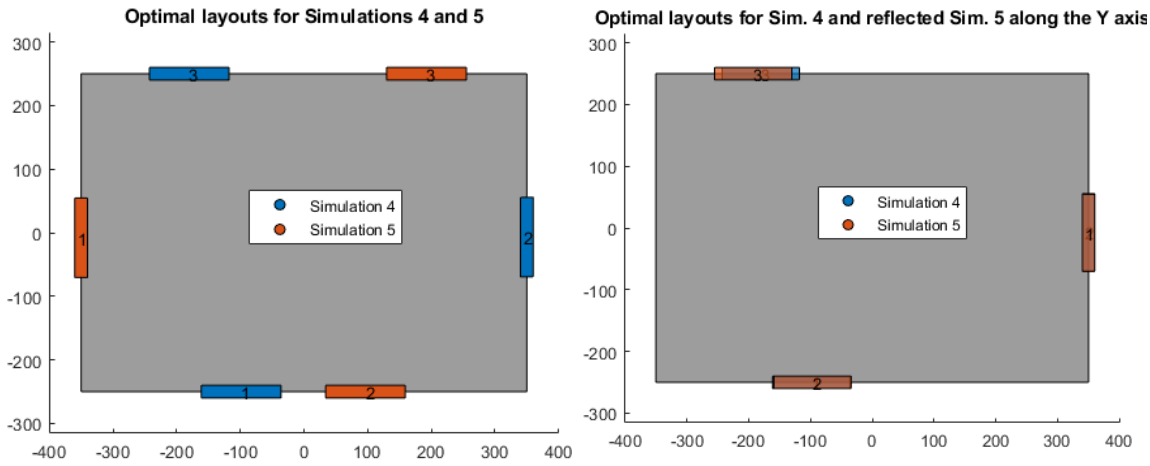

(a) Optimal results from Sim. 4 and 5

(b) Reflected version of Sim. 5

Figure 6.5: Simulations 4 and 5 Optimal layout results

6.1.2 Depth of cut based simulations

As discussed in previous sections, the fitness function can also be based upon calculations of $a_{p,crit}$ outlined in Section 4.12. In order to implement a calculation of this fitness function, certain cutting parameters must be introduced. For this, a commonly used tooling parameter set was assumed consisting of: 3 flute, ⌀16mm tool at 50% radial engagement. Machine dynamics were assumed rigid as the aim for this work is to quantify the workpiece based dynamics and the assumption that reduced fixture environments as this one, present significantly lower levels of stiffness than a production environment machining centre. The method used for calculating the a_p values of all lobes is done via a *zeroeth order approximation* (ZOA), derived from [10]. This method has had significant examination in numerous publications over the years, and has been accepted as a reliable approach as long as . For each layout, the evaluation of this fitness function is determined as follows:

a) With defined tooling parameters, the *directional milling coefficients* can be calculated (as a function of entry and exit angles).

b) The oriented FRF is computed for each evaluation point and the eigenvalues for the the characteristic equation are calculated.

c) The eigenvalue that conveys the lowest $a_{p,crit}$ determines the temporary value for an evaluation point.

d) After calculating all evaluation points, the lowest $a_{p,crit}$ defines the fitness function of the layout.

Three and four vice simulations

To compare the variations in behaviour for the PSO solver using the SLD based fitness function, Simulations 6 and 7 run using the same scenario of Simulation 4 and 5 but using this new fitness function definition. This type of simulations is also ran for 4 vices with edge 4 restriction analogous to Simulation 3.

The convergence curves of Simulations 6 and 7 are presented in Figure 6.6. Initially run for only 40 generations, Simulation 6 reached an optimum result in generation 29 and is extended up to 50 generations to ensure adequate convergence of the layout. Simulation 7 is set as a repeat of the previous, but with a unique initialisation resulting in different behaviour at the beginning of the program, but eventually converging onto almost the same fitness value. In this case, the convergence curve is plotted against

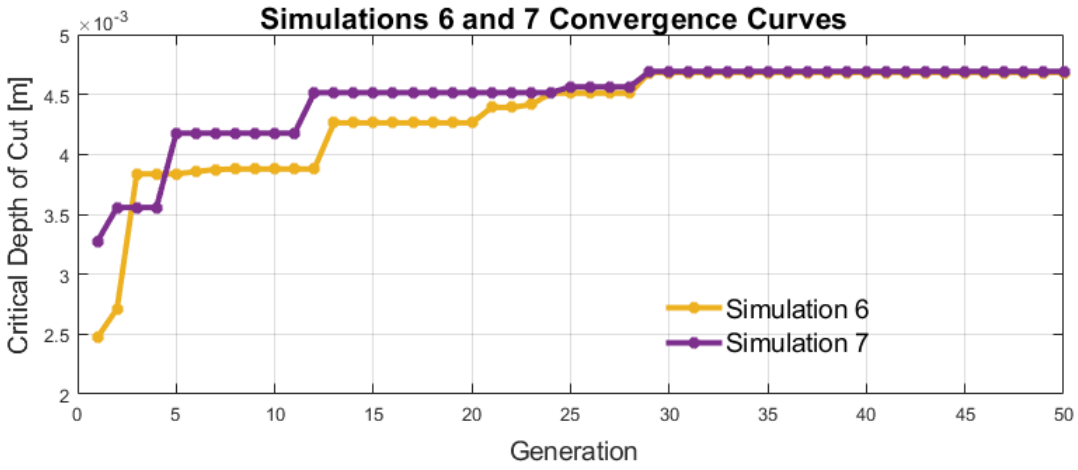

Figure 6.6: Convergence curve for Simulations 6 and 7

the critical depth of cut fitness function, which yields values close to 4.69mm of stepdown (or axial engagement).

The resulting layouts from these simulations are presented in Figure 6.7 and display the same layouts obtained as the FRF based simulations, adding further confirmation and reassurance to the obtained results and repeatability of the PSO program.

To complement the understanding of how this fitness function works, Figure 6.8 presents the stability lobe diagrams of all 15 evaluation points on the component. The SLDs that present the highest and lowest values of $a_{p,crit}$ are highlighted to help visualise how the relative position within the vice affects the stable depth of cut limit prediction. The maximum SLD corresponds to evaluation point 4 (Fig. 6.7) which lies just above vice 3, and therefore is a rigid section of the billet. In contrast, the

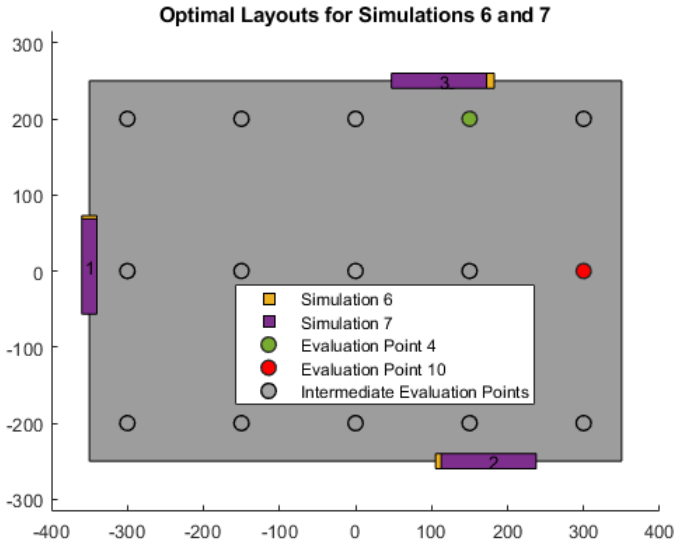

Figure 6.7: Simulations 6 and 7 optimal layouts

lowest valued SLD comes from evaluation point 10, which is situated at the mid-point of vices 2 and 3. Its lowest value coincides with the fitness function of the simulation. The dashed lines in between, plot the remaining SLD curves from the other evaluation points, whose values lie between the maximum and minimum.

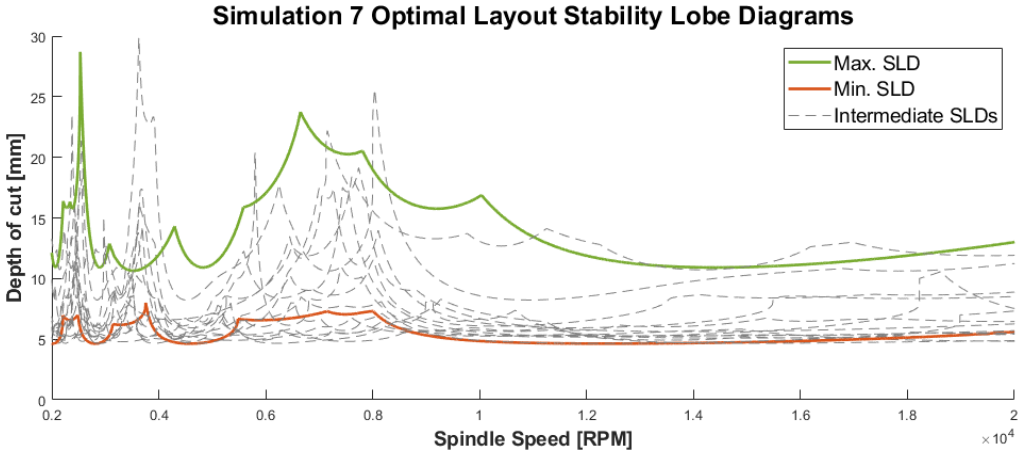

Figure 6.8: SLD curves for all evaluation points of Simulation 7

The last run using this fitness function metric is simulation 8 and models a four vice evaluation on only three sides of the billet (similar to Sim. 1,2 and 3). Its convergence curve is presented in Figure 6.9 and stabilises at a value of 4.91mm.

In this case, no repeat simulation is run and the layout comparison is performed against the results of Simulation 3, seen in Figure 6.10. The variations in optimal

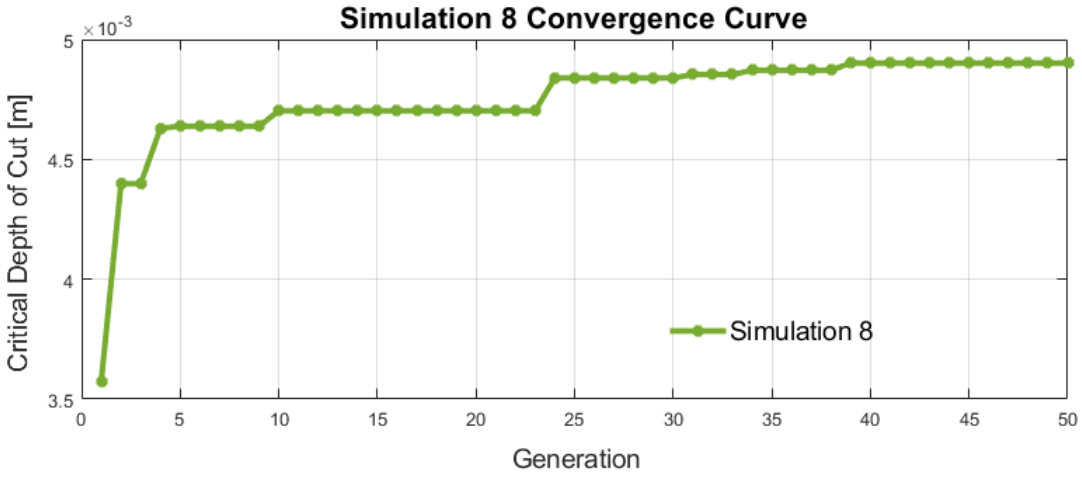

Figure 6.9: Convergence curve for Simulation 8

layout present under 4.5mm difference in the placement of vices 1 and 3.

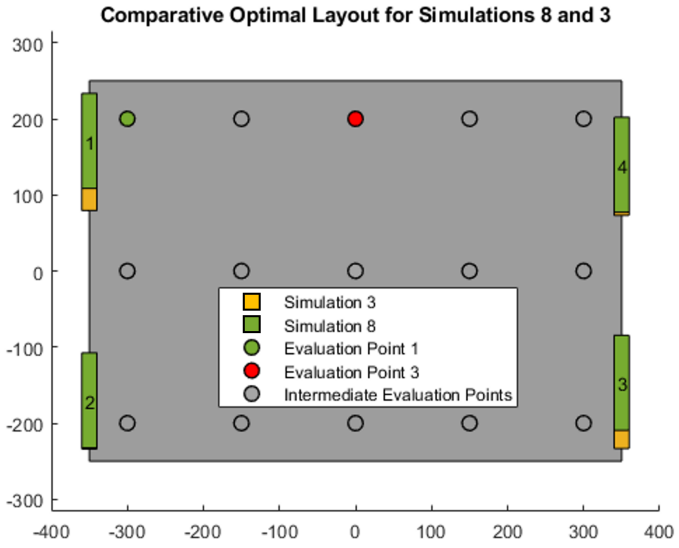

Figure 6.10: Simulation 8 optimal layout compared against Simulation 3

From these tests an interesting and reassuring conclusion can be drawn regarding the efficacy of optimising with the direct receptance metric of Section 6.1.1. This is noteworthy because both methods establish practically the same optimal layouts, despite the receptance approach commonly governed by out-of-plane FRFs (z direction), whilst the depth of cut approach utilises x and y direction driving point receptance values. This is because the ZOA method used to derive the SLDs only requires the in-plane FRFs and cutting conditions to calculate the oriented FRF and subsequently

the eigenvalues that determine $a_{p,crit}$ (Section 4.2.3). For this particular case, the coinciding results of both approaches also alleviates the intrinsic limitations within the ZOA method employed. This, due to the simplification of the system to exclusively consider in-plane receptance and disregarding axial forces in the z direction, related to helix angles in endmills [10]. Alongside the axial force aspect, endmill helix angles also involve a height dependent delay in terms of cutting engagement [120] that further distances this ZOA approach accuracy for endmill machining scenarios. Understanding these limitations, and in light of the aforementioned results, evaluating this approach is still considered a useful exercise.

As with the previous case, the SLD from all evaluation points are plotted in Figure 6.11. In this case, minimum and maximum values are obtained from evaluation points 3 and 1 respectively (see Fig. 6.10).

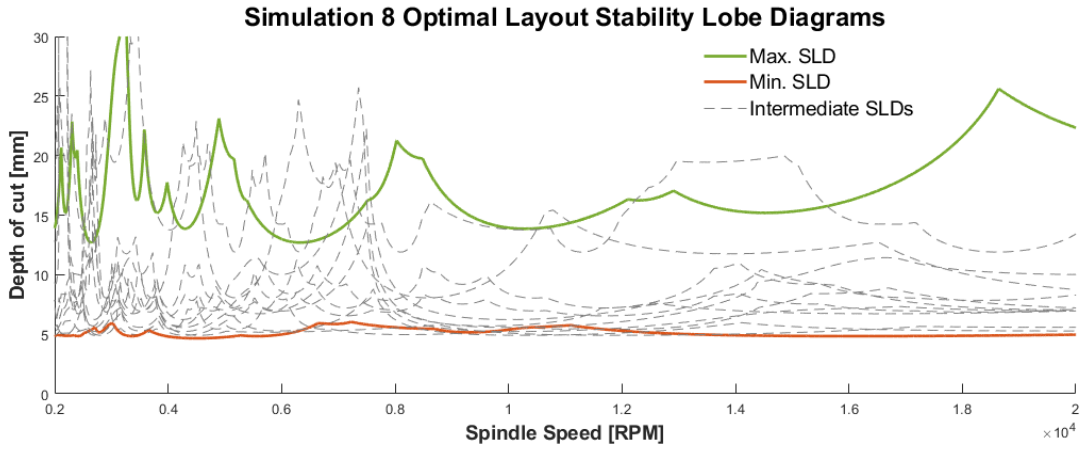

Figure 6.11: SLD curves for Simulation 8

6.1.3 Aspect ratio simulations

Expanding on the isolated billet approach, a set of simulations evaluate the effect of using different aspect ratio billets. This activity is meant to, firstly, trial the versatility of the optimisation architecture for accommodating different billet geometries. Secondly, by increasing the dimensions of the stock condition to 1000 × 500mm following a 2:1 ratio, and then to 1500 × 500 for a 3:1, optimisation runs can provide valuable insights on how optimal solutions evolve and adapt to sequentially increasing dimensions.

The modifications required for the PSO program to operate on this new size billet, are simply the new part mesh *inp* files. The program is scripted in such a way that

proportional scaling of the FRF evaluation points and node selection functions are automated.

Following a similar testing condition as the previous simulations, three and four vice configurations are tested on the 2:1 sized billet and use the depth of cut approach. In contrast, the 3:1 billet is modelled only with the 4 vice constraint and using the receptance metric.

Simulation 9 and 10 are on a 2:1 billet with three and four vices respectively. Their convergence curves have been plotted alongside one another in Figure 6.12.

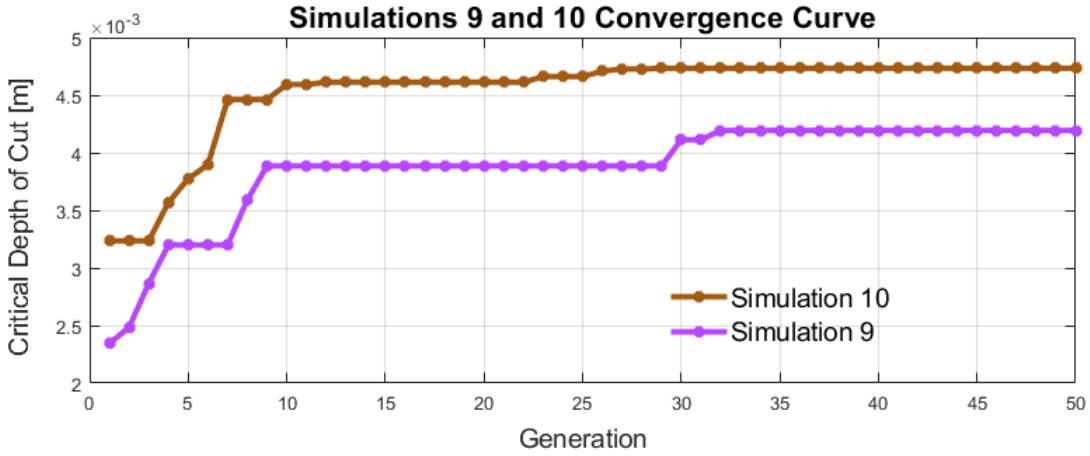

Figure 6.12: Simulations 9 and 10 on a 2:1 sized billet

As expected, the critical depths of cut are lower than the smaller billet tested previously. In consequence, this larger sized billet benefits more from an extra vice, improving the depth limit by 17% from 4.1 to 4.8mm. The associated layouts are presented in Figure 6.13. On one side, Sim. 9 presents a similar type of layout to the other three vice configurations, however the short side vice in this case is drawn closer towards the corner. More surprisingly, the result of Sim. 10, presents vices on the bottom long edge, as opposed to both pairs on the shorter sides. The result is unexpected and not entirely intuitive, but manual inspections on layout variations still yield lower $a_{p,crit}$ than the optimised version. This behaviour is linked to the observation of the depth of cut approach looks at ensuring rigidity in the in-plane direction, rather than out-of-plane, which in a larger billet can be more differentiated from one another.

The last simulation testing aspect ratio variations is performed on a 1500 × 500mm billet and tested using only a 4 vice condition. Its convergence curve and optimal

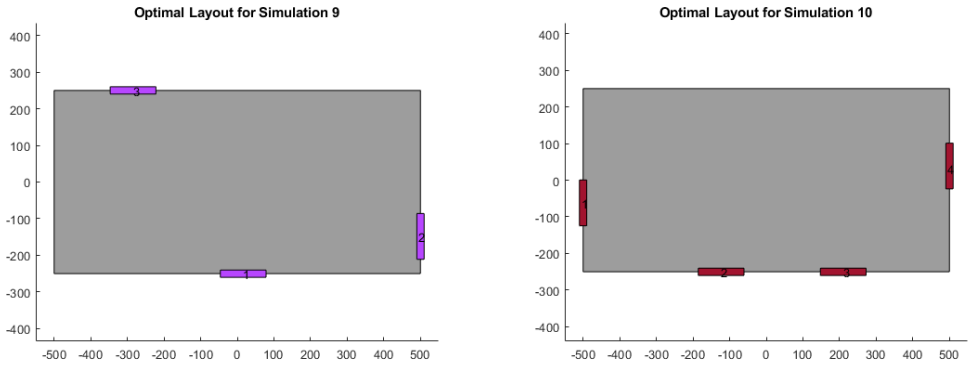

(a) Simulation 9 optimal layout (b) Simulation 10 optimal layout

Figure 6.13: 3 and 4 vice optimal layouts on 2:1 billet

layout are presented in Figures 6.14 and 6.14a. The resulting layout is of a similar nature than the one obtained in Sim 10 on the 2:1 billet. It places both bottom vices close to 300mm apart off the y central axis, and the short side vices are offset from the x centre line by a 120mm approx.

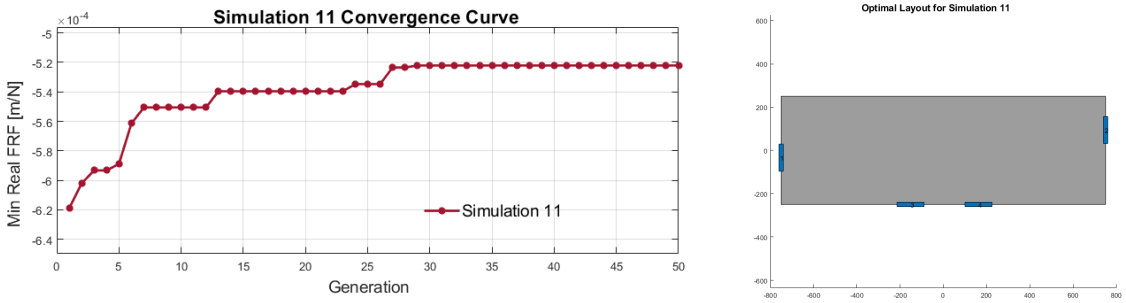

(a) Simulation 11 convergence curve (b) Sim. 11 optimal layout

Figure 6.14: Simulation 11 results on 3:1 billet ratio

6.1.4 Partly-Machined Billet

This application is makes use of the adaptability of the system to evaluate a partly-machined billet. This simulation targets an interesting potential in the optimisation system where workholding layouts can be studied at different stages within the manufacturing process. For this application, the workpiece outer dimensions are maintained at the initial size of $500 \times 700 \times 60$ mm studied in Section 6.1.1. The pocket features in the component are shown in Figure 6.15 and model arbitrary 28mm deep pocket features on both sides of the component that generate 3mm thin walls and 4mm thin floors on both sides of the billet. A mesh of the component is generated and exported

into the *inp* file format. For this case, the semi-roughed component is evaluated for external workholding layouts using 3 and 4 vices, similar to that of the receptance fitness function section.

Given that the mesh in this case has a higher node density and total count, the simulations are trialled using 20 particles and 50 generations. The resulting convergence curve is approximately asymptotic, and reaches the final value at generation 35, as seen in Figure 6.17.

The resulting layout is seen in Figure 6.16a and is an interesting departure from the previously obtained values for a three vice configuration. In this case, the system determines that opposing vices sit on the short edges, slightly offset from the centre and from each other. The third vice is placed centred on the long side opposite of the previous vice offset.

The four vice alternative also showcases an interesting result (Fig. 6.16b). Given that the 3 vice case settled on a layout that overlaps the domain for the 4 vice case, both layouts are fairly similar. The benefit of the fourth vice is therefore marginal (Fig. 6.18). This is an interesting situation where additional clamping elements does not significantly improve the response of the component, opposed to previous cases where the benefit was around 25-30%.

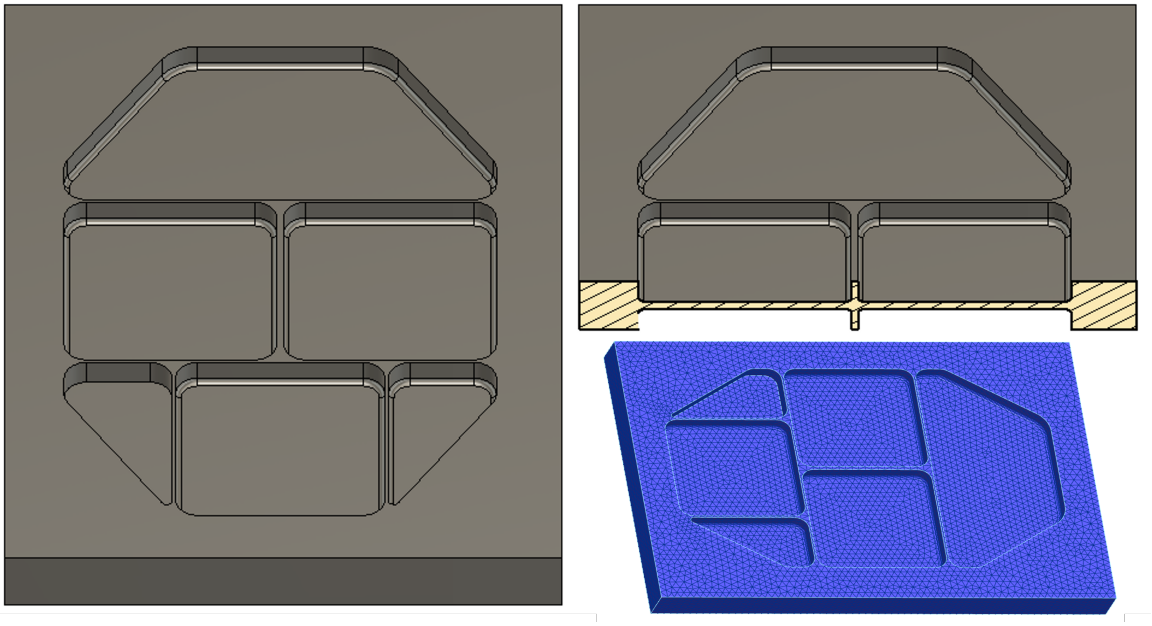

Figure 6.15: Semi roughed billet CAD and mesh

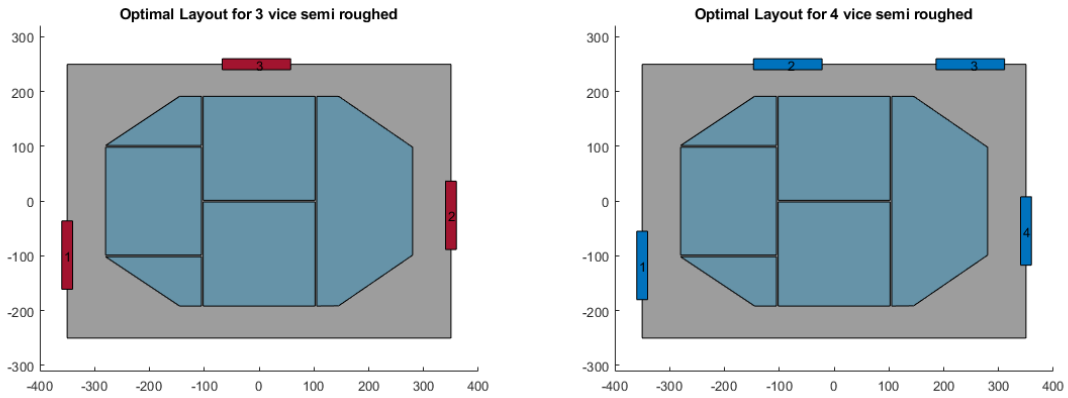

(a) SR billet three vice optimal layout (b) SR billet four vice optimal layout

Figure 6.16: Semi-roughed billet optimal layouts

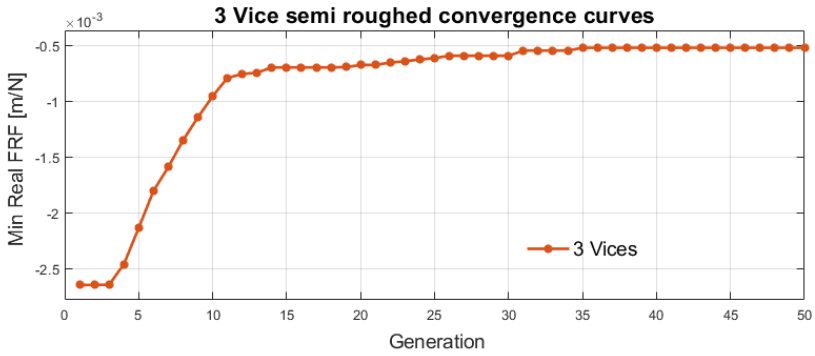

Figure 6.17: 3 vice semi roughed convergence curve

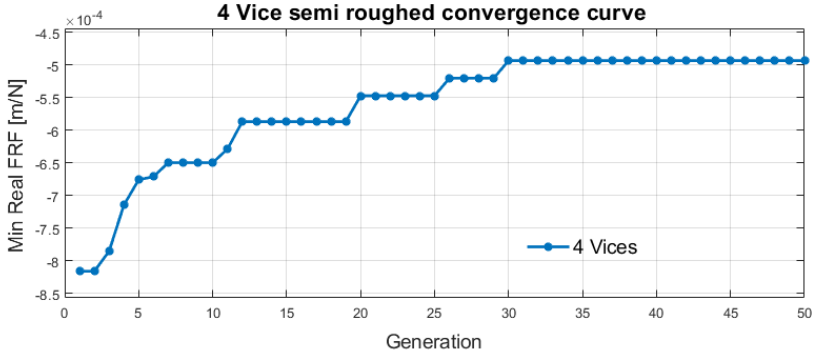

Figure 6.18: 4 vice semi roughed convergence curve

6.2 Fixture Frame Assembly Model

The previous section serves as a useful instance to troubleshoot the optimisation program and fine tune the simulations parameters for reliable convergence. The inert

behaviour of the clamps however is improved upon in this section by introducing a fixturing frame on which these vices are fastened. GKN Aerospace has previously commissioned a DSA frame to be used in its opposed spindle machining cell and it is used as a reference for modelling and experimental activities in this section.

This section has an initial purpose of enhancing the modelling capabilities for these types of workholding configurations by making use of dynamic substructuring of multi-body assemblies. Secondly, it also allows for the comparison of optimisation results between the inert clamp definition of the previous section and flexible assembled structure in this case. It also serves as an introduction for the model updating procedures and methods reviewed in Chapter 5. This section will comprise the first application of a optimisation routine based on updated modelling parameters.

The outline of activities to target these objectives is to firstly model the frame and produce a native mesh for FEA evaluation. Using this, a first model updating routine targets the welded joints present within the frame to update and validate a baseline FEA model for the frame itself. This is due to the complex behaviour of welded joints [128]. Detailed justification for this sequential updating approach is presented in Section 6.2.1.

Secondly, the PSO program is improved to include automated modelling of assembled structures, namely of the vices and billet, by use of dynamic substructuring methods. Experimental data provides a second instance of model updating, now targeting the clamping stiffness at the vice interfaces with the billet.

Finally, the validated model is used to run an optimisation program and derive the optimal placements for the clamps in this frame.

6.2.1 Physical frame model

The frame available for this analysis is presented in Figure 6.19a. It is constructed from a 50mm thick steel base plate bolted to the bases of the parallel kinematic machines. From here, two 45mm thick trapezoidal side arms are vertically welded onto the base and connected to each other using two 150x100x6mm box section beams. The overall height of the fixture is around 1.15m and weighs approximately 800kg. The trapezoidal side arms and the crossbeams have some drilled and tapped vice mounting positions, to receive a set of Schunk KSC-K125 vices.

(a) Double sided access fixturing frame (b) CAD model with weld element sets

Figure 6.19: Physical and FEA model of the DSA frame

The frame is measured and a CAD *step* file is imported into ABAQUS for meshing. Element sets are defined in the weld interfaces of each member of this structure (Figure 6.19b).

Welded joints are known to introduce dynamic discrepancy in modelling results of assembled model due to material property discontinuities within the structure[128, 129]. For this reason it is decided to firstly update the bare frame without any vices or billet attached to it. Nominal mild steel properties are selected: $\rho = 7.85$ [g/cm^3], $E = 210$ [GPa], $\nu = 0.3$.

With a initial approximation to the dynamic response of the frame, pretest analysis methods were employed to define a adequate testing configuration given the hardware availability (details in Table 3.2). Considering the mass of the structure, the accelerometers have a negligible mass loading effect and the test is defined using four triaxial accelerometers and two uniaxial. These instruments (and impact hammer) are sampled using a cRIO chassis, allowing a set of 14 signals to be extracted for each input reference. The arrangement of sensors and its resulting AUTOMAC is presented in Figure 6.20a, and showcase a adequate testing setup with adequate shape isolation, despite modes 5 and 6 present some resemblance ($\sim 30\%$). Some of the

accelerometers and cabling for this test can be seen in Figure 6.19a.

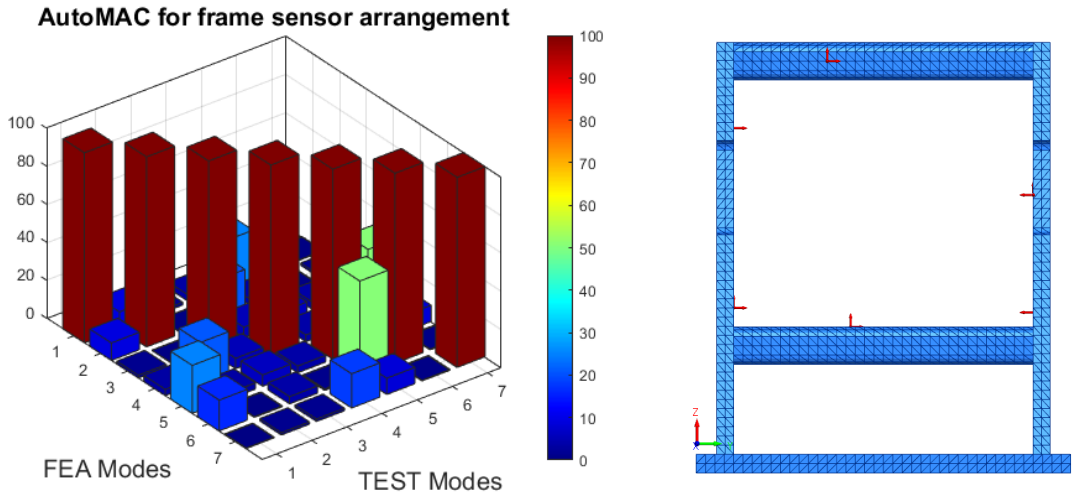

(a) Bare frame autoMAC

(b) Bare frame sensor arrangement

Figure 6.20: AutoMAC for the bare frame sensors

The structure is tapped using the impact hammer on seven different locations, yielding a broad set of cross and direct receptance FRFs. Importing these FRFs into FEMTOOLS modal parameter extraction of the experimental data correlates the nominal FEA to the experimental results. The results of this stage are presented in Figure 6.21a and the central column of Table 6.1.

Before updating, the nominal model presents an absolute average frequency estimation error of around 11.5%. With modes 1, 5 and 6 close to 20%. The shape identification seen in Figure 6.21a displays good shape identification, however diagonal matrix term for modes 4,5 and 6 present factors around 65%.

Mode	EMA [Hz]	FEA Nom. [Hz]	Δ (%)	FEA Updated [Hz]	Δ (%)
1	55.0	65.5	19.0	57.9	5.3
2	214.8	218.4	1.7	217.9	1.4
3	238.1	245.9	3.3	246.7	3.6
4	283.3	282.9	-0.1	281.1	-0.8
5	355.9	441.6	24.1	383.8	7.8
6	443.8	517.9	-19.6	600.1	-6.8
7	657.9	575.5	-12.5	626.4	-4.8

Table 6.1: Bare frame frequency estimations.

The bare frame FEA simulation is subjected to a model updating routine with an interface layer at the joint weld sets targeting local element material properties as

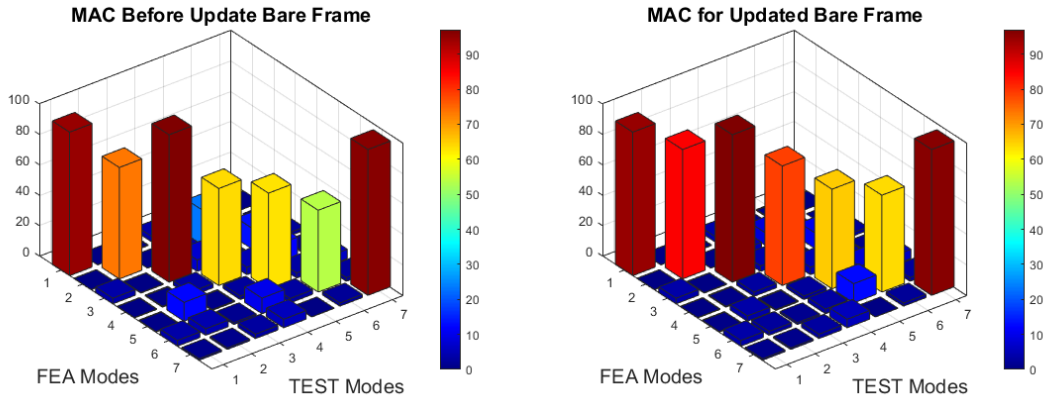

(a) MAC before updating bare frame (b) MAC after updating bare frame

Figure 6.21: Before and after updating MAC for the bare frame model

the updating parameters. Given that shape estimation is adequate, the responses are exclusively set on frequency estimation. The iterative updating yields the right hand column of Table 6.1, improving estimations to an absolute average difference of 4.4%. This consequently also improves the shape estimation slightly and raises modes 4, 5 and 6 MAC coefficients close to 70%. The first 6 mode shapes are presented in Figure 6.22.

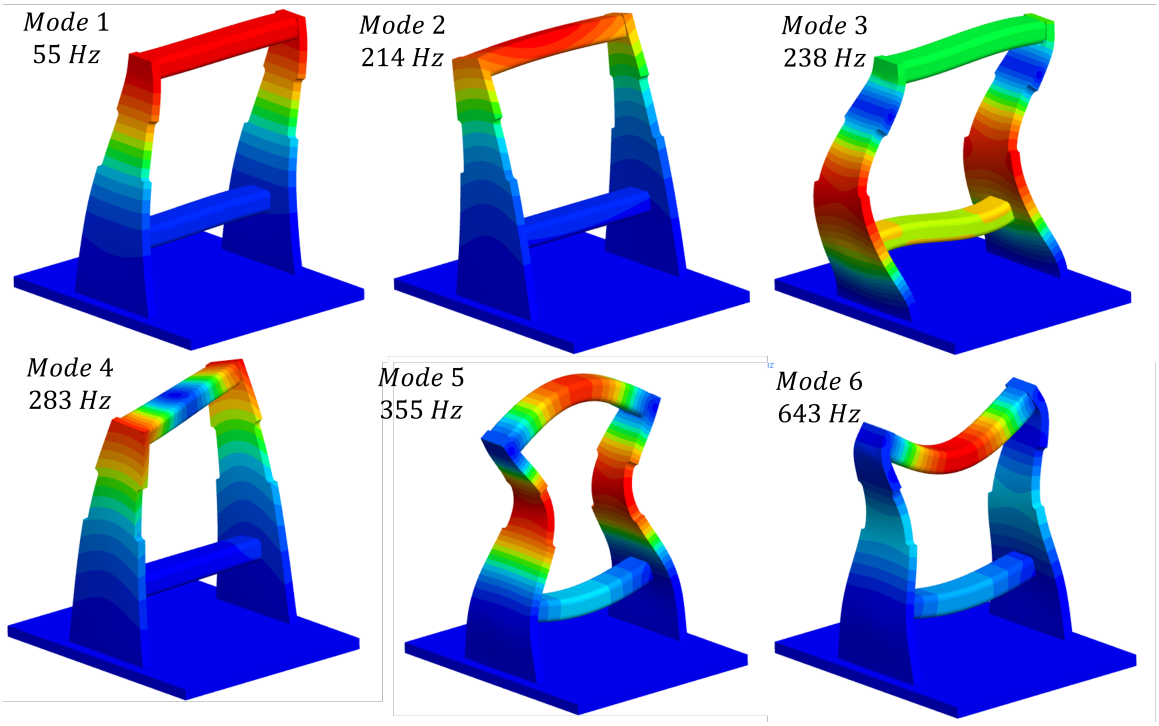

Figure 6.22: First 6 mode shapes for the bare frame

6.2.2 Assembly modelling

To model both the vices and the billet a direct meshing approach is used given the prismatic nature of the components, but more importantly to reduce the model's node count. The billet is rectangular of dimensions $640 \times 400 \times 60$ mm. The vices chosen are Schunk KSC-K125 and are modelled with a rectangular base and trapezoidal jaws. The algorithm behind the automated generation of the vices and billet follows the steps:

a) **Mesh Billet:**

   i. Define material for billet (Al 7050 card used in previous sections).

   ii. Define all 8 vertices of the billet.

   iii. Structured brick mesh of solid between vertices.

b) **Mesh Vices:**

   i. Define position of vice on the parameterised layout domain.

   ii. Transform linear domain position to physical position.

   iii. Define the 6 vertices of a face at the desired plane.

   iv. Generate surface mesh of the face.

   v. Extrude surface mesh length of the vice and convert to solid.

Direct scripting of this process in the software integration routine (Section 4.3.1) makes use of the existing framework to define and update clamping positions according to the values stemming off the PSO results.

Two methods are available to construct an assembled model of the billet, vices and DSA frame. The first is using multi-body substructuring techniques and modification/coupling elements, whilst the second is via direct meshing, merging and using the interface layer method to update the model. In both cases, the process to iteratively update layout definitions is the same.

Unfortunately, the construction of this particular model by the substructuring method is an impractical alternative due to extensive computational times required to submit each layout for dynamic analysis. The substructuring techniques average a time of 212 seconds to setup all the substructures, independently compute its dynamics and perform the assembly. Despite avoiding dynamic re-computation of the frame and

billet, a layout variation still incurs in computational times in excess of 130 seconds per layout. In comparison, the direct mesh approach merges the nodes between the vices and the frame, as well as between the frame and the billet. Computational times are significantly less, at 30 seconds on average.

In order to use the direct meshing approach, a second model updating stage targets the joint between vice and billet to validate the model. Three vices and a billet are loaded onto the frame, and an analogous model is set up in FEMTOOLS. Following the same procedure of pretest analysis, the experimental design consists of two triaxial and nine uniaxial accelerometers. Again, the mass of the structure has negligible mass loading effects and all eleven accelerometers are mounted and sampled for each test. The testing configuration is presented in Figure 6.23, with the FEA representation and the actual experimental setup in Figs. 6.23a and 6.23b respectively.

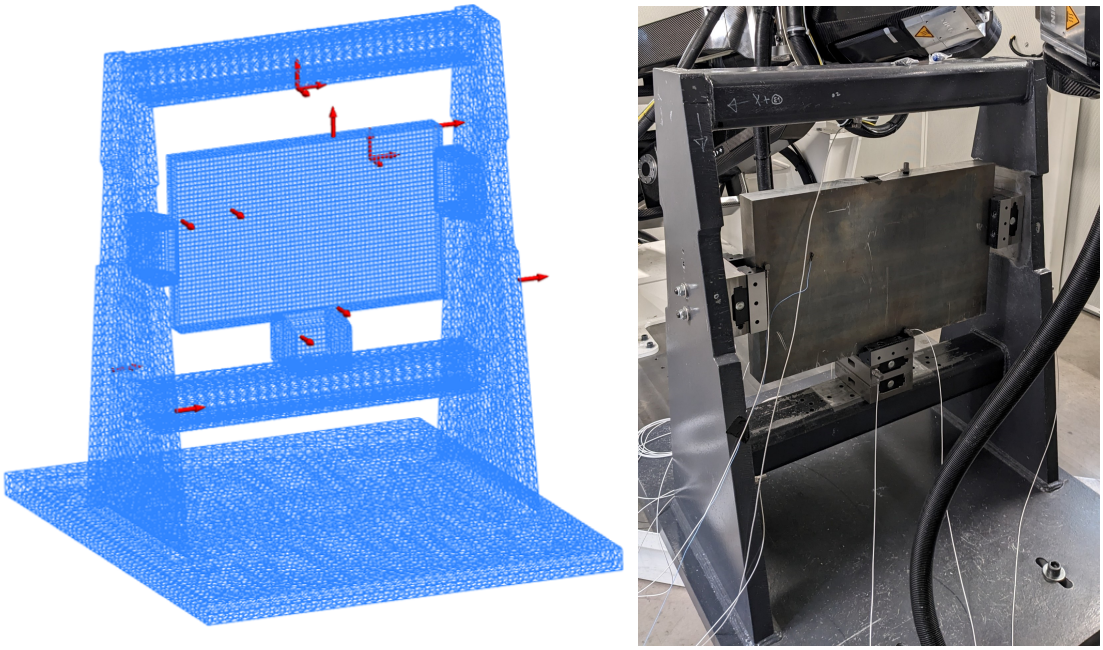

(a) Assembled model sensor configuraiton (b) Experimental setup

Figure 6.23: Modelled and physical modal analysis test

The modal testing of the assembled frame presented similar correlation levels than the previous instance for frequency estimations, but the EMA data proved difficult to pair the mode shapes to the structure and isolate each mode with certainty. Table 6.2 summarises these estimations and improvements of the model updating on the assembled structure. In this instance, a small overall improvement was a achieved, but still maintained similar discrepancies. The nominal model presents close to 5.6%

absolute difference and the updated model nearly 3.9%. Interestingly, one effect the updating had was mode one saw a reduction in its estimation in order to improve the others. Modes 3 and 4 were consistent outliers and were marginally improved in the updating routine.

Mode	EMA [Hz]	FEA Nom. [Hz]	Δ (%)	FEA Updated [Hz]	Δ (%)
1	229.2	219.6	-4.2	218.4	-4.7
2	313.7	295.5	-5.8	300.92	-4.1
3	445.3	507.7	14.0	490.14	10.1
4	504.8	559.7	10.9	552.53	9.5
5	651.6	615.4	-5.6	673.86	3.4
6	721.9	688.2	-4.7	729.36	1.0
7	751.6	733.4	-2.4	756.28	0.6
8	831.2	778.1	-6.4	822.82	-1.0

Table 6.2: Assembled frame frequency estimations

Despite these frequency estimations being around 5% error on average, the shape estimation is considerably poorer in comparison to the frequency result. Shown in Figure 6.24, a higher presence of off-diagonal terms in the MAC matrix is likely due to lower quality and noisier measured data, particularly between modes 3, 4, 5 and 6 (shapes presented in Figure 6.25). By all means higher non-linear behaviour of the structure can also skew the correlation of an intrinsically linear FEA model, but deeper non-linear system identification extends beyond the scope and capabilities at this stage.

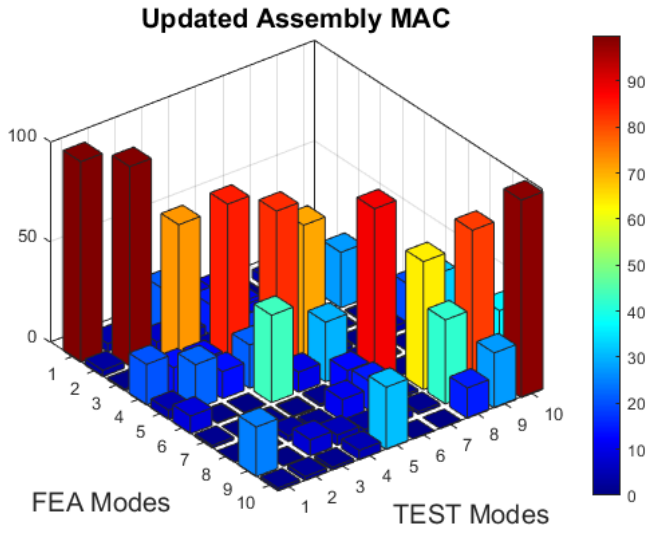

Figure 6.24: Updated assembly model MAC

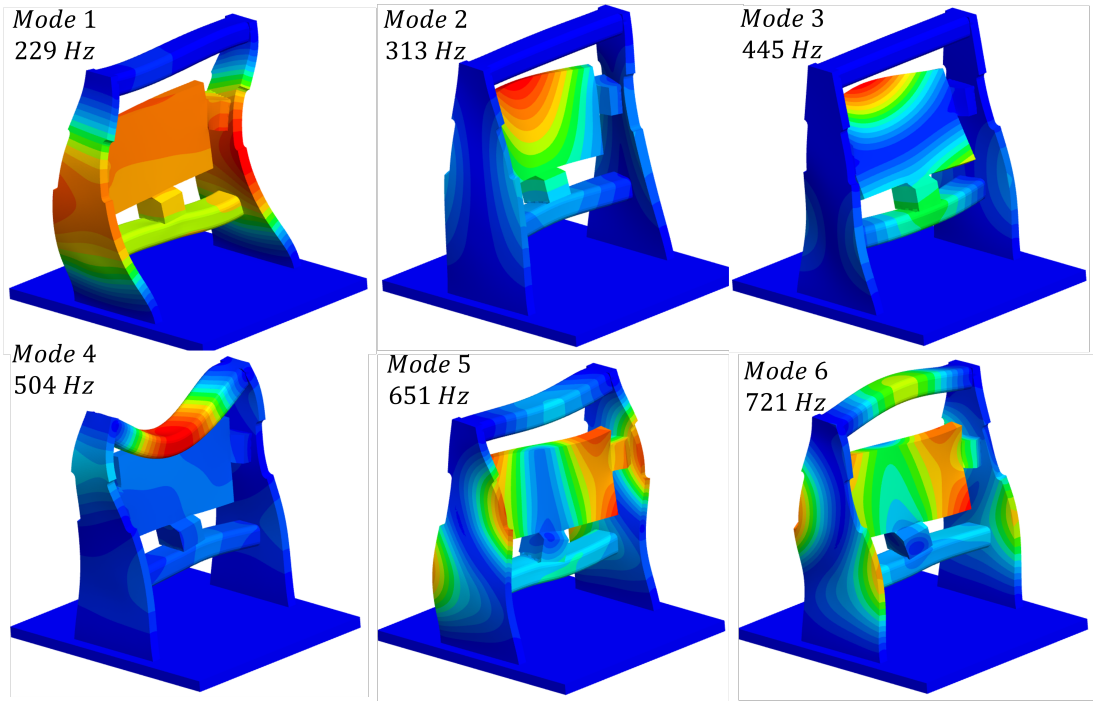

Figure 6.25: Updated assembly mode shapes

The model is progressed forward for optimisation evaluation using an exported *inp* file of the the updating results.The interface layer local element and material definition cards are isolated for each vice and scripted into the updating program for automated position adaptation.

6.2.3 Optimisation of DSA frame

Using the assembly technique and updated parameters to model the frame, vices and billet joints, the final step in this chapter is to run the optimisation routine for the assembled structure. This simulation evaluates the current setup on the frame and determines the level of improvement to the layout of the vices to enhance workpiece stability.

In this instance, three cases of the PSO are run using the physical components tested in the lab. Trialling both definitions of the fitness function, the first simulation uses the receptance approach, whilst simulations 2 and 3 use the $a_{p,crit}$ using alternative tooling configurations:

- Simulation 2 uses the 3 flute, ⌀16mm tool at 50% radial engagement (identical to previous applications of the depth of cut method).
- Simulation 3 is a 3 flute, ⌀20mm tool at 25% radial engagement (4mm).

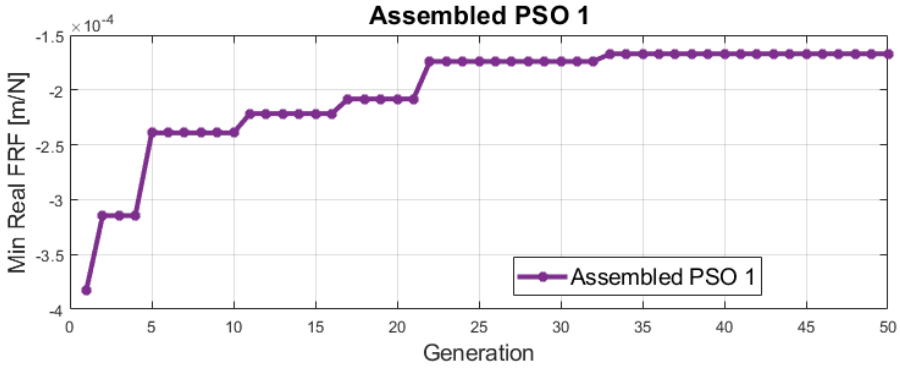

(a) Assembled PSO simulation using receptance fitness function

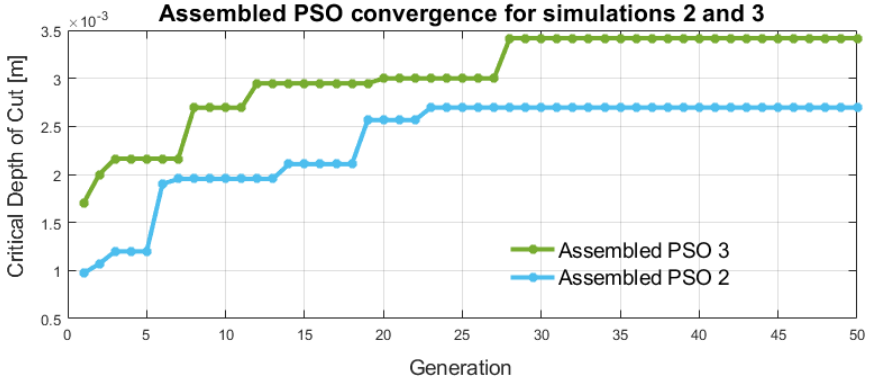

(b) Assembled PSO simulation using depth of cut fitness function

Figure 6.26: Convergence curves for the assembled model optimisations

The converging result for all the three simulations are coincidental. It is presented in Figure 6.27 and the layout locates two vices on the topmost corners of the billet and the third one 170mm off-centred on the bottom edge.

The set of convergence curves is presented in Figure 6.26. The topmost graph (Fig. 6.26a) shows the receptance approach, which converges in generation 33, whilst Figure 6.26b plots both curves of the receptance approach. Intuitively for this case, the higher immersion condition of Simulation 2, results in a lower depth of cut limit than a shallower cut with a wider tool, as Simulation 3 portrays. The billet in this case is slightly smaller than the one simulated in Section 6.1.2 and presents a $1.6:1$ aspect ratio. However, given the fact that the workpiece is mounted on a flexible frame, the resulting depths of cut are consistently lower.

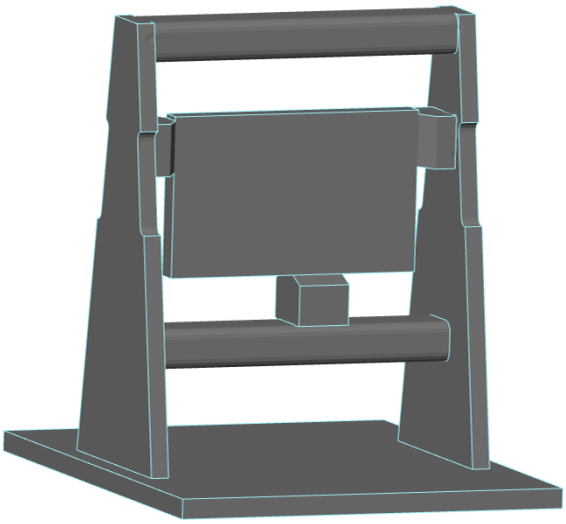

Figure 6.27: Assembled optimal layout

6.3 Summary

This chapter covers a sequential approach to the implementation of the optimisation architecture on external workholding approaches for double sided access environments. It follows a progressive increase in the complexity of the models, approaches and resemblance to industrial applications.

Section 6.1 is the training ground for the system and trials different swarm parameters to gauge performance and repeatability. It models a rectangular stock billet held by inert vice clamps around its perimeter, the contact is therefore modelled as a boundary condition. A set of direct receptance FRFs in all 3 directions are extracted from an

evaluation grid on its surface. Variations in the definition of fitness functions, aspect ratios, and machined state compose the broad set of evaluated simulations.

The second part, Section 6.2, expands the application by incorporating the fact that the inert vice assumption is a coarse simplification of joint modelling, and that DSA environments tend to require a fixture and frame to support the component. In this case, the frame is based on an existing fixture from the GKN Aerospace team, which is modelled and tested experimentally. Using two stages of model updating, an FEA assembly method is validated and employed for optimisation routines. Using both definitions of the fitness function simulations converge onto a same layout.

Table 6.3 presents a summary table with the main parameters for each simulation.

Sim.	**# Part.**	**# Gen.**	**Vices**	**Edge Res.**	**Fit. Func.**	**Size Ratio**
1	50	25	4	4	Receptance	1.4 : 1
2	50	25	4	4	Receptance	1.4 : 1
3	25	50	4	4	Receptance	1.4 : 1
4	20	40	3	-	Receptance	1.4 : 1
5	25	40	3	-	Receptance	1.4 : 1
6	25	50	3	-	$a_{p,crit}$	1.4 : 1
7	25	50	3	-	$a_{p,crit}$	1.4 : 1
8	25	50	4	4	$a_{p,crit}$	1.4 : 1
9	25	50	3	-	$a_{p,crit}$	2 : 1
10	25	50	4	4	$a_{p,crit}$	2 : 1
11	25	50	4	4	Receptance	3 : 1
SR 1	15	50	4	4	Receptance	1.4 : 1
SR 2	20	50	4	4	Receptance	1.4 : 1
Assm. 1	25	50	4	4	Receptance	1.6 : 1
Assm. 2	25	50	4	4	$a_{p,crit}$ ($\varnothing$16-50%)	1.6 : 1
Assm. 3	25	50	4	4	$a_{p,crit}$ ($\varnothing$20-25%)	1.6 : 1

Table 6.3: Summary of all PSO simulations run

6.4 Discussion

The results obtained by studying the applicability and use of the optimisation system for external workholding scenarios in DSA environments, stimulate a series of discussion points.

One of the first objectives of this chapter is to find what swarm configurations can consistently yield adequate convergence curves and repeatable results. The idea that

larger swarms would converge sooner, and require fewer generations was dismissed early on. It is preferable in this type of approach to keep the swarm size slightly lower, but most definitely increase the generation number to observe a consistent final convergence value across a good proportion of the simulation. In this case, swarms of 25 seeds on 50 generations appeared to provide suitable convergence in most applications. This result complements the first objective in Section 1.2, by improving the definition of the optimisation approach and refining successful parameters.

The applications evaluated thus far are only a reduced subset of the potential avenues of analysis this system can target. In this way, the presented results are by no means a bounding limit on the capacity of the architecture to evaluate other problems. One of the key objectives is to test the optimisation solution and trial performance and repeatability. A defining key characteristic is the adaptability to different input files and fitness functions an end user can target. In this case, clamp vices are preferably modelled, as they represent the most common workholding element available in the workshop. An interesting avenue of future research would be to expand the evaluation onto other workholding solutions, such as pins, bolts and other clamp geometries.

As stated previously, the approach used in Section 6.1 can be argued on its accuracy at modelling a DSA clamping scenario. This concept is what evokes the need for assembly modelling of a frame; the fact that external workholding in necessarily attached to either a machining bed, tombstone or frame. Nevertheless, the objective of the isolated billet section is to trial the optimisation program and troubleshoot scripting and software integration issues, rather than providing a steadfast guide for layout definition.

Despite the previous observations, a common result in all the simulations on the isolated billet section is that the layouts are seldom symmetrical across any of the major axes. In all solutions, some degree of offset is present, and vices are not commonly mirrored one from another.

One key aspect of the optimisation solution is the FRF evaluation point definition and how each model is compared to one another. For most of this chapter, the points belong to a uniform rectangular grid on the surface of the billet. This was deemed as a useful way of covering the areas where FRFs are being calculated. Nevertheless, if necessary for a particular application, the definition of the evaluation points can certainly be targeted to a specific area within the billet where a component is to be machined.

Following on the evaluation metrics between each model in an optimisation run, this chapter deliberately alternates between fitness function definitions. The receptance method offers significantly faster computational times with apparently similar results. On average, it is close to three times faster than the depth of cut method.

Another contentious point between these methods is the requirement of incorporating cutting and tooling parameters for the depth of cut metric, binding the results to a particular cutting strategy. The depth of cut method also employs the ZOA approach based on x and y direction vibration parameters on the workpiece, omitting both tool based vibrations, as well as, z direction receptance parameters. Enhancing the depth of cut prediction method could provide better estimations and make use of the lobing effect and maximise for MRR or maximum axial depth of cut. This point is critical, given that DSA environments are varied, and consequently so is their tool stiffness. Robotic milling approaches differ significantly from gantry type machines or parallel kinematics based machining centres which have been used in applications of minimal fixturing and unsupported machining this chapter targets. In order to provide competitive productivity to this type of machining approach, all efforts in reducing workpiece vibrations are useful.

An interesting application of this chapter is the partly machined component simulations of Section 6.1.4. It showcases a good example of the adaptability of the optimisation program to target, among others, stage specific workholding arrangements. Understanding that reduced workholding approaches, for residual and machining induced stress deformations for example, are beneficial aspects of a DSA environment, the capability to evaluate how workholding requirements vary from stage to stage can provide an overall improvement in the machining process by incorporating dynamic behaviour.

The optimisation of the assembled structure provided some useful insights to the applicability of the system, but can still be improved. Despite the updating model running in two stages, the overall validation can be improved by better EMA procedures. Running the update in a single stage does not improve the updated model correlation results as the amount of parameters increases with respect to the available responses. Further work is required to derive a more robust dynamic substructuring approach to model the frame interaction with the billet, and reduce the computational times against the direct mesh approach used. A possible avenue for this is to enhance the receptance coupling of the frame at different positions and potentially treat the interface as a set of boundary mDOF springs.

For the application in the following chapter, where the parting tabs of a finished double sided component are optimised, the proposal from this work is to utilise the receptance method rather than the depth of cut approach.

Chapter 7

Optimisation of Parting-off Tab Layouts

This chapter examines the application of the optimisation routine to the parting-off tabs (or breakaway ties) designed to facilitate the release of prismatic components from the stock material. In instances where not all of the billet is machined away, this remaining material serves as a frame which anchors the part using small bridge-like extensions, thus allowing the completion of all machining operations without the need for an additional setup to remove the part. The finished part can then be broken free from these ties and deburred.

While this technique is commonly employed in industry, there have been no discernible developments in the literature regarding the precise definition of the locations for these tabs. More often than not, ties are positioned based on the experience of the programmer, lacking a specific method other than the use of recognisable geometrical features proven useful in similar components.

The critical nature of these features lies in the fact that they are implemented towards the end of the machining process, following numerous hours of machine time. Consequently, any damages or non-conformance rising at this stage would result in scrapping nearly finished parts, with little room for remedial work. Breakaway tie generation often also involves a finishing pass on outer faces of the component, requiring a balance between sufficient support for the machining operation while also enabling manual removal of the finished part. Achieving these conflicting requirements poses a considerable challenge.

The optimisation method developed thus far can be applied to this type of feature, as

they fundamentally represent the same type of problem. What was initially designed for external workholding features on a billet can now be reconfigured to focus on internal features between the component and the unmachined stock material.

The objective of this chapter is to measure the improvements an optimised tab layout can have on the stability of a finishing pass against a common practice approach where no dynamic metrics are used. On the FEA modelling front, the main objective is to provide the PSO program with further versatility and areas of application. This chapter presents a novel approach to characterising breakaway ties and its associated meshing routines to derive optimal layouts.

The chapter is divided into three main sections, which describe the physical test vehicle used for machining trials, the FEA, EMA and PSO adaptations to evaluate this setup, and the results of different simulations with alternative user defined variables.

7.1 Evaluated Setup

The test artefact used to test the optimisation is presented in figure Fig. 7.1. The

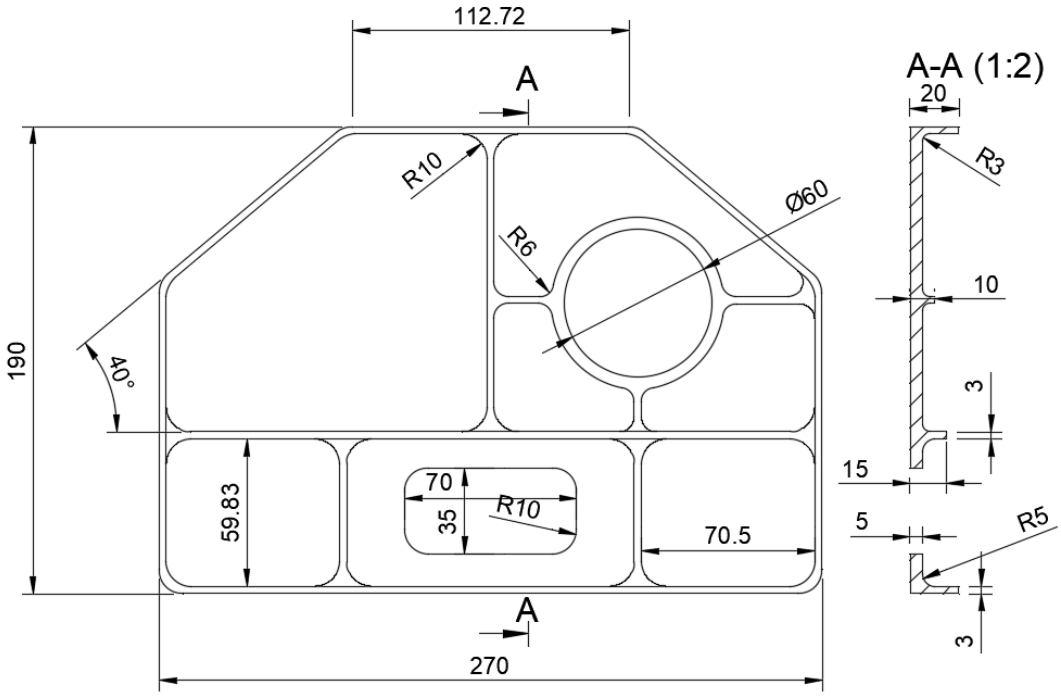

Figure 7.1: Drawing of tab optimisation test vehicle

component is designed with non-symmetric features to avoid the presence of repeated

modes and multiple maxima in the search space. It is based on components of similar scale produced by GKN in the past, including key features such as through holes, thin walls and thin floors, as well different wall heights and edge transition radii. The aim is to provide the test vehicle with representative features commonly found in prismatic double-sided components.

The available tooling is defined in Table 7.1 and the image of Fig. 7.2 displays them in the same order.

Tool ID	**Diameter [mm]**	**Nose Rad** [mm]	**# Flutes**	**Make**
20mm endmill	20	5	3	Walter Tools
12mm finish	12	3	5	Kennametal
12mm serrated	12	3	3	SGS Kyocera
10mm finish	10	0.2	4	SGS Kyocera

Table 7.1: Tooling details

Figure 7.2: Built tools. Left to right: 20mm, 12mm finish, 12mm serrated, 10mm finish

7.1.1 Machining Process

The component is machined from a Al-7050 billet of dimensions 400 × 360 × 60 mm on a Heller HF3500, a table-table 5 axis machining centre, and follows a three

stage method of manufacturing. The CAM package used to program the tool paths is Autodesk Fusion360. The images depicting the evolution of material removal in Figs. 7.3 to 7.5 show the billet and unmachined surfaces in blue, whilst the finish component geometry is highlighted in green. The material removal sequence is as follows:

- Stage 0:
  - Blank billet has been previously squared, drilled and counterbored to receive M12 fasteners following the machine's bed bolting pattern.
  - Tools are built, measured on Zoller pre-setter and loaded onto the machine.
  - Billet is loaded and work coordinate system probed in according to the CAM program G54 definition; on the centre of top surface.
- Stage 1:
  - Facing of billet to 58mm thickness.
  - Pocketing of component bottom face using a trochoidal waterline approach at 12mm maximum axial depth of cut, 8mm radial depth of cut and 0.15mm/tooth feed rate. A 0.2mm axial depth of cut finishing pass is machined as well. The contour has a positive radial offset of 16mm and an axial recess of 28mm from the top surface to situate the component in the centre of the billet and allow radial relief for subsequent slotting operations.
  - Stage 1 is machined with the 20mm endmill, with a CAM preview in Fig. 7.3

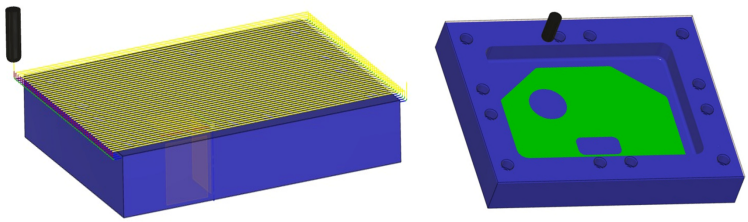

Figure 7.3: Stage 1 CAM

- Stage 2:
  - Flip billet. Probing of G55 to overlay on previous G54 (i.e. on centre of bottom face).

- Waterline approach to generate internal pockets at 5mm depths. Machined with the 20mm endmill and 12mm finish endmill where required.
- Through holes are bored out with 20mm endmill in a trochoidal path.
- Floors and webs are finished.
- Progressive operations as illustrated in Fig. 7.4

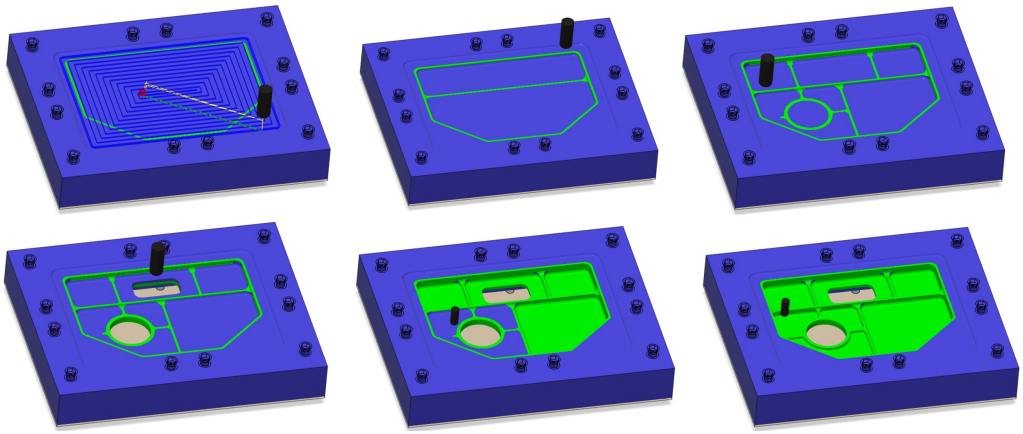

Figure 7.4: Stage 2 CAM sequential operations

- Stage 3:
  - Helical slotting of outer wall and tab preform generation. Milled with a 1° helical slope at maximum 2mm axial depth of cut, using 12mm ripper endmill at 0.075mm/tooth feed rate.
  - Tab cleanup to ensure square mating surface with 10mm finishing endmill. Discussed in section Section 7.3.1.
  - Full axial finishing pass on outer wall at 0.15mm radial engagement and 0.05mm/tooth feed rate using 10mm finishing endmill.

7.2 Tab modelling and PSO adaptation

The optimisation system programmed for the previous applications requires some adaptation to work on internal features of the *inp* file mesh. Nevertheless, the approach is similar: parameterisation of the outer border onto a single dimension search space, populating the the swarm particles and iterative evaluation of each generation.

In this case, in order to accurately represent a tab on the outer edge of the part some mesh manipulation and FEA methods must be employed. Three main approaches

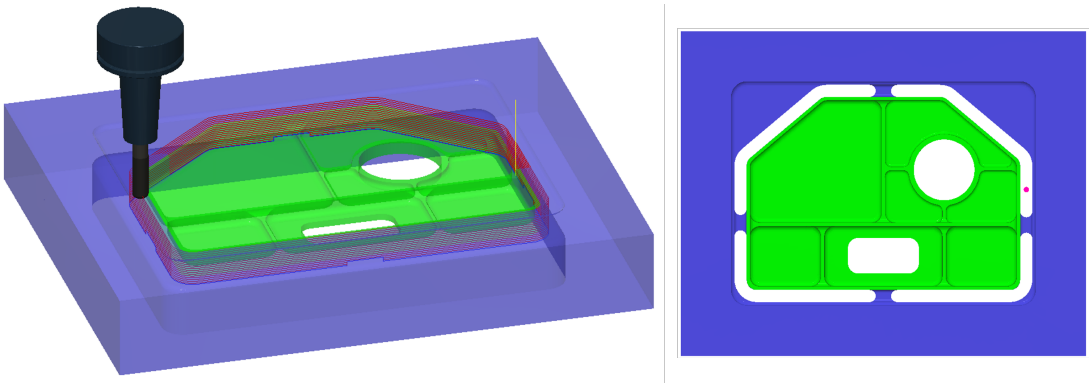

Figure 7.5: Stage 3 CAM, representing arbitrary layout of 4 tabs

are initially screened to derive the most suitable way of modelling a set of tabs on the part. The comparison in performance for each alternative, is measured against a benchmark layout and model that all three methods must emulate. Details of all modelling methods, including the baseline model are described in the following sections.

7.2.1 Baseline Model

The reference level to compare these three methods is defined using a structured meshed model (built using an adaptive bottom-up approach) that includes the tabs and local mesh refinement to ensure adequate mesh quality metrics. This model was subjected to close inspection and compared FEMTOOLS, ABAQUS and Autodesk Fusion360 simulation environments. The first two simulations shared the same *inp* file mesh, whilst the Fusion 360 model generated its own adaptive meshing routine and dynamic solver. Despite the differences in simulation environments, all three instances of the baseline mode coincided to within 0.2% absolute frequency difference. This particular modelling approach is treated as the baseline reference due to the fact that the protocol followed is expected to provide the most accurate result for a non-validated FE approximation. However, due to the intensive meshing procedure required to build the model, this modelling method is not suitable for automation within the optimisation program.

The representative mesh is presented in Fig. 7.6a, and the first ten mode frequencies are listed in the first row of Table 7.3. Upon inspection of the mode shapes, three discernible quasi-rigid body modes (or suspension modes) for the semi-finished component are identified under the 100[Hz] band. These correspond to the 3 out-of-plane modes, which in this coordinate system correspond to TZ, RX and RY (Figure 7.6b).

They are considered to be *quasi-rigid* modes, given that the tabs still influence higher order modes and are a structural part of the component. This arrangement, therefore, does not fully establish a suspension that exhibits strict definition of pure rigid modes, presented in Section 3.1. The fully flexible (or elastic) modes exhibited by the component are observable around 500[Hz] and over.

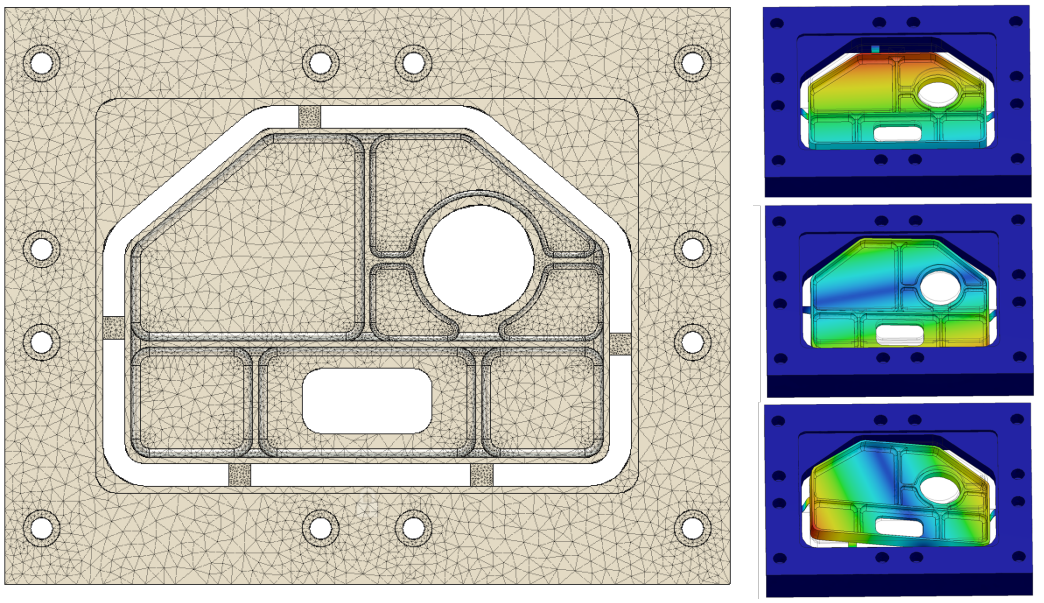

(a) Baseline mesh and tab layout

(b) 'Rigid' body modes

Figure 7.6: Mesh and mode estimation for the baseline model

From a software integration perspective, this method is technically feasible to automate at a significant computational cost. Although Fusion 360 can be scripted into modifying the parametric model of the part and adjust to the PSO definition for each layout, meshing the part can either be done internally in the Fusion Simulation environment or scripted into ABAQUS. The internal Fusion360 environment works off cloud servers and require significant amount of time to provide a solution; in the range of 5 to 6 minutes for this component. Then a *vtu* mesh format must be translated into an *inp* file for FEMTOOLS to perform dynamic computation and FRF computation. The ABAQUS route would take a *step* file from Fusion360 and import it for structured bottom-up meshing and subsequent *inp* file generation. This alternative would also require mesh quality controls and local refinements subroutines amounting to similar lead times per layout. For these reasons, automating this modelling approach within the optimisation program is not considered at this stage.

7.2.2 Direct Node and Element Generation

This method consists of directly meshing the tabs in order to join the component and billet. The native mesh is composed of two disconnected parts corresponding to the component and the billet. Local mesh refinement is performed on the component mesh and interest area of tab placements, as seen in Figure 7.7a.

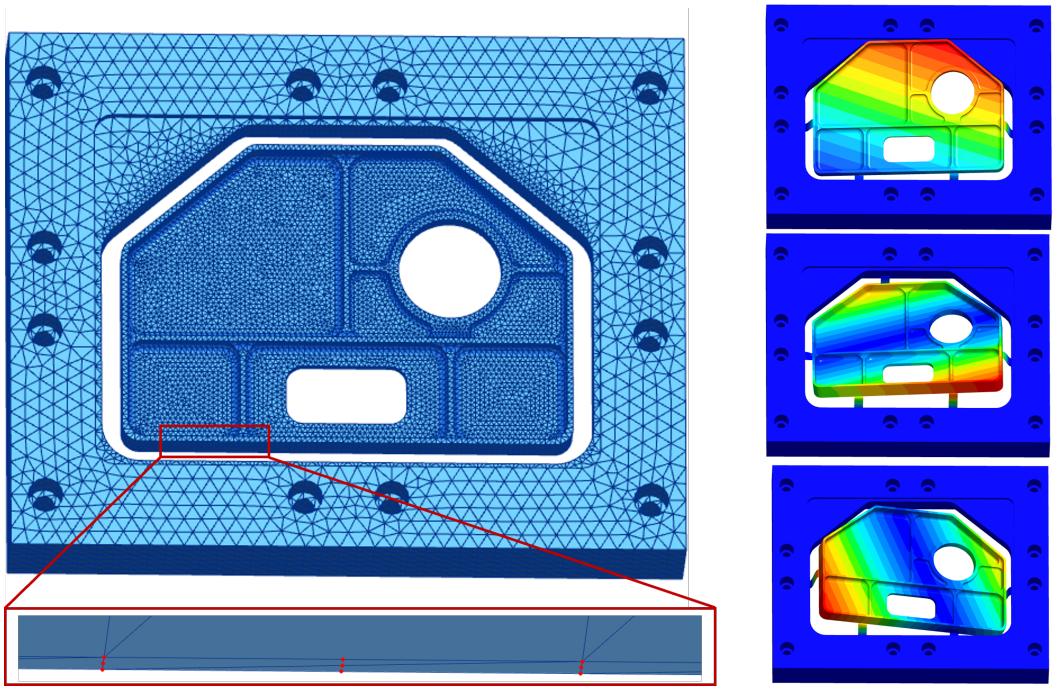

(a) Direct Meshing native mesh

(b) 'Rigid' body modes

Figure 7.7: Mesh and mode estimation for the direct meshing model

The placement of the tabs to each selected position, is done by finding opposing corner nodes of the component and billet, and then interpolating nodes and elements between them. This mesh generation procedure then generates a direct rectangular mesh for each tab using the same material and geometrical properties of the native mesh. Elements are generated at 1mm spacing, merged between both native meshes and prompted into dynamic computation.

Frequency estimation results are listed in Table 7.3 and present an average difference of 4% in the first 10 modes. The main deviation is in the first 3 quasi-rigid body modes, which despite exhibiting the same mode shapes (Figure 7.7b), frequency estimation differences rise to nearly 20%.

Despite having results within an acceptable range of estimation, from a computational

time perspective, this method incurs in significant simulation times. Given that each tab takes approximately 8 seconds to generate before dynamic computation begins, this overall increase in computational time is close to 20%, including the dynamic solving and file export.

7.2.3 Mesh Activation and Deactivation

Mesh activation methods are common for adaptation of FEA simulations. They makes use of a global mesh whose elements are activated or deactivated following a set of certain rules or criteria. Common applications are in areas such as residual stress and deformation modelling in additive manufacturing [130, 131] or machining induced stresses [132]. An adaptation of this method was also used by GKN to evaluate the evolution in dynamic response of the single pocket coupon in mentioned in section 5.1.

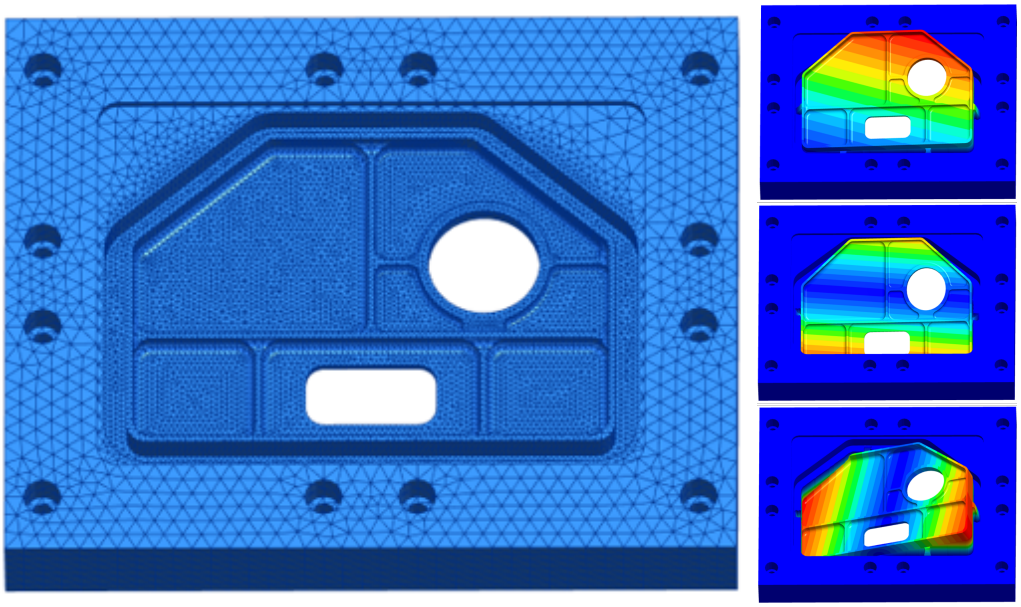

(a) Direct Meshing native mesh

(b) 'Rigid' body modes

Figure 7.8: Mesh and mode estimation for the activation model

In this case, a thin mesh completely spans the potential tab locations and is activated or deactivated as needed (Figure 7.8a). When the PSO program prompts the requirement for a tab in a specific location, the corresponding region activates to indicate material presence and simulate a tab. No mesh merging or new element creation is required, only the activation of elements within the tab's bounding box. However, this approach has its limitations. Despite providing a refined mesh in the brim area,

the mesh's spatial resolution will limit the capability to model each tab precisely. Firstly, uneven edges and overall jagged geometries can be observed for each tab, but more importantly, the spatial resolution imposes a limit on the minimum tab width differences and sensitivity it can compute. Consequently, variations in width close to this resolution may not be accurately represented and resulting in undersized tabs. A graphic example is presented in Figure 7.9.

In spite of these potential shortcomings, the method is tested against the benchmark FEA layout and exhibits a similar set of results with an overall mismatch in frequency estimation of about 11%. Although it does exhibit the same three quasi-rigid body modes (Figure 7.8b), frequencies are significantly underestimated, which could be explained by undersized tabs.

A positive outcome of the method is that no significant additional computational time or resources are required over the dynamic evaluation of a layout, however to overcome the aforementioned limitations with finer meshes would necessarily result in longer simulation times.

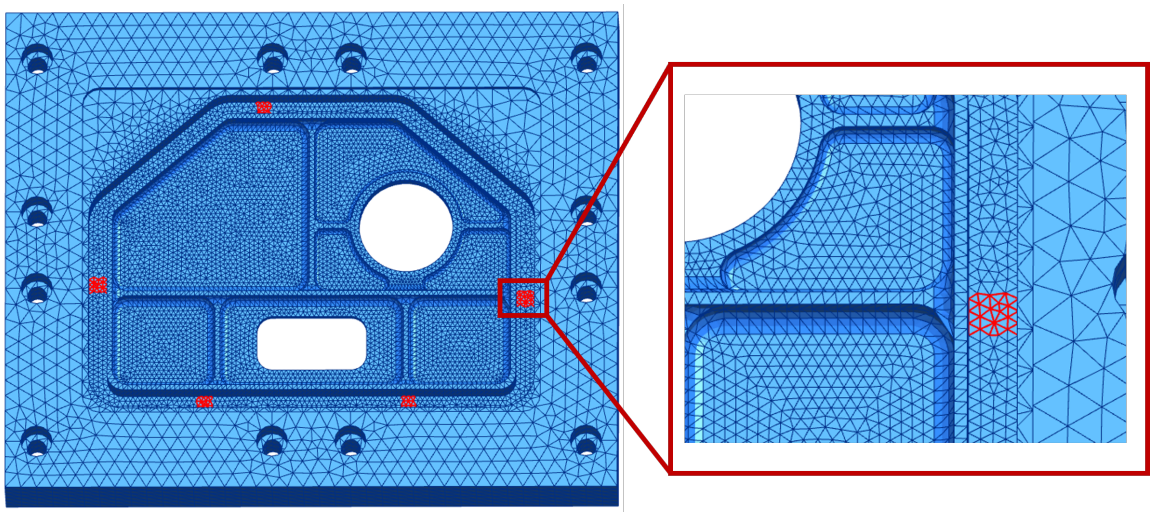

Figure 7.9: Detail of tab generation with a deactivation method

7.2.4 6-DOF Spring Method

The 6DOF spring method is similar to that used in section 5.3.3. In this case, each tab is modelled as a set of 6DOF springs on a group of nodes taken from the edge of the component. The main argument to support the implementation of this approach is the apparent presence of out of plane quasi-rigid body modes at lower frequencies than local elastic modes, which can be easily targeted via spring-based boundary

conditions. Careful definition of each directional stiffness is required, but this method has significant computational time benefits if correct implementation is achieved. There is also the benefit of omitting the billet and frame mesh, considerably lowering the node and element count in the model.

This method is evaluated in two stages; using only nominal stiffness values from beam theory, and then updating the spring parameters using the baseline model as a target. Given that the baseline is designed using completely rectangular tab, implying both constant cross section and constant thickness, classic beam theory can be used to calculate the 6DOF stiffness values. The translational stiffness values are calculated using Equations (7.1a) and (7.1b) and the torsional stiffness using Equation (7.1c). These definitions are based on a local coordinate system to the tab and are therefore independent of the orientation they take around the part (Fig. 7.10). This localised definition is implemented in the model by defining the normal directions at each node within the edge of the part.

$$k_{ti} = \frac{3EI_{ii}}{T_L^3}, \quad i = [x, y] \tag{7.1a}$$

$$k_{tz} = \frac{EA}{T_L} \tag{7.1b}$$

$$k_{rot} = \frac{E\beta H_t W_t^3}{2T_L(1+\nu)} \tag{7.1c}$$

For these equations, E is elastic modulus, I_{ii} is the second moment of area, L_t, H_t, W_t are the tab's length, height and width respectively, A is the cross section, β is the torsional constant factor for rectangular beams and ν is the Poisson modulus used for relating the shear modulus to the elastic modulus.

Using the numerical values of the baseline model for the tab, where $L_t = 12, H_t = 0.2, W_t = 12$ (units of which are SI(mm) specified in Table 3.1). The resulting stiffness values are obtained:

$k_{tx} =$	$2.34 \cdot 10^{-1}$	N/mm
$k_{ty} =$	$5.39 \cdot 10^{2}$	N/mm
$k_{tz} =$	$2.15 \cdot 10^{3}$	N/mm
$k_{rx} =$	$3.46 \cdot 10^{8}$	N·mm/rad
$k_{rx} =$	$1.54 \cdot 10^{2}$	N·mm/rad
$k_{rx} =$	$1.54 \cdot 10^{2}$	N·mm/rad

Table 7.2: Nominal stiffness for 6DOF spring

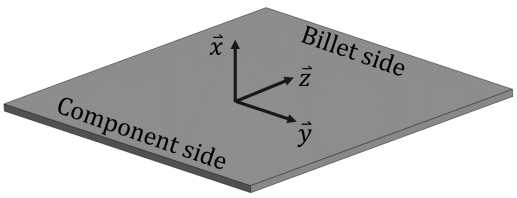

Figure 7.10: Internal tab orientation

With these stiffness values, a set of nodes spanning the width of the tab are selected from the edge of the component. Each value is divided in the number of nodes per each tab to ensure that the estimated stiffness is consistent despite potential discrepancies rising from the spatial resolution and tolerance.

Dynamic evaluation yields a good frequency and mode shape estimation when compared to the baseline model, averaging a 2.6% frequency difference (Table 7.3) with the same type of shapes. Additionally, there is a significant improvement in the computational time, reducing the baseline modelling times from 40 seconds down to 19. Further benefits to this method are targeting each stiffness value as updating parameters. Using the baseline model as a test mesh and the 6DOF as a FEM model, direct correlation metrics can be implemented. This allows to set frequency and MAC coefficients as a target responses for model updating (Section 3.4). The updated results of the spring method are presented in the last row of Table 7.3 and show a significant improvement against the other methods. Frequencies were estimated with a 0.9% difference, on average, with a maximum deviation of 2% on mode 1. Variations in stiffness parameters were observed within the $\pm 0.6\%$ range for torsional stiffness and within the $\pm 15\%$ range for translation values, except for k_{tx}, which increased by 48% to $3.46 \cdot 10^{-1} N/mm$. This latter value corresponds to the out-of-plane direction stiffness and is therefore the most sensitive parameter to the first 3 modes responses. The updating also resulted in minimal influence from the torsional modes. Modelling the component with only translational springs at the updated values yields identical results in both frequency and shape estimation, offering even further simplifications to the model.

7.2.5 Tab Modelling Summary

In the previous sections, the performance of different modelling approaches to target tab generation was compared against a baseline FEA model. Each approach was screened for natural frequency estimations as well as computational times and automation capabilities. Table 7.3 presents the baseline estimations for natural frequency up to mode 10 in the topmost rows, and is used to quantify errors from the other methods. The graph in Figure 7.12 aids the visualisation of these results.

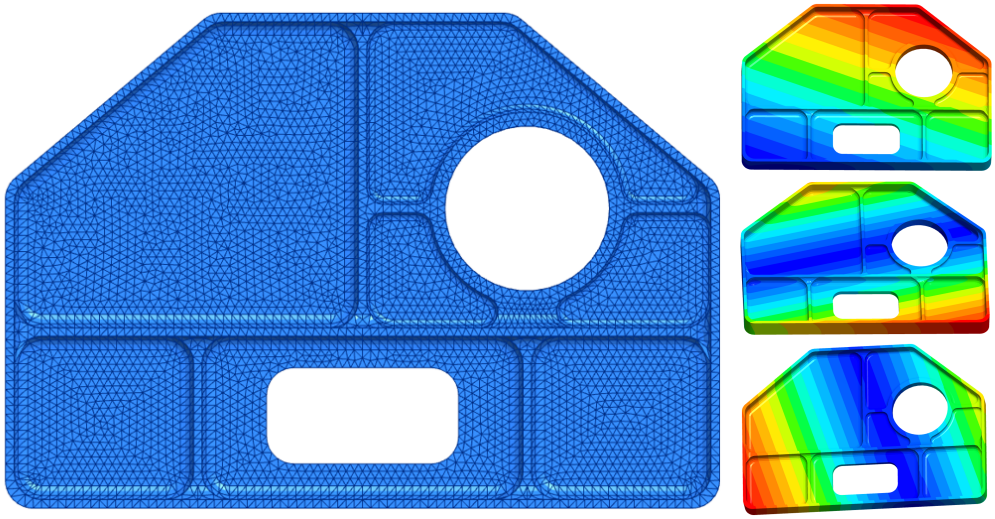

(a) Spring BC mesh (b) 'Rigid' body modes

Figure 7.11: Mesh and mode estimation for the spring BC model

Model	Mode / Baseline [Hz]	1 **48.2**	2 **67.4**	3 **87.4**	4 **510.6**	5 **771.5**	6 **1033.7**	7 **1078.2**	8 **1253.1**	9 **1353.7**	10 **1548.2**	**Mean Dif.**
Direct	f_n [Hz]	45.0	62.1	70.0	506.3	768.6	1030.8	1092.4	1267.7	1370.2	1545.1	
Meshing	Dif. [%]	6.6	7.9	19.9	0.8	0.4	0.3	1.3	1.2	1.2	0.2	4.0%
Mesh	f_n [Hz]	41.4	55.4	62.3	499.3	762.3	885.7	1016.1	1053.8	1146.3	1534.7	
Activation	Dif. [%]	14.1	17.9	28.7	2.2	1.2	14.3	5.8	15.9	15.3	0.9	11.6%
6dof	f_n [Hz]	45.7	71.6	83.3	519.7	778.8	1027.6	1115.4	1248.3	1371.1	1573.6	
Spring	Dif. [%]	5.2	6.2	4.7	1.8	1.0	0.6	3.5	0.4	1.3	1.6	2.6%
6dof	f_n [Hz]	47.3	66.8	88.4	507.3	775.2	1031.3	1082.2	1248.3	1371.1	1573.6	
Updated	Dif. [%]	1.9	0.9	1.1	0.6	0.5	0.2	0.4	0.4	1.3	1.6	0.9%

Table 7.3: Tab modelling method comparison of natural frequency estimations

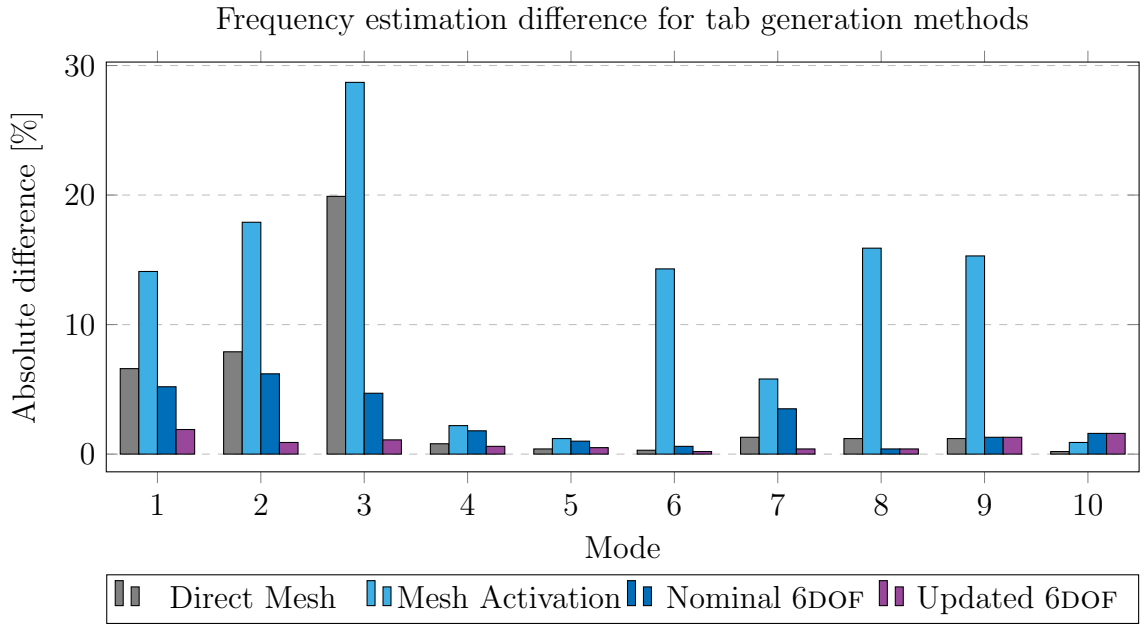

Figure 7.12: Frequency estimation difference for tab generation methods

From all the evaluated alternatives, the mesh activation method produced the largest frequency discrepancies. While the direct meshing approach was potentially adequate, it presents significant computational times. Finally, the 6DOF method reveals considerable benefits over the previous two methods. It provides closer estimations to the baseline model, halves the computation time per layout, and more importantly, it allows for reliable and efficient updating on the physical constants of the spring elements. These results suggest that the 6DOF method is the most practical approach for PSO implementation.

7.3 Machining Trials

In order to test the validity of this approach and further improve the capabilities of the optimisation program, a set of machining trials were conducted. The aims of these experimental activities are to firstly quantify a potential improvement an optimised layout can provide when compared to a common practice (and non-optimised) approach. Secondly by applying the EMA methods on the non-optimised component, it will allow for model updating of the tab parameters. These validated results are then be implemented in the optimisation routine to derive an optimal layout. An interesting discussion can be found by reviewing the extrapolation behaviour of updated results compared against the EMA data of the optimised layout. Finally, making

use of this optimisation development, a series of complementary tab layouts are run maintaining the total tab length, but varying the amount of tabs.

7.3.1 Non-Optimised Component

A brief set of common industrial guidelines for tab placement decisions are as follows. Where possible:

- Place tabs on straight edges, preferably opposing.
- Overlap on face should nominally be 0.15mm (tab height).
- Tab width should be under 25mm.
- Slotting of tab channel is performed with square endmill (0.2mm nose rad.).
- Anchor tabs as close as possible to fixturing elements (bolts, vices, clamps).

Based on this, the non-optimised layout is presented in Fig. 7.13 and is composed of four 15mm tabs located at the top and bottom edges symmetrically distanced from the centre line.

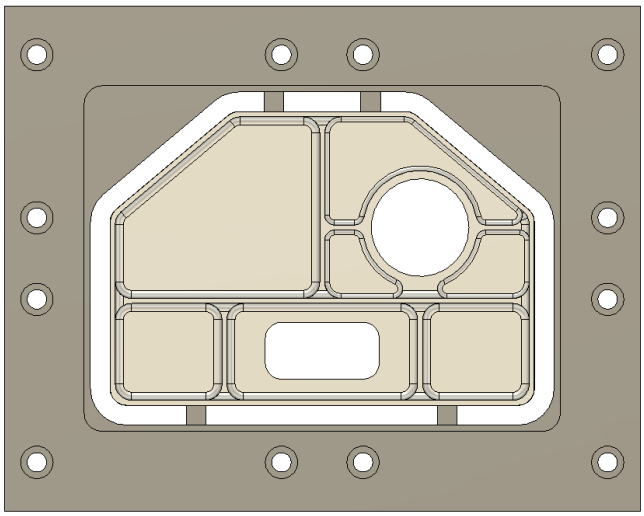

Figure 7.13: Non-optimised test vehicle

One deviation this part has from the guidelines is the slotting operation, where common practice would machine this section with a square (or flat) endmill. In this case, the slot is machined with a bull nose 12mm ripper endmill with a 3mm nose radius. To avoid leaving a fillet between the component and the tab (see Fig. 7.14) a clean up operation skims the top section of each tab. This is done to avoid running a

sharp endmill in a potentially unstable workpiece and risking a catastrophic failure of the tool and/or part. This also allows for a more consistent finishing pass, as the wall maintains a uniform stock width and avoids sudden increases in radial and axial engagements of the cutter at the tab locations.

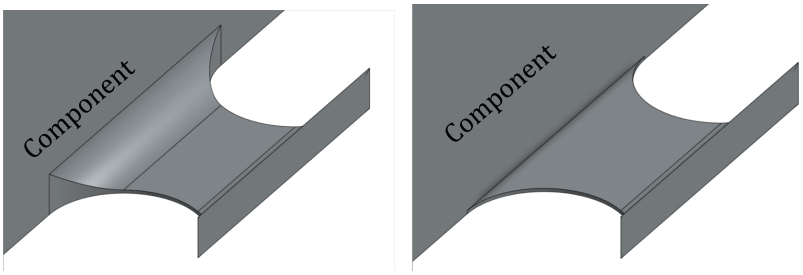

Figure 7.14: Tab clean up operation

7.3.2 EMA and Model Updating of Tab Parameters

The first step to extract the EMA data from the non-optimised component is to derive the most adequate positions for sensors and excitations. Following the method defined in Section 3.3.1 and using mode participation analysis a roving hammer test protocol was defined. Figure 7.15 shows the semi-finished non-optimised component with some marker dots showing tapping and sensor placements. The test is comprised of 5 excitation locations and 9 sensor locations.

Figure 7.15: Non-optimised machined component

Once the tap tests were performed, FRFdata was translated to *uff* format and imported to FEMTOOLS for correlation. The initial model was simulated with nominal stiffness values for a rectangular tab, as per Table 7.2. It presents good mode shape correlation to that of the EMA data, with modes 1 to 9 of the MAC matrix in the range of 70 to 99.6%, however mode 10 has a drop to 54%. The natural frequency estimations presented a considerably less accurate (Table 7.4) result. All modes exhibit an underestimation of frequencies, averaging close to 10% difference, with modes 2 and 3 slightly over 25%.

Before running the update, careful measurements of the thickness of the tabs is required to double check whether the physical component machined the tabs at 0.15mm thickness. Despite being a complicated feature to measure on the part, due to the size of the channel compared to that of the micrometer, the tabs presented a slight oversize to an average thickness of 0.187mm versus a nominal of 0.15mm. This is consistent with the frequencies being higher than expected, as a thicker tab will present a higher stiffness and consequently a higher frequency. Even if 37 microns is usually well within machining tolerances, particularly for non critical or even auxiliary features in the part, in this case the deviation presents a considerable proportion of the overall thickness of the tab. Remedial thinning of the tab by means of a tool length offset was not pursued at this stage, due to the risk of ejecting the part and potential damages to the machining centre.

Mode	EMA	FEA Nominal	Δ (%)	FEA Updated	Δ (%)
1	76.7	69.2	-9.7	77.4	1.0
2	125.8	94.1	-25.2	128.9	2.4
3	221.6	164.3	-25.9	219.6	-0.9
4	480.8	458.0	-4.7	472.1	-1.8
5	713.1	701.4	-1.6	711.0	-0.3
6	991.8	943.2	-4.9	957.1	-3.5
7	1358.8	1117.4	-17.8	1341.1	-1.3
8	1425.9	1413.5	-0.9	1442.0	1.1
9	1535.2	1461.7	-4.8	1484.1	-3.3
10	1799.7	1574.7	-12.5	1728.3	-4.0
k_{tx}	N/mm	$2.34 \cdot 10^{-1}$		$3.83 \cdot 10^{-1}$	63.9
k_{ty}	N/mm	$5.39 \cdot 10^{2}$		$5.69 \cdot 10^{2}$	5.5
k_{tz}	N/mm	$2.15 \cdot 10^{3}$		$2.35 \cdot 10^{3}$	9.4

Table 7.4: Non-optimised natural frequency estimations

Despite the variation in thickness, the tabs' stiffness was updated using natural fre-

quency estimations as the parameters (Section 3.4). MAC coefficients were adequate to start with, but were still improved upon as a result, with mode 10 correlation rising to 57% and all other modes over 73% (Fig. 7.16) . In contrast, the natural frequency estimations were significantly improved. The average estimation difference fell from over 10% to 1.1%. Particularly, modes 2 and 3, had a reassuring maximum difference of 2.4% and 0.9% respectively.

The most significant result of the updating routine is the disproportionate increase in the out-of-plane stiffness, rising almost to 64%. Adding to the fact discussed previously of the physical tabs being slightly oversised, another reason behind this increase is potentially due to the discrepancy between the physical geometry of the tab and the nominal modelled version. Despite the cleaning the nose radius blend on the component side (Fig. 7.14) the blend is kept on the billet side. Alongside this, the tab itself is not perfectly rectangular and actually has semicircle edges, adding width at both ends of the tab, which also explain the lesser increases in the in-plane stiffness values. Regardless of the variation between modelled and physical geometry of the tab, the versatility of the updating procedure relies on having a close enough starting point for the parameters. In this case, the updated values are deemed reasonable and are carried over to the PSO routines.

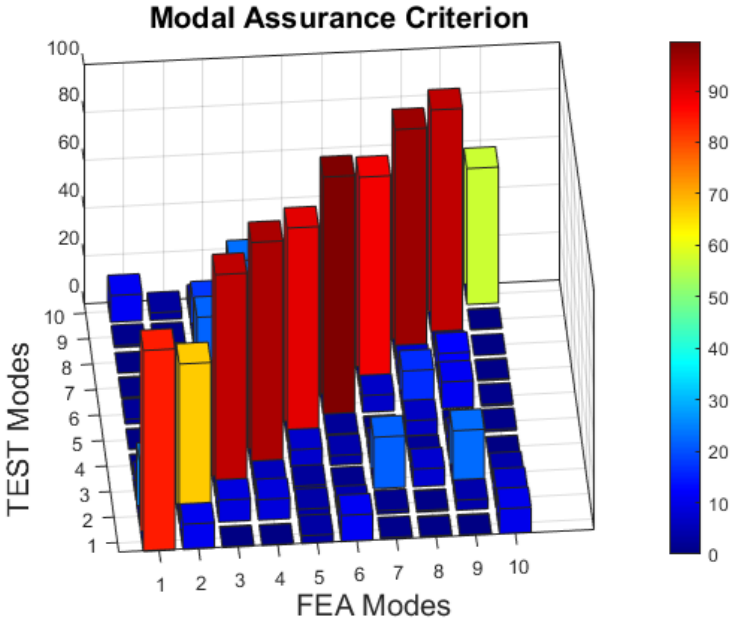

Figure 7.16: Non-optimised updated model MAC matrix

7.3.3 Optimised Component

With the updated model available, a PSO routine is set out to improve on the non-optimised test vehicle of the previous section. The first step is to parameterise the edge as the search domain, and associate normal directions at each section. Secondly, a new FRF raster has to be tailored for this mesh. This set of 16 FRF extraction points is presented in Figure 7.17 and for each location, direct FRFs are evaluated in all 3 spatial directions.

The PSO is scripted to run with 4 tabs of 15mm width and 12mm length and with no edge restrictions. The swarm is set at 25 particles and 50 generations, however depending on the behaviour of the convergence curves, this can be extended if required.

The convergence curve for this simulation is shown in Figure 7.18 and displays an interesting behaviour, given that the final optimal value was reached in relatively late, at generation 31. Nevertheless, 20 generations later no further improvements are determined by the program and the optimal layout is established.

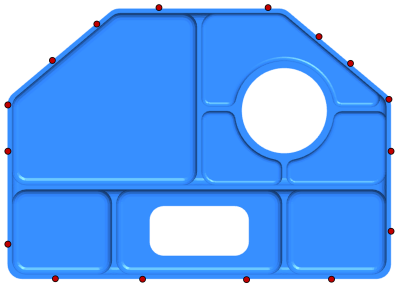

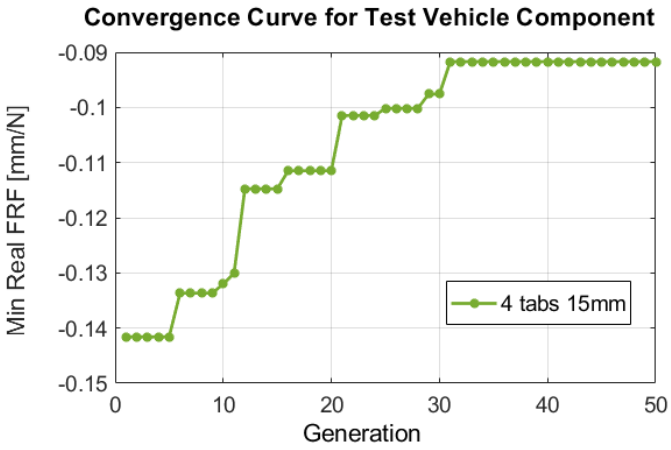

Figure 7.17: Tab FRF raster Figure 7.18: Tab optimisation convergence curve

The physical layout of this optimised solution is presented in Figure 7.19 and displays two of the tabs in the bottom long edge, whilst the other two are centrally placed on the top diagonals.

As a comparison between models, if evaluated under the same fitness function as the PSO, the non-optimised layout would export a fitness function of -0.277 [mm/N], which is a worse result than the best randomised initial seed in generation 1. This

value also showcases that the optimisation improved the fitness function between the non-optimised layout by around 65%, to -0.0917 [mm/N].

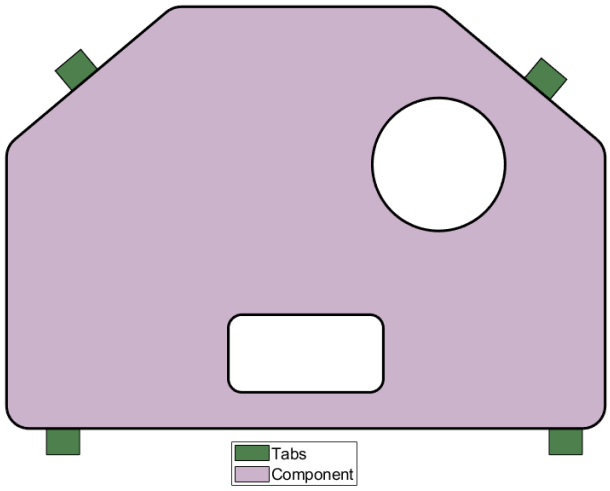

Figure 7.19: Optimal layout

The resulting layout from the PSO routine is machined following stages 1 and 2, but varying the tab positions in stage 3. The machined component is presented in Figure 7.20.

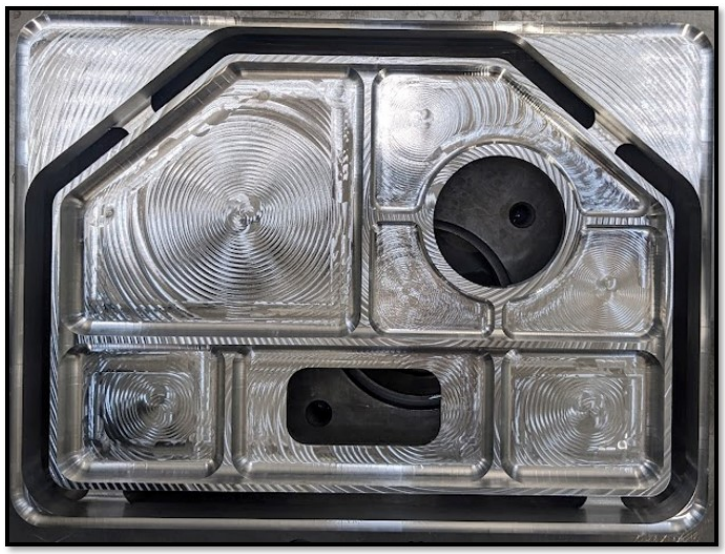

Figure 7.20: Optimised machined component

This component is tap tested to evaluate the robustness and reliability of the updating

parameters calculated previously and whether or not they transfer correctly onto other layouts. Evaluating the EMA data gathered in Table 7.5, the frequency estimation averages a 3.3% absolute difference to the experimental data which is expectedly higher than the updated model. Mode shape estimation is also reasonably accurate with a 79.8% average for the paired modes. As in the previous experimental instance, mode 2 is a source of higher discrepancy, as is mode 7. Despite presenting an increase in estimation difference, the FEA model is deemed suitable.

Mode	FEA [Hz]	EMA [Hz]	Δ (%)	MAC (%)
1	100.3	98.0	2.3	86.3
2	144.1	135.5	6.3	71.1
3	149.2	145.7	2.4	89.7
4	492.0	495.0	-0.6	94.2
5	700.2	707.6	-1.0	83.3
6	958.3	949.4	0.9	80.3
7	934.6	1001.8	-6.7	68.3
8	1341.7	1311.0	2.3	95
9	1397.8	1420.0	-1.6	91.5
10	1510.7	1602.5	-5.7	68.3

Table 7.5: Frequency estimation comparison for optimal layout

7.3.4 Additional Optimisation Runs

Building on top of the test vehicle models, the PSO program is tested using different user defined variables governing the simulations. To have a partially comparative test, the total width of tab interface is maintained for different number of tabs. In this way, three tabs of 20mm, and five tabs of 12mm, are submitted for evaluation, which maintain the original total tab width of 60mm. To adjust the updated stiffness to tabs of different size, the values were normalised to tab width and proportionally scaled. This point represents a debatable extrapolation of the updating result and is presented as a future research avenue to explore.

From Figure 7.21 some of interesting observations can be derived. Firstly, both sets of convergence curves appear to converge sooner than the four tab simulation. This can be due to the randomised initialisation feature of the PSO and potential good initial estimates. However, looking at the five tabs simulation, the optimal result is reached in generation 9, which can be explained by a higher relative density of tabs within the search space. Looking at the layout dispositions, the three tabs simulation presents an asymmetric solution, which would be hard to derive without the program. The

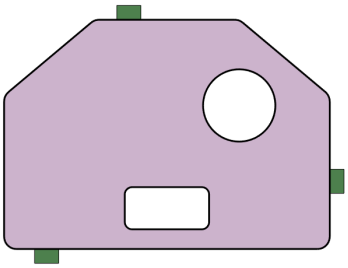

(a) Three tabs optimal layout

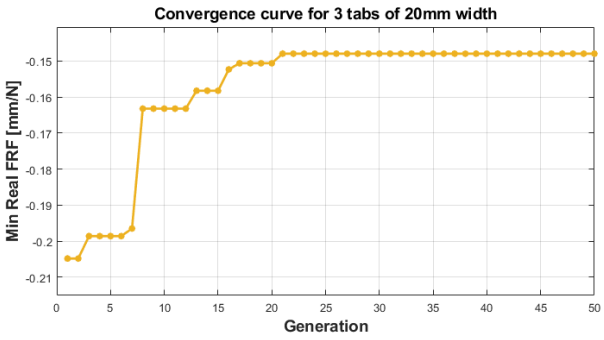

(b) Three tabs convergence curve

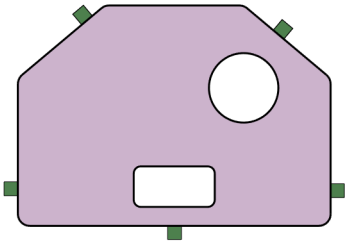

(c) Five tabs optimal layout

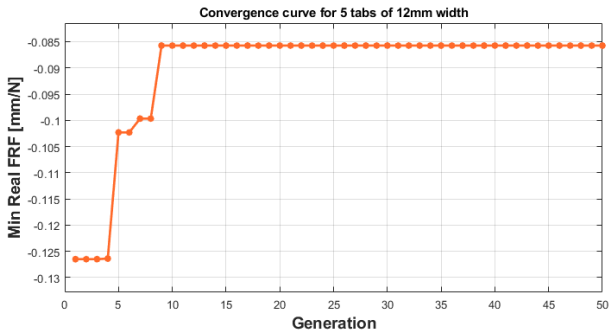

(d) Five tabs convergence curve

Figure 7.21: Additional optimisation results

five tabs model, in contrast, is fairly symmetrical, with the exception of the topmost tabs at different positions within the diagonal edge.

One final observation drawn from these simulations has to do with the fitness function value reached by the optimal layouts. Each tab added to the component improves the fitness function. The results obtained were $-0.0857, -0.0917$ and -0.1479 [mm/N] for the 5, 4 and 3 tab models respectively.

7.4 Discussion

Throughout the development and expansion of the optimisation program onto a parting-off tab layout problem, the main objective was centred around improving the understanding of workpiece based dynamic behaviour and how these optimisation methods can improve machining operations of flexible and minimally held workpieces. In this case, the component studied encompassed that description; a large unsupported thin floor and thin walled part, with double sided machining operations. The development of this required detailed evaluation of modelling techniques to find

the most suitable candidate, improvements to the software integration and numerical evaluation of dynamic behaviour, and finally an implementation of the PSO program.

These developments are complemented by experimental data obtained from machining a set of physical components and subsequent modal analysis tests. The purpose of these tests was to initially provide an updating reference for the FEA model, but also to compare the robustness of this process when extrapolating its results onto different layouts.

One of the main objectives of this section was to expand and add versatility to the PSO program developed. Broadening the application of the optimisation routine onto internal features of a billet is a substantial benefit to the workpiece modelling capabilities of GKN. The procedure followed to attain this objective is rigorous and different methods are quantitatively evaluated for its implementation. This activity by itself presents a useful understanding for future applications of each method.

Another relevant point of discussion is the contrast of geometrical and dynamic behaviour presented between nominal and physical tabs. More precise analytical modelling of the tabs can be performed to derive estimates with better accuracy. Nevertheless, one of the strong arguments in favour of model updating approaches is to provide the initial model with a set of values and allow the numerical methods to converge to the most accurate results. Discussion can then be centred on how much detail can go into analytical definitions of stiffness parameters for these tabs and its extended benefit on the modelling and updating results. An argument for higher detail can be based on the extrapolation of stiffness onto tabs of different width in Section 7.3.4. In this case the updated stiffness values are spatially normalised and scaled to the new width value, however the validity of this extrapolation can be debated. Further machined test vehicles with different tab designs can aid the characterisation of parting off tabs, however this is beyond the objectives of this section and can be considered follow up stages to this chapter.

This previous aspect is also related to the fact that the non-optimised model, where the update is originally created, presents significantly lower levels of error than the optimal model. This is an expected and understandable result which is also related to the extrapolation of updated parameters from one model to another. In this case, errors are low and well within adequate EMA standards for model validation, however understanding the limits and defining strict criteria for the extrapolation of these results is critical for further applications of this program onto production parts.

Another objective of this section is met by comparing the benefits in PSO results of the 4 tab model between non-optimised and optimised versions. Compared under the same FEA based metric, a 65% increase in fitness function is obtained between them and presents a considerable benefit. Comparing experimental FRFs obtained from both EMA tests, the benefit is of 45%, which is of similar magnitude than the FEA estimate, and variations are due to the higher level of error observed in the optimal layout between its FEA estimation and the EMA data.

One final point of discussion revolves around the applicability of this program to other types of setup. In this case a rib type component is studied, nevertheless parting off tabs are found in other families of prismatic and monolithic parts. A main avenue to implement this optimisation approach is in parts where tabs fall within a broader 3D surface, rather than a 2D part edge. This would require the PSO to be expanded onto 3D search spaces rather than a 2D edge parameterisation, as has been the previous cases. Despite the fact that, using spatial resolution values, any surface can parameterised into a single dimension domain, a far more interesting approach would be to define the PSO seeds as multidimensional vectors. Some careful definition of progression must be introduced, but the idea is applicable into the existing framework. Using orthogonal vectors for each dimension of a seed, the PSO parameters can also be equipped with a multidimensional definition and run under the same architecture. Alongside this, the PSO fitness functions can also be targeted onto different objectives. In the case where a particular tooling and cutting process is determined as a requirement (due to certifications for example), the fitness functions can target layouts that provide natural frequencies in a particular band. This is an example of ways to tailor the establish the PSO system to carry out optimisation tasks that can further benefit the production process at GKN.

Chapter 8

Conclusions

The conclusions Chapter presents a brief summary of this Thesis, its key findings and contributions to knowledge, as well as a future work and proposed avenues of research section.

8.1 Key findings and contributions to knowledge

The first contribution stemming from this work is the development of a computational program capable of autonomously evaluating and optimising workpiece dynamic modelling for machining workholding applications. This is supported by the characterisation of various FEA modelling techniques, the evaluation of their strengths and weaknesses, and the specific suitability each one of them can offer for a particular application. This study complements the existing literature in the fields of structural dynamics and machining stability, due to the unique implementation of receptance and critical depth of cut metrics to define the optimisation objective functions. Objective 1 of Section 1.2 is successfully achieved and the software developed is used on a set of different applications.

Secondly this thesis is one of the few available research projects that targets workholding for machining stability in double sided access environments. This ambitious machining strategy incurs in an intrinsic reduction in workpiece stiffness and any development to increase cutting stability is a valuable step forward in enabling this type of technology. This presents a novel contribution to the field and complements existing methods for stable machining in DSA approaches.

This research also presents a novel application of the particle swarm heuristic, by

means of using dynamic response variables in the fitness function definition. In this regard, it is also a unique contribution to the field of machining layout optimisation, as few projects are centred on machining stability, and this is the first to use FRF based results and SLD estimations for iterative adaptation of the component's workholding definition. This meets the third objective set out in Chapter 1 by linking chatter analysis with computer-aided fixture design methodologies.

Parting off tabs is a rare topic in the machining literature, let alone the topological optimisation of these features for milling operations. Given that this type of feature are more of an practical hurdle than a engineering requirement, machinists usually use common guideline approaches based on trial and error experience for their definition. In this project, a robust mechanistic approach is used to understand the dynamic response of the workpiece and define from there the optimal locations these features must take to ensure the required stability parameters. It can be concluded from this work that this industrial design aspect can benefit from the integrated FEA development of this project. The novelty of this study is found in the characterisation of breakaway tabs, the evaluation on their influence on workpiece dynamics, and the optimisation of layout positions to maximise cutting stability.

One of the main objectives of this work was to provide a capable and versatile optimisation package. For this reason, the programs have been scripted to allow wide variability both in user defined parameters as well as machining applications. This is conveyed in the range of applications covered in this Thesis, including unmachined, semi-roughed and finished components. Different fitness functions were also trialled, as well as diverse modelling techniques. This does not mean that the Thesis limits the application scope, on the contrary, the developed system is open for further expansions and allows the user to tailor the program to their particular requirements. This concludes in a successful completion of the main objectives set out for this Thesis.

The boundary condition modelling techniques used in this work, have been identified to work best to model different aspects of workholding modelling and optimisation. In this regard, this Thesis mainly employed interface layer techniques to update models with contact surfaces of external workholding elements, such as a bolted joint or vice clamp. Conversely, the parting off tab work preferred a spring boundary condition formulation for modelling the component. An important learning point that derives from this work is the ability to recognise and discern where each approach can provide better results for workpiece modelling, updating and optimisation. This aligns to Objective 2 of Section 1.2, where multi-body assemblies, joint characterisation

and model updating proved to be beneficial and necessary steps for the optimisation protocols of assembled workholding fixtures.

This work is presented as a complementary approach to existing chatter avoidance techniques and does not necessarily impede the implementation of other existing strategies. Given the industrial environment of this work, a rapid deployment technique was one of the industrial motivation factors that guided the development of the modelling and optimisation process. Implementation of external dampers and robotic assisted strategies to improve cutting stability can further enhance the work presented and complement the efforts to enable double sided access approaches.

The direct dependence of machining stability to dynamic response of the workpiece requires any FEA approximation to be as accurate as possible. In this regard, it is concluded that EMA and model updating activities are considered essential stages in the implementation of these evaluation and optimisation routines. As the accuracy of the optimisation is set by the accuracy of the FEA solution, validated and updated models are necessarily going to improve the optimisation. Therefore, the reliability and trustworthiness of the optimisation results depends considerably on the estimation natural frequencies and receptance behaviour of the workpiece, which are reportedly improved by EMA and model updating procedures.

It can then be concluded that the work covered in this Thesis improves the definition of machining workholding layouts. All objectives set out in Chapter 1 are successfully met. The developments presented can be used to evaluate and measure assembled fixturing alternatives with a focus on machining dynamic stability. Furthermore, this Thesis has successfully implemented an optimisation program that yields the most stable layout for a particular set of user-defined and application specific constraints. Applicable to different stages within a machining operation, the program can be used in a variety of applications, and serves as a contribution to the fields of chatter avoidance and machining fixture layout optimisation.

8.2 Limitations and recommendations for future work

If GKN Aerospace wish to expand on this project, an initial recommendation would be to derive a standalone executable of the optimisation architecture. This is based on the fact that as it stands, deep understanding of the existing codes, functions and subroutines developed are required to run the program. An executable could ease

the implementation onto production parts and can take a step by step approach to ensure all the program required variables are well defined.

Associated to the previous point, it is relevant to consider that larger and more complex simulations can considerably benefit of a higher capacity computing systems. In this thesis, all simulations were carried out on a computer with 4-core 16GB RAM memory and 2.8GHz CPU. Despite being quite powerful for most engineering applications, it is common to encounter modelling machines with more than twice the RAM power or even linked to HPC units. Significant improvement to computational times can be done cheaply and straightforwardly by implementation onto more capable computers.

The previous aspect highlights one of the main limitations explored in this thesis, which relates to the fact that the PSO program was not trialled into exploring values inside the lobes of a SLD plot. One of the main reasons for this decision is that a SLD is specific to a particular tool and radial engagement configuration. Given that prismatic machining is known to involve several cutter geometries and operations, optimisation for a single tool might not transfer adequately to others. For the current setup, it is recommended to define the optimal layout and then perform tool based modal analysis and derive stage specific SLD plots to determine the most productive cutting conditions.

The applications showcased in this thesis are by no means a hard limit con the capabilities of the system. Despite only evaluating two different fitness function definitions, the program is set up in such a way that other responses can be targeted. For example, if a machining and tooling characteristics of an operation are fixed due to microstructural requirements of machined surfaces (common in Ti and Ni machining), then the system can target mode frequencies to enhance those specific cutting requirements. Alternatively, the focus can also be set onto particular frequency bands, where the periodical tool excitation might be situated.

8.3 Publications

A conference paper was presented at Eurodyn-2023. It described the software integration solution for the optimisation programming of Chapter 4. The title is *"Unsupported machining fixture layout optimisation"*

References

[1] R. Fu, P. Curley, C. Higgins, Z. M. Kilic, D. Sun, A. Murphy, and Y. Jin, "Double-sided milling of thin-walled parts by dual collaborative parallel kinematic machines," Journal of Materials Processing Technology, vol. 299, p. 117395, 2022.

[2] I. Boyle, Y. Rong, and D. C. Brown, "A review and analysis of current computer-aided fixture design approaches," Robotics and Computer-Integrated Manufacturing, vol. 27, no. 1, pp. 1–12, 2011.

[3] K. Cheng, Machining Dynamics:Fundamentals, Applications and Practices. Springer, 2009.

[4] S. S. Rao, Mechanical Vibrations. Prentice Hall, 2011.

[5] G. Quintana and J. Ciurana, "Chatter in machining processes: A review," International Journal of Machine Tools and Manufacture, vol. 51, no. 5, pp. 363–376, 2011.

[6] S. Tobias, "Machine tool vibrations," Blackie and Son, London, 1965.

[7] R. Faassen, Chatter Prediction and Control for High-Speed Milling: Modelling and Experim PhD thesis, Technische Universiteit Eindhoven, 2007.

[8] M. Wiercigroch and A. Krivtsov, "Frictional chatter in orthogonal metal cutting," Philosophical Transactions of The Royal Society A: Mathematical, Physical and Engineering Sciences, vol. 359, pp. 713–738, 04 2001.

[9] M. Wiercigroch and E. Budak, "Sources of nonlinearities, chatter generation and suppression in metal cutting," Philosophical Transactions of The Royal Society A: Mathematical, Physical and Engineering Sciences, vol. 359, pp. 663–693, 04 2001.

[10] Y. Altintas, Manufacturing Automation. Cambridge University Press, 2012.

[11] A. Gasparetto, "Eigenvalue analysis of mode-coupling chatter for machine-tool stabilization," Journal of Vibration and Control, vol. 7, no. 2, pp. 181–197, 2001.

[12] Z. Pan, H. Zhang, Z. Zhu, and J. Wang, "Chatter analysis of robotic machining process," Journal of Materials Processing Technology, vol. 173, no. 3, pp. 301 – 309, 2006.

[13] L. Yuan, Z. Pan, D. Ding, S. Sun, and W. MCPS Li, "A review on chatter in robotic machining process regarding both regenerative and mode coupling mechanism," IEEE/ASME Transactions on Mechatronics, vol. PP, pp. 1–1, 08 2018.

[14] L. Yuan, S. Sun, Z. Pan, D. Ding, O. Gienke, and W. Li, "Mode coupling chatter suppression for robotic machining using semi-active magnetorheological elastomers absorber," Mechanical Systems and Signal Processing, vol. 117, pp. 221 – 237, 2019.

[15] X. J. Zhang, C. H. Xiong, Y. Ding, M. J. Feng, and Y. L. Xiong, "Milling stability analysis with simultaneously considering the structural mode coupling effect and regenerative effect," International Journal of Machine Tools and Manufacture, vol. 53, no. 1, pp. 127 – 140, 2012.

[16] H. Celikag, E. Ozturk, and N. D. Sims, "Can mode coupling chatter happen in milling?," International Journal of Machine Tools and Manufacture, vol. 165, p. 103738, 2021.

[17] Y. Altintas and E. Budak, "Analytical Prediction of Stability Lobes in Milling," Annals of the CIRP, vol. 44, no. 2, pp. 357–362, 1995.

[18] J. Tlusy and M. Polacek, "The stability of machine tools against self-excited vibration in machining," International research in production engineering, ASME, pp. 465–474, 1963.

[19] H. E. Merrit, "Theory of Self-Excited Machine-Tool Clatter," Journal of Engineering for Industry, 1965.

[20] R. Sridhar, R. Hohn, and G. Long, "A general formulation of the milling process equation: Contribution to machine tool chatter research—5," Journal of Engineering for Industry, vol. 90, no. 2, pp. 317–324, 1968.

[21] I. Minis and R. Yanushevsky, "A new theoretical approach for the prediction of machine tool chatter in milling," Journal of Engineering for Industry, vol. 115, no. 1, pp. 1–8, 1993.

[22] T. Insperger and G. Stepan, "Semi-discretization method for delayed systems," International Journal for Numerical Methods in Engineering, vol. 518, no. December 2001, pp. 503–518, 2002.

[23] J. Gradišek, E. Govekar, I. Grabec, M. Kalveram, K. Weinert, T. Insperger, and G. Stépán, "On Stability Prediction For Low Radial Immersion Milling," Machine Science and Technology, vol. 9, pp. 117–130, 2007.

[24] E. Budak and Y. Altintas, "Analytical Prediction of Chatter Stability in Milling — Part II : Application of the General Formulation to Common Milling Systems," Journal of Dynamic Systems, Measurement and Control, vol. 120, no. March 1998, pp. 31–36, 1998.

[25] J. Munoa, Z. Dombovari, I. Mancisidor, Y. Yang, and M. Zatarain, "Interaction between multiple modes in milling processes," Machining Science and Technology, vol. 17, no. 2, pp. 165–180, 2013.

[26] S. D. Merdol and Y. Altintas, "Multi Frequency Solution of Chatter Stability for Low Immersion Milling," Journal of Manufacturing Science and Engineering, vol. 126, no. August 2004, pp. 459–466, 2019.

[27] N. Sims, B. Mann, and S. Huyanan, "Analytical prediction of chatter stability for variable pitch and variable helix milling tools," Journal of Sound and Vibration, vol. 317, no. 3-5, pp. 664–686, 2008.

[28] D. Bachrathy and G. Stepan, "Improved prediction of stability lobes with extended multi frequency solution," CIRP Annals - Manufacturing Technology, vol. 62, no. 1, pp. 411–414, 2013.

[29] M. Wang, L. Gao, and Y. Zheng, "Prediction of regenerative chatter in the high-speed vertical milling of thin-walled workpiece made of titanium alloy," Int. J Adv Manuf Technol, vol. 120, pp. 707–716, 2014.

[30] T. Insperger and G. Stepan, "Semi-discretization method for delayed systems," International Journal for Numerical Methods in Engineering, vol. 518, no. December 2001, pp. 503–518, 2002.

[31] T. Insperger and G. Stépán, "Updated semi-discretization method for periodic delay-differential equations with discrete delay," International Journal for Numerical Methods in Engineering, vol. 141, no. January, pp. 117–141, 2004.

[32] T. Insperger, J. Munoa, M. a. Zatarain, and G. Peigné, "Unstable islands in the stability chart of milling processes due to the helix angle," in CIRP 2nd international conference on high performance cutting, Vancouver, Canada, pp. 12–13, 2006.

[33] T. Kalmár-Nagy, G. Stépán, and F. C. Moon, "Subcritical hopf bifurcation in the delay equation model for machine tool vibrations," Nonlinear Dynamics, vol. 26, no. 2, pp. 121–142, 2001.

[34] G. Stepan, R. Szalai, B. P. Mann, P. V. Bayly, T. Insperger, J. Gradisek, and E. Govekar, "Nonlinear dynamics of high-speed milling—analyses, numerics, and experiments," Journal of Vibration and Acoustics, vol. 127, no. 2, pp. 197–203, 2005.

[35] M. Fofana, "Sufficient conditions for the stability of single and multiple regenerative chatter," Chaos, Solitons & Fractals, vol. 14, no. 2, pp. 335–347, 2002.

[36] M. Fofana, "Delay dynamical systems and applications to nonlinear machine-tool chatter," Chaos, Solitons & Fractals, vol. 17, no. 4, pp. 731–747, 2003.

[37] Y. Ding, L. Zhu, X. Zhang, and H. Ding, "A full-discretization method for prediction of milling stability," International Journal of Machine Tools and Manufacture, vol. 50, no. 5, pp. 502–509, 2010.

[38] T. Insperger, "Full-discretization and semi-discretization for milling stability prediction: some comments," International Journal of Machine Tools and Manufacture, vol. 50, no. 7, pp. 658–662, 2010.

[39] C. Yue, X. Liu, and S. Y. Liang, "A model for predicting chatter stability considering contact characteristic between milling cutter and workpiece," The International Journal of Advanced Manufacturing Technology, vol. 88, no. 5-8, pp. 2345–2354, 2017.

[40] Y. Ding, L. Zhu, X. Zhang, and H. Ding, "Second-order full-discretization method for milling stability prediction," International Journal of Machine Tools and Manufacture, vol. 50, no. 10, pp. 926–932, 2010.

[41] Q. Quo, Y. Sun, and Y. Jiang, "On the accurate calculation of milling stability limits using third-order full-discretization method," International Journal of Machine Tools and Manufacture, vol. 62, pp. 61–66, 2012.

[42] C. Ozoegwu, S. Omenyi, and S. Ofochebe, "Hyper-third order full-discretization methods in milling stability prediction," International Journal of Machine Tools and Manufacture, vol. 92, pp. 1–9, 2015.

[43] P. Bayly, J. Halley, B. P. Mann, and M. Davies, "Stability of interrupted cutting by temporal finite element analysis," Journal of Manufacturing Science and Engineering, vol. 125, no. 2, pp. 220–225, 2003.

[44] B. P. Mann, K. A. Young, T. L. Schmitz, and D. N. Dilley, "Simultaneous stability and surface location error predictions in milling," Journal of Manufacturing Science and Engineering, vol. 127, no. 3, pp. 446–453, 2005.

[45] T. Insperger, B. P. Mann, G. Stépán, and P. V. Bayly, "Stability of up-milling and down-milling, part 1: alternative analytical methods," International journal of Machine tools and manufacture, vol. 43, no. 1, pp. 25–34, 2003.

[46] B. Patel, B. Mann, and K. Young, "Uncharted islands of chatter instability in milling," International Journal of Machine Tools and Manufacture, vol. 48, no. 1, pp. 124–134, 2008.

[47] M. Zatarain, J. Munoa, G. Peigné, and T. Insperger, "Analysis of the influence of mill helix angle on chatter stability," CIRP annals, vol. 55, no. 1, pp. 365–368, 2006.

[48] Y. Altintas and M. Campoanes, "An improved time domain simulation for dynamic milling at small radial immersions," Journal of Manufacturing Science and Engineering, vol. 125, pp. 416–422, 2003.

[49] M. Zatarain, J. Alvarez, I. Bediaga, J. Munoa, and Z. Dombovari, "Implicit subspace iteration as an efficient method to compute milling stability lobe diagrams," The International Journal of Advanced Manufacturing Technology, vol. 77, no. 1-4, pp. 597–607, 2015.

[50] Z. Li, Z. Yang, Y. Peng, F. Zhu, and X. Ming, "Prediction of chatter stability for milling process using runge-kutta-based complete discretization method," The International Journal of Advanced Manufacturing Technology, vol. 86, no. 1-4, pp. 943–952, 2016.

[51] J. Niu, Y. Ding, L. Zhu, and H. Ding, "Runge-kutta methods for a semi-analytical prediction of milling stability," Nonlinear Dynamics, vol. 76, no. 1, pp. 289–304, 2014.

[52] D. Lehotzky, T. Insperger, F. Khasawneh, and G. Stepan, "Spectral element method for stability analysis of milling processes with discontinuous time-periodicity," The International Journal of Advanced Manufacturing Technology, vol. 89, no. 9-12, pp. 2503–2514, 2017.

[53] J. Munoa, X. Beudaert, Z. Dombovari, Y. Altintas, E. Budak, C. Brecher, and G. Stepan, "Chatter suppression techniques in metal cutting," CIRP Annals - Manufacturing Technology, vol. 65, no. 2, pp. 785–808, 2016.

[54] S. Atlar, E. Budak, and H. Özgüven, "Modeling part dynamics and chatter stability in machining considering material removal," in 1st Int. Conf. on Process Machine Interactions, Hannover, pp. 61–72, 2008.

[55] E. Budak, L. T. Tunç, S. Alan, and H. N. Özgüven, "Prediction of workpiece dynamics and its effects on chatter stability in milling," CIRP annals, vol. 61, no. 1, pp. 339–342, 2012.

[56] S. Herranz, F. J. Campa, L. N. De Lacalle, A. Rivero, A. Lamikiz, E. Ukar, J. A. Sánchez, and U. Bravo, "The milling of airframe components with low rigidity: A general approach to avoid static and dynamic problems," Proceedings of the Institution of Mechanical Engineers, Part B: Journal of Engineering Manufacture, vol. 219, no. 11, pp. 789–801, 2005.

[57] J. Wang, S. Ibaraki, and A. Matsubara, "A cutting sequence optimization algorithm to reduce the workpiece deformation in thin-wall machining," Precision Engineering, vol. 50, pp. 506–514, 2017.

[58] J. Munoa, M. Sanz-Calle, Z. Dombovari, A. Iglesias, J. Pena-Barrio, and G. Stepan, "Tuneable clamping table for chatter avoidance in thin-walled part milling," CIRP Annals, vol. 00, pp. 14–17, 2020.

[59] G. Campatelli, L. Sallese, and A. Scippa, "Design of an active workpiece holder," Procedia CIRP, vol. 34, pp. 217–222, 2015.

[60] E. Abele, H. Hanselka, F. Haase, D. Schlote, and A. Schiffler, "Development and design of an active work piece holder driven by piezo actuators," Production Engineering, vol. 2, no. 4, pp. 437–442, 2008.

[61] X. Beudaert, K. Erkorkmaz, and J. Munoa, "Portable damping system for chatter suppression on flexible workpieces," CIRP Annals, vol. 68, no. 1, pp. 423–426, 2019.

[62] G. Gubanov, "Broadband pneumatic mass damper for the elimination of workpiece vibrations," CIRP Journal of Manufacturing Science and Technology, vol. 30, pp. 184–194, 2020.

[63] Y. Yang, R. Xie, and Q. Liu, "Design of a passive damper with tunable stiffness and its application in thin-walled part milling," The International Journal of Advanced Manufacturing Technology, vol. 89, pp. 2713–2720, 2017.

[64] T. N. Papastathis, S. M. Ratchev, and A. A. Popov, "Dynamics model of active fixturing systems for thin-walled parts under moving loads," The International Journal of Advanced Manufacturing Technology, vol. 62, pp. 1233–1247, 2012.

[65] O. J. Bakker, T. Papastathis, A. A. Popov, and S. Ratchev, "Active fixturing: literature review and future research directions," International Journal of Production Research, vol. 51, no. 11, pp. 3171–3190, 2013.

[66] A. Rashid and C. M. Nicolescu, "Active vibration control in palletised workholding system for milling," International Journal of Machine Tools and Manufacture, vol. 46, no. 12-13, pp. 1626–1636, 2006.

[67] J. Munoa, A. Iglesias, A. Olarra, Z. Dombovari, M. Zatarain, and G. Stepan, "Design of self-tuneable mass damper for modular fixturing systems," CIRP Annals, vol. 65, no. 1, pp. 389–392, 2016.

[68] H. C. Moehring, P. Wiederkehr, O. Gonzalo, and P. Kolar, Intelligent fixtures for the manufacturing of low rigidity components. Springer, 2018.

[69] K. Krishnakumar and S. N. Melkote, "Machining fixture layout optimization using the genetic algorithm," International Journal of Machine Tools and Manufacture, vol. 40, no. 4, pp. 579–598, 2000.

[70] N. Kaya, "Machining fixture locating and clamping position optimization using genetic algorithms," Computers in Industry, vol. 57, no. 2, pp. 112–120, 2006.

[71] K. Padmanaban, K. Arulshri, and G. Prabhakaran, "Machining fixture layout design using ant colony algorithm based continuous optimization method," The International Journal of Advanced Manufacturing Technology, vol. 45, no. 9-10, pp. 922–934, 2009.

[72] M. Vasundara and K. Padmanaban, "Recent developments on machining fixture layout design, analysis, and optimization using finite element method and evolutionary techniques," The International Journal of Advanced Manufacturing Technology, vol. 70, no. 1-4, pp. 79–96, 2014.

[73] G. Li, S. Du, D. Huang, C. Zhao, and Y. Deng, "Elastic mechanics-based fixturing scheme optimization of variable stiffness structure workpieces for surface quality improvement," Precision Engineering, vol. 56, pp. 343–363, 2019.

[74] H. Deng and S. N. Melkote, "Determination of minimum clamping forces for dynamically stable fixturing," International Journal of Machine Tools and Manufacture, vol. 46, no. 7-8, pp. 847–857, 2006.

[75] B. Li and S. N. Melkote, "Improved workpiece location accuracy through fixture layout optimization," International Journal of Machine Tools and Manufacture, vol. 39, no. 6, pp. 871–883, 1999.

[76] M. Calabrese, T. Primo, and A. Del Prete, "Optimization of machining fixture for aeronautical thin-walled components," Procedia CIRP, vol. 60, pp. 32–37, 2017.

[77] Y. Zhou, Y. Li, and W. Wang, "A feature-based fixture design methodology for the manufacturing of aircraft structural parts," Robotics and Computer-Integrated Manufacturing, vol. 27, no. 6, pp. 986–993, 2011.

[78] M. Sabareeswaran, K. P. Padmanaban, and K. A. Sundararaman, "Comparison of evolutionary techniques for the optimization of machining fixture layout under dynamic conditions," Proceedings of the Institution of Mechanical Engineers, Part C: Journal of Mechanical Engineering Science, vol. 232, no. 12, pp. 2145–2158, 2018.

[79] F. Michael Thomas Rex, P. Hariharasakthisudhan, A. Andrews, and B. Prince Abraham, "Optimization of flexible fixture layout to improve form quality using parametric finite element model and mixed discrete-integer genetic algorithm," Proceedings of the Institution of Mechanical Engineers, Part C: Journal of Mechanical Engineering Science, vol. 236, no. 1, pp. 16–29, 2022.

[80] S. Satyanarayana and S. Melkote, "Finite element modeling of fixture–workpiece contacts: single contact modeling and experimental verification," International journal of machine tools and manufacture, vol. 44, no. 9, pp. 903–913, 2004.

[81] N. Olgac and R. Sipahi, "A unique methodology for chatter stability mapping in simultaneous machining," 2005.

[82] C. Brecher, Y. Trofimov, and S. Bäumler, "Holistic modelling of process machine interactions in parallel milling," CIRP annals, vol. 60, no. 1, pp. 387–390, 2011.

[83] E. Budak, A. Comak, and E. Ozturk, "Stability and high performance machining conditions in simultaneous milling," CIRP Annals, vol. 62, no. 1, pp. 403–406, 2013.

[84] E. Shamoto, T. Mori, B. Sencer, N. Suzuki, and R. Hino, "Suppression of regenerative chatter vibration in multiple milling utilizing speed difference method–analysis of double-sided milling and its generalization to multiple milling operations," Precision Engineering, vol. 37, no. 3, pp. 580–589, 2013.

[85] S. Ma, J. Xiao, H. Liu, S. Liu, and Y. Tian, "Modeling and analysis for time-varying dynamics of thin-walled workpieces in mirror milling considering material removal," Science China Technological Sciences, pp. 1–16, 2023.

[86] E. Ozturk, A. Barrios, C. Sun, S. Rajabi, and J. Munoa, "Robotic assisted milling for increased productivity," CIRP Annals, vol. 67, no. 1, pp. 427–430, 2018.

[87] A. Barrios, S. Mata, A. Fernandez, J. Munoa, C. Sun, and E. Ozturk, "Frequency response prediction for robot assisted machining," MM Science Journal, vol. 2019, no. 04, pp. 3099–3106, 2019.

[88] M. Sadd, Elasticity. Elsevier Butterworth-Heinemann, 2005.

[89] D. J. Ewins, Modal Testing: Theory, Practice and Application. Engineering dynamics series], Wiley, 2000.

[90] S. Adhikari and J. Woodhouse, "Identification of damping: part 1, viscous damping," Journal of Sound and vibration, vol. 243, no. 1, pp. 43–61, 2001.

[91] S. Adhikari, "Damping characterization in dynamic problems," 2021.

[92] J. Woodhouse, "Linear damping models for structural vibration," Journal of Sound and Vibration, vol. 215, no. 3, pp. 547–569, 1998.

[93] S. Adhikari and A. S. Phani, "Rayleigh's classical damping revisited," in International Conference on Civil Engineering in the New Millennium: Opportunities and Challenges, 2007.

[94] T. Caughey and M. E. O'Kelly, "Classical normal modes in damped linear dynamic systems," Journal of Applied Mechanics, vol. 32, no. 3, pp. 583–588, 1965.

[95] S. Adhikari, "Structural dynamics with generalized damping models: identification," 2013.

[96] O. C. Zienkiewicz, R. L. R. L. Taylor, and J. Z. Zhu, The finite element method : its basis and fundamentals. Amsterdam ; London: Elsevier Butterworth-Heinemann, 6th ed. ed., 2005.

[97] R. G. Grimes, J. G. Lewis, and H. D. Simon, "A shifted block lanczos algorithm for solving sparse symmetric generalized eigenproblems," SIAM Journal on Matrix Analysis and Applications, vol. 15, no. 1, pp. 228–272, 1994.

[98] T. Ericsson and A. Ruhe, "The spectral transformation lanczos method for the numerical solution of large sparse generalized symmetric eigenvalue problems," Mathematics of Computation, vol. 35, no. 152, pp. 1251–1268, 1980.

[99] R. J. Boulbes, "Troubleshooting finite-element modeling with abaqus," Fransa, vol. 1, p. 439, 2020.

[100] D. Wang and X. Fan, "Nonlinear Dynamic Modeling for Joint Interfaces by Combining Equivalent Linear Mechanics with Multi-objective Optimization," Acta Mechanica Solida Sinica, vol. 33, no. 4, pp. 564–578, 2020.

[101] R. Huňady, P. Lengvarský, P. Pavelka, A. Kaľavský, and J. Mlotek, "Stiffness estimation and equivalence of boundary conditions in fem models," Applied Sciences, vol. 11, p. 1482, Feb 2021.

[102] K. G. Sharma and C. S. Desai, "Analysis and Implementation of Thin-Layer Element for Interfaces and Joints," Journal of Engineering Mechanics, vol. 118, no. 12, pp. 2442–2462, 1992.

[103] C. S. Desai, M. M. Zaman, J. G. Lightner, and H. J. Siriwardane, "Thin-layer element for interfaces and joints," International Journal for Numerical and Analytical Methods in Geomechanics, vol. 8, no. 1, pp. 19–43, 1984.

[104] H. Ahmadian, M. Ebrahimi, J. E. Mottershead, and M. I. Friswell, "Identification of bolted-joint interface models," Proceedings of the 2002 International Conference on Noise and Vibration Engineering, ISMA, no. January 2002, pp. 1741–1747, 2002.

[105] D. J. Ewins, Modal testing: theory, practice and application. John Wiley & Sons, 2009.

[106] A. T. Mathis, N. N. Balaji, R. J. Kuether, A. R. Brink, M. R. Brake, and D. D. Quinn, "A review of damping models for structures with mechanical joints," Applied Mechanics Reviews, vol. 72, no. 4, p. 040802, 2020.

[107] M. Nieto, M. Elsayed, and D. Walch, "Modal participation factors and their potential applications in aerospace: A review," 2018.

[108] M. Papadopoulos and E. Garcia, "Sensor placement methodologies for dynamic testing," AIAA journal, vol. 36, no. 2, pp. 256–263, 1998.

[109] D. Li, H. Li, and C. Fritzen, "The connection between effective independence and modal kinetic energy methods for sensor placement," Journal of sound and vibration, vol. 305, no. 4-5, pp. 945–955, 2007.

[110] D. Li, H. Li, and C. Fritzen, "The connection between effective independence and modal kinetic energy methods for sensor placement," Journal of sound and vibration, vol. 305, no. 4-5, pp. 945–955, 2007.

[111] B. J. Schwarz and M. H. Richardson, "Experimental modal analysis," CSI Reliability week, vol. 35, no. 1, pp. 1–12, 1999.

[112] H. Van Brussel and J. Peters, "Comparative assessment of harmonic, random, swept sine and shock excitation methods for the identification of machine tool structures with rotating spindles," Annals of the CIRP, vol. 24, no. 1, pp. 291–296, 1975.

[113] U. of Cincinnati CEAS, "Complete UFF library." https://www.ceas3.uc.edu/sdrluff/all_files.php.

[114] P. Guillaume, P. Verboven, and S. Vanlanduit, "A poly-reference implementation of the least-squares complex frequency- domain estimator," Proceedings of IMAC, Vol. 21, no. January, 2003.

[115] B. Dobson, "A straight-line technique for extracting modal properties from frequency response data," Mechanical Systems and Signal Processing, vol. 1, no. 1, pp. 29–40, 1987.

[116] R. J. Allemang, "The modal assurance criterion - Twenty years of use and abuse," Sound and Vibration, vol. 37, no. 8, pp. 14–21, 2003.

[117] M. Friswell and J. E. Mottershead, Finite element model updating in structural dynamics, vol. 38. Springer Science & Business Media, 1995.

[118] S. Ereiz, I. Duvnjak, and J. Fernando Jiménez-Alonso, "Review of finite element model updating methods for structural applications," Structures, vol. 41, no. April, pp. 684–723, 2022.

[119] C. Brecher, P. Chavan, M. Fey, and M. Daniels, "A modal parameter approach for receptance coupling of tools," MM Science Journal, vol. 2016, no. OCTOBER, pp. 1032–1034, 2016.

[120] T. L. Schmitz and K. S. Smith, Machining dynamics. Springer, 2014.

[121] A. Rezaee Jordehi and J. Jasni, "Parameter selection in particle swarm optimisation: a survey," Journal of experimental & theoretical artificial intelligence, vol. 25, no. 4, pp. 527–542, 2013.

[122] J. Dou, X. Wang, and L. Wang, "Machining fixture layout optimization using particle swarm optimization algorithm," Fourth International Seminar on Modern Cutting and Measurement Engineering, vol. 7997, no. May 2011, p. 79970S, 2010.

[123] O. Cakar and K. Y. Sanliturk, "Elimination of transducer mass loading effects from frequency response functions," Mechanical Systems and Signal Processing, vol. 19, no. 1, pp. 87–104, 2005.

[124] L. Gaul and J. Lenz, "Nonlinear dynamics of structures assembled by bolted joints," Acta Mechanica, vol. 125, no. 1-4, pp. 169–181, 1997.

[125] L. Gaul and J. Becker, "Damping prediction of structures with bolted joints," Shock and Vibration, vol. 17, no. 4, 5, pp. 359–371, 2010.

[126] D. J. Segalman, D. L. Gregory, M. J. Starr, B. R. Resor, M. D. Jew, J. P. Lauffer, and N. M. Ames, "Handbook on dynamics of jointed structures," Sandia National Laboratories, Albuquerque, 2009.

[127] A. P. Piotrowski, J. J. Napiorkowski, and A. E. Piotrowska, "Population size in particle swarm optimization," Swarm and Evolutionary Computation, vol. 58, p. 100718, 2020.

[128] N. C. Chcc et al., "Finite element modeling of arc welded joints," Jurnal Mekanikal, 2007.

[129] D. Serdjuks, V. Kurtenoks, A. Tatarinovs, K. Buka-Vaivade, V. Lapkovskis, V. Mironovs, A. Podkoritovs, and K. Topcijs, "Non-model vibration analysis method for health monitoring of structural joints," Procedia Structural Integrity, vol. 37, pp. 555–562, 2022.

[130] C. Laruelle, R. Boman, L. Papeleux, and J.-P. Ponthot, "Element activation method and non-conformal dynamic remeshing strategy to model additive manufacturing," in 24th International Conference on Material Forming (ESAFORM 2021), 2021.

[131] M. Chiumenti, E. Neiva, E. Salsi, M. Cervera, S. Badia, J. Moya, Z. Chen, C. Lee, and C. Davies, "Numerical modelling and experimental validation in selective laser melting," Additive Manufacturing, vol. 18, pp. 171–185, 2017.

[132] W. S. Awan and T. Mabrouki, "Numerical and experimental investigations of post-machining distortions in thin machined structures considering material-induced residual stress," Journal of the Brazilian Society of Mechanical Sciences and Engineering, vol. 39, pp. 509–521, 2017.